Establishing an *in vitro* disease model for Fabry Disease using patient specific induced pluripotent stem cell-derived sensory neurons

Etablierung eines *in vitro* Krankheitsmodells für M. Fabry mittels patienteneigener sensibler Neurone, generiert über induzierte pluripotente Stammzellen

Doctoral thesis for a doctoral degree

at the Graduate School of Life Sciences,

Julius-Maximilians-Universität Würzburg,

Section Neuroscience

submitted by

Thomas Klein

from

Bamberg

Würzburg 2019

Submitted on: ……..……..

Office stamp

Members of the *Promotionskomitee*:

Chairperson: Prof. Dr. Manfred Gessler

Primary Supervisor: Prof. Dr. Nurcan Üçeyler

Supervisor (Second): PD Dr. Robert Blum

Supervisor (Third): Prof. Dr. Erhard Wishmeyer

Supervisor (Fourth): Prof. Dr. Claudia Sommer

Date of Public Defence: ……..……

Date of Receipt of Certificates:

……

Affidavit

I hereby confirm that my thesis entitled “**Establishing an *in vitro* disease model for Fabry Disease using patient specific induced pluripotent stem cell-derived sensory neurons**” is the result of my own work. I did not receive any help or support from commercial consultants. All sources and / or materials applied are listed and specified in the thesis.

Furthermore, I confirm that this thesis has not yet been submitted as part of another examination process neither in identical or in similar form.

Place, Date Signature

Eidesstattliche Erklärung

Hiermit erkläre ich an Eides statt, die Dissertation “**Etablierung eines *in vitro* Krankheitsmodells für M. Fabry mittels patienteneigener sensibler Neurone, generiert über induzierte pluripotente Stammzellen** ” eigenständig, d.h. insbesondere selbstständig und ohne Hilfe eines kommerziellen Promotionsberaters angefertigt und keine anderen als die von mir angegebenen Quellen und Hilfsmittel verwendet zu haben.

Ich erkläre außerdem, dass die Dissertation weder in gleicher noch in ähnlicher Form bereits in einem anderen Prüfungsverfahren vorgelegen hat.

Ort, Datum Unterschrift

Parts of the results presented in this thesis have been published:

Klein, T., Günther, K., Kwok, C.K., Edenhofer, F., Üçeyler, N. (2018). Generation of the human induced pluripotent stem cell line (UKWNLi001-A) from skin fibroblasts of a woman with Fabry disease carrying the X-chromosomal heterozygous c.708G>C (W236C) missense mutation in exon 5 of the alpha-galactosidase-A gene. *Stem Cell Res* 31**,** 222-226.

The published manuscript and this thesis contain similar text passages in adapted form in some sections.

The TK1 cell line was generated during the master thesis, and fully characterized during this doctoral thesis:

Klein, T. (2016). Generation of patient-derived peripheral sensory neurons via reprogramming and transdifferentiation of human fibroblasts into iPSCs and iNPCs. Master of Science, University of Würzburg.

The control cell line was fully characterized by Katharina Klug during her master thesis:

Klug, K. (2019). Establishment and characterization of patient-derived sensory neurons in genetic small fiber neuropathies. Master of Science, University of Würzburg.

1 Abstract

Fabry disease (FD) is an X-linked lysosomal storage disorder caused by deficiency of the α-galactosidase A (GLA), leading to intracellular accumulations of globotriaosylceramide (Gb3). Acral burning pain, which can be triggered by heat, fever or physical activity is an early hallmark of FD and greatly reduces patients' quality of life. The pathophysiology of FD pain is unknown and research is hindered by the limited *in vivo* availability of suitable human biomaterial. To overcome this obstacle, we generated induced pluripotent stem cells (iPSC) from one female and two male patients with a differing pain phenotype, and developed a refined differentiation protocol for sensory neurons to increase reliability and survival of these neurons, serving as an *in vitro* disease model. Neurons were characterized for the correct neuronal subtype using immunocytochemistry, gene expression analysis, and for their functionality using electrophysiological measurements.

iPSC and sensory neurons from the male patients showed Gb3 accumulations mimicking the disease phenotype, whereas no Gb3 depositions were detected in sensory neurons derived from the female cell line, likely caused by a skewed X-chromosomal inactivation in favor of healthy GLA. Using super-resolution imaging techniques we showed that Gb3 is localized in neuronal lysosomes of male patients and in a first experiment using *d*STORM microscopy we were able to visualize the neuronal membrane in great detail. To test our disease model, we treated the neurons with enzyme replacement therapy (ERT) and analyzed its effect on the cellular Gb3 load, which was reduced in the male FD-lines, compared to non-treated cells. We also identified time-dependent differences of Gb3 accumulations, of which some seemed to be resistant to ERT. We also used confocal Ca^{2+} imaging to investigate spontaneous neuronal network activity, but analysis of the dataset proofed to be difficult, nonetheless showing a high potential for further investigations. We revealed that neurons from a patient with pain pain are more easily excitable, compared to cells from a patient without pain and a healthy control.

We provide evidence for the potential of patient-specific iPSC to generate a neuronal *in vitro* disease model, showing the typical molecular FD phenotype, responding to treatment, and pointing towards underlying electrophysiological mechanisms causing different pain phenotypes. Our sensory neurons are suitable for state-of-the-art microscopy techniques, opening new possibilities for an in-depth analysis of cellular

changes, caused by pathological Gb3 accumulations. Taken together, our system can easily be used to investigate the effect of the different mutations of *GLA* on a functional and a molecular level in affected neurons.

2 Zusammenfassung

Morbus Fabry (M. Fabry) ist eine X-chromosomal vererbte lysosomale Speichererkrankung, die durch die Defizienz von α-Galaktosidase A (GLA) verursacht wird. Diese führt zu pathologischen Ablagerungen von Globotriaosylceramid (Gb3) in Zellen. Akraler, brennender Schmerz, der durch Hitze, Fieber oder Sport ausgelöst werden kann, ist ein frühes Krankheitsmerkmal und reduziert die Lebensqualität der Patienten deutlich. Die Pathophysiologie von M. Fabry ist unklar und die Forschung ist durch die limitierte Verfügbarkeit von humanem Biomaterial nur eingeschränkt möglich. Um dieses Problem zu bewältigen haben wir induzierte pluripotente Stammzellen (iPSC) von einer weiblichen Patientin und zwei männlichen Patienten mit unterschiedlichen Schmerzphänotypen generiert. Mit diesen Zellen konnten wir ein verbessertes Protokoll zur Herstellung sensibler Neurone etablieren um diese als *in vitro* Krankheitsmodell zu nutzen. Die Neurone wurden mittels Immunozytochemie, Genexpressionsanalyse und elektrophysiologischer Messungen auf die korrekte Zellidentität und deren Funktionalität getestet.

Gb3 Ablagerungen konnten als Krankheitsmerkmal in iPSC und sensiblen Neuronen der männlichen Patienten, nicht aber in Zellen der weiblichen Patientin und der Kontrollperson nachgewiesen werden. Das Fehlen von pathologischen Ablagerungen in Zellen der weiblichen Betroffenen ist vermutlich auf eine verschobene X-Inaktivierung zu Gunsten des gesunden GLA zurückzuführen. Nichtsdestotrotz ist es uns durch die Nutzung hochauflösender Mikroskopietechniken gelungen, bei männlichen Patienten Gb3 in neuronalen Lysosomen nachzuweisen und die Membran in großem Detail abzubilden. Die Behandlung der Neurone mit der Enzymersatztherapie (ERT) als Nachweis für die Funktionalität des Krankheitsmodells führte zu einer Reduktion der Gb3 Ablagerungen bei männlichen Zellen, im Vergleich zu unbehandelten Zellen. Zudem konnten wir unterschiedliche Arten von Gb3 Akkumulationen identifizieren, von denen einige scheinbar behandlungsresistent sind. Erste Versuche mit Ca^{2+} Imaging zeigten spontane, neuronale Netzwerkaktivität, die noch weitergehend analysiert werden müssen. Mittels Patch-Clamp Analysen konnten wir zeigen, dass Neurone des Patienten mit Schmerzen leichter erregbar sind als Zellen des Patienten ohne Schmerzen, was einen Hinweis auf die mögliche Beteiligung gestörter Ionenkanäle gibt.

Wir konnten zeigen, dass patientenspezifische iPSC geeignet sind um ein neuronales *in vitro* Krankheitsmodell zu erstellen. Dieses Modell zeigt den typischen molekularen Phänotypen des M. Fabry, spricht auf ERT an und liefert erste Hinweise auf pathologische elektrophysiologische Krankheitsursachen, die zu unterschiedlichen Schmerzphänotypen führen können. Zelluläre Veränderungen durch Gb3 Ablagerungen können nun mittels neuester Mikroskopietechniken anhand der von uns generierten Neurone untersucht werden um ein besseres Verständnis der zugrundeliegenden Pathophysiologie zu bekommen. Zusammenfassend bietet unser System eine neue Möglichkeit den neuronalen Einfluss verschiedener *GLA* Mutationen auf einer funktionellen und molekularen Ebene zu untersuchen und die Diversität von M. Fabry aufzuschlüsseln.

3 Introduction

3.1 Fabry disease

Fabry disease (FD) is a rare X-linked lysosomal storage disorder caused by mutations in the gene encoding α-galactosidase A (GLA). Prevalence rates are ranging from 1:40,000 (Desnick et al., 2003) to 1:117,000 (Schiffmann, 2009) since large epidemiological studies are lacking. Hence, current epidemiologic data are highly dependent on the respective geographical region. A screening of male newborns in Italy, for example, showed a prevalence rate of 1:3,100 (Spada et al., 2006), whereas in the United Kingdom, a prevalence of 1:366,000 was found (MacDermot et al., 2001). Due to the X-linked inheritance, hemizygous men are earlier and more severely affected than heterozygous women (Wilcox et al., 2008). FD pathophysiology is based on the insufficient hydrolysis of α-galactose moieties which leads to the accumulation of glycosphingolipids, such as globotriaosylceramide (Gb3) in various tissues including the central and peripheral nervous system (CNS, PNS), kidneys, heart, eyes, and skin. Gb3 accumulation cause a broad range of complications, e.g. nephropathy, cardiomyopathy with arrhythmia, early-onset cerebral stroke, and FD-associated pain based on small fiber pathology (Germain, 2010). Due to the multisystem nature of FD and early involvement of the cardiovascular, renal, and cerebrovascular systems, life expectancy is reduced by 16.2 years in male and 4.6 years in female patients (Waldek et al., 2009).

3.1.1 Genetic background of FD

FD is caused by >900 different mutations with numbers rising (http://www.hgmd.cf.ac.uk). Substitutions, deletions, or insertions of nucleotides in a gene can lead to either nonsense, missense, or silent mutations, with the latter having no pathophysiological impact. Nonsense mutations may cause a premature termination codon and result in a shortened protein primary structure and thus in nonfunctional protein. Missense mutations do not lead to stop codons and therefore result in a full-length protein. Alterations in the catalytic center are particularly critical, or misfolding of the protein due to subsequent changes in the protein secondary and tertiary structure (Rodgers, 2011). This may result in degradation of the instable enzyme, or a decreased enzymatic activity (Filoni et al., 2010). This variety of mutations and effects on protein GLA likely leads to the manifestation of either a classical or nonclassical FD phenotype. Patients with the latter usually show a late-

onset and milder phenotype, whereas classical FD patients are affected early and severely (Arends et al., 2017).

3.1.2 Small fiber pathology in FD

In FD, the PNS is mainly impaired in terms of a small fiber pathology caused by a damage to the thinly-myelinated A-δ and unmyelinated C nerve fibers (Laaksonen et al., 2008). Patients develop thermal hypoesthesia with elevated warm and cold detection thresholds in functional tests such as quantitative sensory testing (Üçeyler et al., 2013). Morphologically, reduction of the intraepidermal nerve fiber density (IENFD) in skin punch biopsies may be found, while nerve conduction studies remain normal in the majority of patients pointing to an involvement of the small, rather than large nerve fibers (Scott et al., 1999). The major symptom in FD is triggerable acral burning pain, which is one of the earliest and most impairing manifestation starting in childhood and affecting men and women with FD (Burlina et al., 2011).

3.1.3 FD-associated pain

Episodic acral burning pain is a hallmark of FD starting in early childhood and affecting both genders (Üçeyler et al., 2014). Typical triggers are fever, physical activity, and heat. Pain character, distribution, and triggerability hint towards neuropathic pain, however, nociceptive components are also discussed (Üçeyler et al., 2019).

FD-associated pain is clinically diverse and can be categorized into four different phenotypes: acral evoked pain, comprising allodynia (i.e. pain triggered by usually non-painful stimuli) and hyperalgesia (i.e. increased pain upon painful stimuli), is the most common phenotype. Pain attacks are frequently reported by FD patients and are triggered by external stimuli and typically lead to acral burning pain. Avoidance or elimination of such triggers usually leads to an attenuation of pain. Fabry crisis is a rare, but extreme form of FD pain and is characterized by excruciating pain that may spread all over the body sometimes lasting for days. FD crises are often resistant to analgesic medication and patients need to be hospitalized. Chronic permanent pain is scarce in FD and mostly of mild to moderate intensity (Üçeyler et al., 2014). FD-associated pain has a great impact on health-related quality of life and the current treatment options are limited due to lack of knowledge on the underlying pathomechanisms linking Gb3 with FD pain.

3.1.4 Diagnostic criteria for FD

As a rare disease with variable phenotype, FD diagnosis if often delayed. The diagnosis is made by determination of plasma GLA activity, which is reduced in male patients and mostly normal in heterozygous female patients (Tsukimura et al., 2014). Hence, genetic analysis for pathogenic mutations in the *GLA* gene is mandatory to confirm diagnosis in men and women. If the diagnosis cannot be established, organ biopsies taken from kidneys or the heart is recommended for the histological detection of pathognomonic Gb3 accumulation (Schiffmann et al., 2017). Besides investigation of GLA activity and genetic analysis, plasma lyso-Gb3 levels have been established as potential prognostic marker in FD patients (Aerts et al., 2008) with high levels indicating a classical phenotype in men and women (Tsukimura et al., 2014).

3.1.5 FD-specific and analgesic treatment

Due to the unknown mechanisms linking Gb3 depositions with FD symptoms, treatment is focused on reduction of these accumulations using enzyme replacement therapy (ERT) or the recently established chaperone therapy. ERT is administered intravenously and biweekly using recombinant agalsidase-α (Eng et al., 2001b) or agalsidase-ß (Schiffmann et al., 2001). Both drugs are similar in their pharmacological properties and increase systemic levels of functional GLA. ERT reduces Gb3 load in plasma, urine, skin, heart, and kidneys, whereas data about the analgesic effect of ERT is inconclusive (Eng et al., 2001a; Schiffmann et al., 2001; Alegra et al., 2012).

Another treatment approach is to increase endogenous enzyme activity by oral administration of the chaperone migalastat. Migalastat is an iminosugar analogue, which binds to the active site of GLA and stabilizes the tertiary structure of the enzyme ensuring proper intracellular trafficking to the lysosomes (Fan et al., 1999). Migalastat dissolves in the acidic lysosomal environment, restoring enzymatic activity and leading to degradation of Gb3 (Germain et al., 2016). A major advantage of migalastat is its oral intake, while its efficacy is dependent on the type of *GLA* mutation and is only suitable for approximately 50% of FD patients with amenable missense mutations (http://www.galafoldamenabilitytable.com). Hence, migalastat can only be effective, if the mutation leads to a misfolding of GLA, but the endogenous catalytic activity is still preserved (Giugliani et al., 2013). Long-term data

on reduction of pain is sparse and current data are inconclusive (Hughes et al., 2017).

Another promising novel treatment option is the iminosugar lucerastat applied for substrate reduction therapy, which inhibits the glucosylceramide synthase, leading to a reduction of the metabolic precursor of Gb3 and thus preventing accumulations (Guerard et al., 2018). Lucerastat is currently tested in a phase III clinical trial in which its efficacy, safety, and effect on neuropathic pain in FD is investigated (https://clinicaltrials.gov; Identifier: NCT03425539).

In the majority of cases, FD pain is not relieved by FD-specific treatment, hence, symptomatic analgesic medication is needed. Since randomized-controlled-trials are lacking, FD patients are treated following the guidelines for the treatment of neuropathic pain (Baron et al., 2010; Rolfs, 2013). Observing renal and cardiac contraindications, sodium channel blockers such as carbamazepine or phenytoin are recommended as first line analgesic treatment (Politei et al., 2016).

3.1.6 Pathophysiology of FD pain and small fiber pathology

Pathomechanistic research in FD is hindered by the lack of suitable human biomaterial that cannot be obtained easily *in vivo*. Although tissue collected during organ biopsies or *post mortem* can be used to investigate morphological changes, insight into disease mechanisms is limited. Hence, GLA deficient mouse models (GLA KO) were established to examine the effect of Gb3 depositions *in vivo* (Ohshima et al., 1997). GLA KO mice age-dependently develop thermal hyposensitivity and show hints for spontaneous pain behavior, resembling the human disease phenotype (Üçeyler et al., 2016). Age dependent Gb3 accumulations in GLA KO mice were detected in multiple cell types, such as dorsal root ganglia (DRG) and trigeminal neurons, or vascular smooth muscle cells, and were associated with mutations causing a classic and non-classic FD phenotype (Bangari et al., 2015). Furthermore, there is evidence for increased apoptosis of sensory neurons which may contribute to skin denervation as also seen in FD patients (Hofmann et al., 2018) and a differentiated gene expression in GLA KO DRG, pointing towards involvement of immune-related pathways in the development of the pain phenotype (Kummer et al., 2017).

However, data obtained from animal studies cannot be transferred to patients directly. To investigate pain pathophysiology, human biomaterial such as DRG neurons is needed, but can only be obtained *post mortem*. Hence, researchers are increasingly utilizing induced pluripotent stem cells (iPSC) to establish individual patient-specific disease models. These models offer the chance to investigate live cells obtained from the patient reflecting individual pathology. However, a specialized *in vitro* model to study the pathophysiology of pain in FD is still missing. Such a model system is of particular interest because FD pain is difficult to analyze in animal models and its source is still elusive. Additionally, generating a universal animal disease model is challenging because of the numerous mutations causing FD. *In vitro* systems, such as iPSC generated tissue may be the next step towards personalized medicine for FD to develop more specific treatment options to alleviate pain and increase patients' quality of life.

3.2 Induced pluripotent stem cells

Pluripotency is defined as the cellular ability to differentiate into any of the three embryonic germ layers: mesoderm, ectoderm, and endoderm (Hanna et al., 2010). This potential is naturally restricted to embryonic stem cells (ESC), which are beneficial for disease modelling, but ethical concerns are a major disadvantage (Lo and Parham, 2009). In 2012, Sir John B. Gurdon and Shinya Yamanaka jointly received the Nobel Prize in Physiology or Medicine, for the discovery that mature cells can be reprogrammed to become pluripotent (https://www.nobelprize.org/). Gurdon discovered that transplanting the nucleus of a somatic cell of *Xenopus laevis* into an enucleated egg of the same species results in viable tadpoles (Gurdon et al., 1958). This experiment gave first evidence that terminally differentiated cells can become pluripotent in the appropriate microenvironment. The breakthrough for modern iPSC research was achieved by Yamanaka and colleagues in 2006, who identified the genes responsible for pluripotent identity, the so called Yamanaka factors (YF) "KMOS": Kruppel-like factor 4 (*Klf4*), *c-Myc*, octamer-binding transcription factor 4 (*Oct4*), sex determining region Y-box2 (*Sox2*), and thus have the ability to reprogram murine somatic cells to iPSC (Takahashi and Yamanaka, 2006). One year after reprogramming mouse fibroblasts, the research group around Shinya Yamanaka generated the first human iPSC from adult fibroblasts, providing the tools for today's iPSC research (Takahashi et al., 2007).

3.2.1 Reprogramming mechanism

A hallmark of iPSC is the expression of pluripotency-associated markers, which are a product of the endogenous pluripotency network. In somatic cells, this network is silenced via epigenetic mechanisms. To achieve pluripotency, these genes have to be reactivated by remodeling the epigenome, achieved by the overexpression of YF. This leads to conformational changes of chromatin, mediated by methylation and acetylation of histones, thus rendering ESC associated genes accessible, but somatic cell specific genes inaccessible for the cellular transcription machinery (Sims et al., 2003). YF replace repressing histone modifications with activating ones on ESC genes, and vice versa for genes, which determine a somatic cell fate (Stadtfeld et al., 2008). The complete reprogramming process can be divided into two major phases (**Figure 1**).

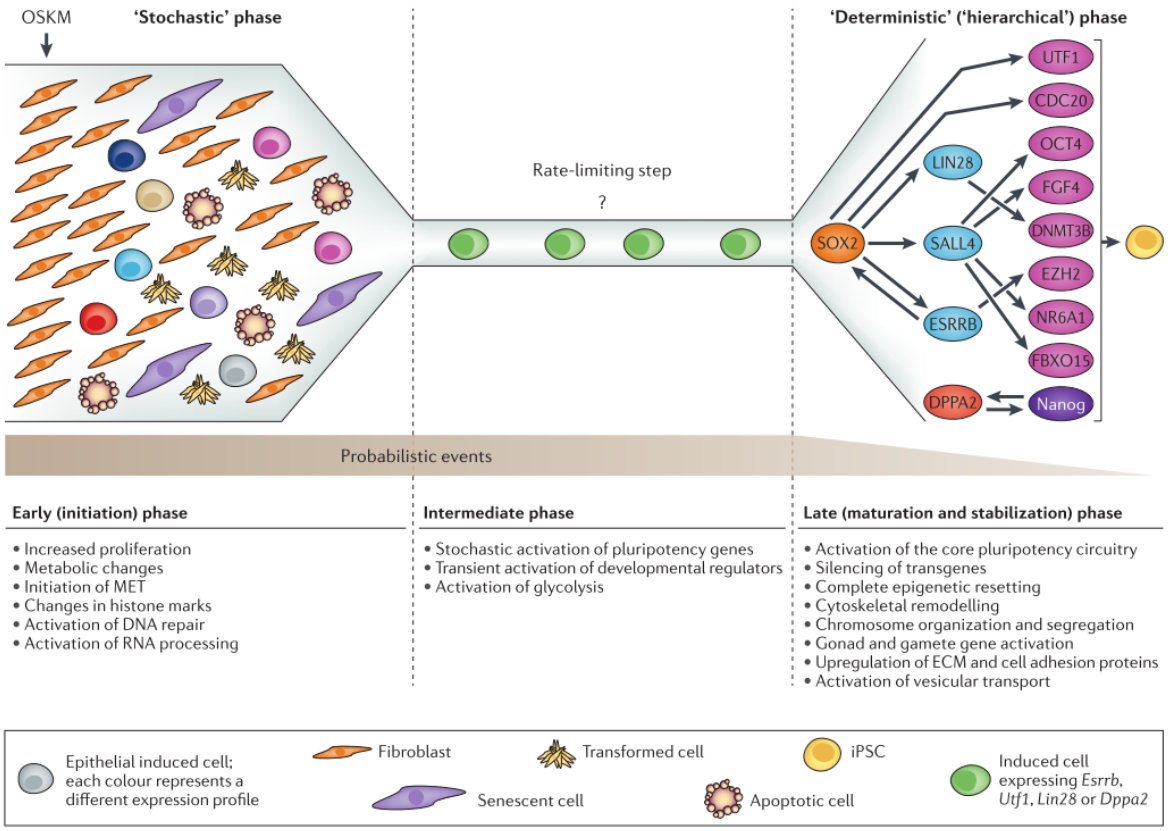

Figure 1: Reprogramming stages. In the stochastic phase, cells acquire different cell fates induced by the overexpression of YF and the underlying transcriptional changes. Cells with a reprogramming fate pass an unknown rate-limiting step and enter the deterministic phase, in which a stable endogenous pluripotency-network is established.
For abbreviations see **page 94**. Adapted by permission from Macmillan Publishers Ltd: Buganim Y., Faddah D.A., and Jaenisch R., Mechanisms and models of somatic cell reprogramming. Nat Rev Genet, 2013. 14(6): p. 427-39, copyright 2013.

Briefly, in the initiation phase, gene expression of the target cells is altered to increase proliferation and metabolism. The stochastic activation and deactivation of several genes leads to multiple cell fates, such as senescence, apoptosis or reprogramming. Cells with an acquired reprogramming fate start activating endogenous pluripotency genes and enter the maturation and stabilization phase. In this phase, the epigenetic remodeling is completed, including X-chromosomal inactivation (XCI) in cells from female donors, resulting in the full reactivation of the endogenous pluripotency network (Buganim et al., 2013). Stable and mature iPSC can maintain pluripotency without exogenous delivery of transcription factors and have the ability of self-renewal.

3.2.2 Reprogramming approaches

In the early phases of iPSC research, YF were introduced into the cells via viral vectors integrating into the genome and causing their overexpression (Takahashi et al., 2007). This can lead to uncontrolled gene disruption (Stadtfeld and Hochedlinger, 2010) or formation of tumors *in vivo (Okita et al., 2007)*, making translational use difficult. Techniques sparing the genome were established by using non-integrating virus vectors, which maintained sufficient expression of YF without integration (Fusaki et al., 2009).

A recent method is expression of the YF via transfection of the cells with mRNA (Warren et al., 2010). The mRNA is quickly degraded after induction and leads to footprint-free iPSC. Current generation reprogramming kits consist of mRNA encoding for KMOS, LIN28, and NANOG for establishing the pluripotency network. The immune evasion factors E3, K3, and B18R, necessary to inhibit the innate immune response of the cells to exogenous RNA are also delivered via mRNA. Micro RNA from the 302/367 cluster are supplemented to increase reprogramming efficiency (Poleganov et al., 2015).

3.2.3 Stem cell niches and differentiation

To maintain a sufficient pool of undifferentiated and differentiated stem cells *in vivo*, stem cell niches provide a specialized compartment, which regulate self-renewal, quiescence, and differentiation. These niches have a unique microenvironment, which is the result of the extracellular matrix (ECM), cell-cell interactions of stem cells with niche cells, and paracrine signaling (Spradling et al., 2008). Thus, mimicking stem cell niches *in vitro* is crucial for stable expansion of iPSC. Simulating paracrine

signaling can be achieved by supplementing the cultivation medium with defined growth factors (Eiselleova et al., 2009). Mouse embryonic fibroblasts, or solubilized basement membrane from extracted Engelbrecht-Holm-Swarm mouse sarcoma cells can be utilized to mimic cell-ECM interaction and paracrine signaling (Hughes et al., 2010).

During embryogenesis, neurulation leads to the formation of the CNS and PNS. To induce neural fate in iPSC, formation of the neuroectoderm is initiated by the inhibition of bone-morphogenetic protein (Lamb et al., 1993), and transforming growth factor beta mediated signaling (Sakaki-Yumoto et al., 2013). Neural crest cells, progenitors for peripheral neurons are derived from the neuroectoderm by inhibition of NOTCH (Endo et al., 2002) and MAPK1/3 (Newbern et al., 2008). Sensory fate is then established by inhibition of the glycogen synthase kinase-3 pathway (Newbern, 2015). During *in vitro* differentiation, these signaling pathways can be modulated by the addition of small molecules, specifically activating, or inhibiting the desired target.

3.2.4 iPSC-based disease and pain models

The ability of iPSC to differentiate into virtually any cell type makes them a powerful tool for translational research and several models have been established for diverse diseases. These range from 2D monotypic cell cultures to 3D organoids, mimicking complex organ structures *in vitro* usually focusing on frequent disorders such as Alzheimer's (Tcw, 2019) or Parkinson's disease (Li et al., 2018). Only few disease models are published concentrating on pain, such as a model for plate-based phenotypic screening for pain, using Ca^{2+} imaging (Stacey et al., 2018), or a personalized medicine approach for erythromelalgia using microelectrode arrays (Namer et al., 2018). A functional neuronal *in vitro* model system for FD is still missing.

3.3 Aim of this study

Due to the inaccessibility of human neuronal material *in vivo*, shortcomings of animal models, and lack of human *in vitro* disease models focusing on FD pain, we aimed at establishing an entirely human neuronal *in vitro* disease model to investigate the underlying mechanisms of FD pain. We hypothesized that we can:

1) Generate and cultivate FD-sensory neurons from skin fibroblasts via iPSC

2) Reconstitute the molecular disease phenotype in patient-specific cells

3) Adapt new techniques for analysis of FD-neurons

4) Identify yet unknown differences in cells from patients with differing pain

4 Materials and Methods

4.1 Equipment and reagents

A list of the utilized technical equipment, reagents, and specific parameters for polymerase-chain reaction (PCR) can be found in the appendices.

4.2 Patients

Three patients were chosen for biomaterial collection and cell reprogramming. Details about genotype and clinical phenotype can be found in **Table 1**.

Table 1: Clinical data of subjects and control person

Line-ID	TK1-iPSC	TK8-iPSC	TK9-iPSC	Ctrl-iPSC
Sex	Female	Male	Male	Male
Age at biopsy	25	28	27	62
GLA activity	0.22 [ref.:0.4 – 1.2 ng/ml/protein]	0.5 [ref.: 3.4 – 13.0 nmol/h/ml]	0.04 [ref.: 0.4 – 1.0 nmol/min/mg protein]	N/A
Genotype	c.708G>C (heterozygous)	c.1069C>T (hemizygous)	c.568delG (hemizygous)	wt
Lyso-Gb3	11.5 [ref.:< 0.9 ng/ml]	57.7 [ref.:< 0.9 ng/ml]	241.0 [ref.: < 2.01 ng/ml]:	N/A
ERT	None	Agalsidase-β	None	N/A
Pain phenotype	Attacks	Attacks	No pain	N/A
Thermal sensory thresholds	Normal	Elevated	Normal	N/A
IENFD at calf (fibers/mm)	8.5*	4.9*	3.7*	N/A

Abbreviations: ERT = enzyme replacement therapy, Gb3 = globotriaosylceramide GLA = Alpha-, IENFD = intraepidermal nerve fiber density, GLA = α-galactosidase A, ref = reference, wt = wildtype

*Normative values at calf according to sample collection in our laboratory: 9 ± 3 fibers/mm.

Additionally, skin from the calf of a 29-year old healthy man was used for Gb3 detection in skin cryosections.

4.3 Immunocytochemistry (ICC)

For conventional ICC experiments, cells were fixed with 4% (v/v) paraformaldehyde (PFA; Electron Microscopy Sciences, Hatfield, PA, USA) in live cell imaging solution (Gibco, Waltham, MA, USA) for 20 min at room temperature (RT), washed three times with Dulbecco's phosphate buffered saline ($DPBS^{+/+}$; Sigma-Aldrich, St. Louis, MS, USA) and blocked with 5% (v/v) fetal calf serum (FCS; Merck, Darmstadt, Germany)/$DPBS^{+/+}$ for 30 min at RT. For super-resolution microscopy, cells were fixed for 1 h at RT with 5% (v/v) glyoxal (pH=5), quenched with 100 mM glycine for 30 min and blocked as described above (both Sigma-Aldrich, St. Louis, MS, USA). For intracellular targets, 0.1% (w/v) saponin (Sigma-Aldrich, St. Louis, MS, USA) was added to the blocking buffer for membrane permeabilization. Primary antibodies were diluted (see **Table 8**) in the blocking solution and cells were incubated for 16 h at 4°C. After washing three times with $DPBS^{+/+}$, the corresponding secondary antibody (see **Table 9**), diluted in $DPBS^{+/+}$ was added to the cells and incubated for 30 min at RT. Shiga toxin 1, B subunit (STxB)::555 or STxB::647, detecting Gb3 and globotetrahexosylceramide (Gb4), kindly provided by the Department of Biotechnology and Biophysics, Würzburg (Prof. Markus Sauer), was added to the secondary antibody, where applicable. Cells were incubated with 700 nM 4',6-diamidino-2-phenylindole (DAPI; Sigma-Aldrich, St. Louis, MS, USA) for 5 min, washed with $DPBS^{+/+}$ and mounted with Aqua-Poly/Mount (Polysciences, Warrington, PA, USA), or ProLong™ Glass Antifade (Thermo Fisher Scientific, Waltham, MA, USA) for super-resolution imaging.

4.3.1 Labeling of extracellular targets

Live cells were incubated on ice for 20 minutes with 5 µM double knot toxin-His_6 (DkTx; Mybiosource.com, San Diego, CA, USA), washed three times with $DPBS^{+/+}$, followed by the previously described routine ICC protocols for multiplex labeling. An

Anti-His::647 antibody (GenScript Biotech, Nanjing, China) was used for detection of DkTx.

4.3.2 *d*STORM imaging

One week before analysis, 5 week old neurons were replated on 8-well cell culture glass chamber slides (Sarstedt, Nürnbrecht, Germany) and cultivated for 1 week, as usual. Cells were incubated live with 5 µg/ml Cholera toxin B subunit (CTxB; Sigma-Aldrich, St. Louis, MS, USA) conjugated with Alexa Fluor 647 (Thermo Fisher Scientific, Waltham, MA, USA) for 15 min, washed with PBS and fixed with 2% PFA/0.2% glutaraldehyde (Sigma-Aldrich, St. Louis, MS, USA). 100 mM cysteamine was used as switching buffer (Sigma-Aldrich, St. Louis, MS, USA). Images were reconstructed using the ThunderSTORM plugin for ImageJ (Ovesny et al., 2014).

4.4 Immunohistochemistry

Skin tissue from skin punch biopsies were fixed, embedded in Tissue-Tek® O.C.T.™ (Sakura, Tokyo, Japan), and cut in 40-µm sections using a cryostat (Leica Microsystems, Wetzlar, Germany). Sections were blocked for 30 min at RT with 10% (w/v) bovine serum albumin (BSA; Sigma-Aldrich, St. Louis, MS, USA)/DPBS$^{-/-}$ and STxB::555, diluted in 1% (w/v) BSA/DPBS$^{-/-}$ + 0.1% (w/v) saponin and incubated for 16 h at 4°C. Sections were washed and mounted with VECTASHIELD® antifade mounting medium with DAPI (Vector Labs, Burlingame, CA, USA).

4.5 Imaging setups

Different microscope setups were used for biomaterial analysis.

4.5.1 Conventional epifluorescence

The following systems were used for conventional epifluorescence imaging: Leica DMi8 microscope equipped with a DFC3000G CCD camera, EL6000 light source, and Leica Application Suite X (abbreviated as DMi8 in further sections; all: Leica Microsystems, Wetzlar, Germany). Zeiss Axiophot2, excitation by HXP 120C (Zeiss, Oberkochen, Germany) with a SPOT INSIGHT™ camera and SPOT Software (abbreviated as Axiophot in further sections; both: Diagnostic Instruments, Sterling Heights, MI, USA). Zeiss Imager M.2 with an Apotome 2 device for structured illumination, Colibri 7 LED as light source, an Axiocam 506 mono CCD camera, and Zeiss ZEN Blue edition as software (abbreviated as Apotome in further sections; all: Zeiss, Oberkochen, Germany).

4.5.2 Phase contrast imaging

Images of *in vitro* cultures were acquired with a Leica DMI IL LED inverted microscope, with a DMC2900 CCD camera and Leica Application Suite as software (abbreviated as DMI IL LED in further sections; all: Leica Microsystems, Wetzlar, Germany).

4.5.3 Super-resolution and confocal imaging

Structured illumination microscopy (SIM) images were acquired using an Elyra S.1 microscope (Zeiss, Oberkochen; Germany) with a PCO Edge 5.5 cMOS camera (PCO, Kelheim, Germany) and 405 nm, 488 nm, 561 nm, and 642 nm laser lines. Abbreviated as SIM in following sections.

Direct stochastic optical reconstruction microscopy (*d*STORM) experiments were performed with a custom built setup, based on an Axio Oberserver.Z1 body (Zeiss, Oberkochen, Germany) with two Andor EMCCD iXon Ultra DU-897 cameras (Oxford Instruments, Abingdon, UK) and 405 nm, 488 nm, 532 nm, and 640 nm laser lines. Abbreviated as *d*STORM in following sections.

An LSM700 microscope, with two photomultipliers and 488 nm, 555 nm, and 639 nm laser lines (all: Zeiss, Oberkochen, Germany) was used for confocal laser scanning microscopy (CLSM). Abbreviated CLSM in further sections. SIM, CLSM, and *d*STORM images were acquired at the Department of Biotechnology and Biophysics, Würzburg in collaboration with Jan Schlegel, M.Sc.

4.6 Skin punch biopsy and human dermal fibroblast (HDF) cultivation

A six-mm skin punch biopsy was obtained by the treating physician from the locally anesthetized calf following a standard procedure (Üçeyler et al., 2010). Dermis and epidermis were mechanically separated, the dermal part was cut into small pieces and placed in a tissue culture (TC) flask. Fibroblast cultivation medium (DMEM/F12, 120 U/ml penicillin, 100 µg/ml streptomycin [all: Gibco, Waltham, MA, USA], 10% FCS) was added and cells were cultivated at 37°C in 5% CO_2 (v/v). Once HDF grew out of the tissue pieces and were 60-80% confluent, cells were passaged using TrypLE™ Express (Gibco, Waltham, MA, USA). Medium was changed twice a week.

4.7 Reprogramming of HDF to iPSC and clonal expansion

For reprogramming, two different commercially available kits were used. TK1-iPSC were generated using StemMACS™ mRNA reprogramming kit (Miltenyi Biotec, Bergisch Gladbach, Germany) according to manufacturer`s protocol, with the following minor modifications: cells were reprogrammed in a 12-well format instead of the 6-well format. Volumes of reagents were adjusted accordingly (Klein, 2016). TK8 and TK9 iPSC were generated using the StemRNA 3rd Gen reprogramming kit (Reprocell, Kanagawa, Japan), as recommended by the manufacturer.

Anti-TRA-1-60 live cell staining antibody was used (1:100; Miltenyi Biotec, Bergisch Gladbach, Germany) to identify putative iPSC colonies after reprogramming. Colonies were manually picked and initially cultivated in a 24-well plate (TK1 clones), or 12-well plate (TK8, TK9), respectively and expanded to a 6-well cultivation format.

4.8 Cultivation of iPSC

iPSC were cultivated on TC plates, coated with hESC qualified Matrigel® (ES-Mg; Corning, Corning, NY, USA). For coating, 250 µl ES-Mg was diluted in 25 ml ice cold DMEM/F12 medium and 111 µl/cm² was added to the wells and incubated for at least 16 h at 4°C. Before seeding, excessive ECM was aspirated.

StemMACS™ iPS-Brew (Miltenyi Biotec, Bergisch Gladbach, Germany), supplemented with 120 U/ml penicillin and 100 µg/ml streptomycin, called ”iPSC-medium“ in the following sections, was used as cultivation medium. Once cells reached 80% confluency, medium was aspirated, incubated for 8 minutes with 2 mM ethylenediaminetetraacetic acid/DPBS without calcium and magnesium^{-} (EDTA/DPBS$^{-/-}$; Thermo Fisher Scientific, Waltham, MA, USA), and centrifuged (300 rcf, 3 min, RT). Cells were seeded with the desired density in ES-Mg coated wells. 10 µM Y-27632 (ROCKi; Miltenyi Biotec, Bergisch Gladbach, Germany) was added to the iPSC-medium for the first 24 h. Cells were kept at 37°C in 5% CO_2 (v/v) and medium was changed daily. Cells from early passages were cryoconserved in KnockOut™ serum replacement (KO-SR; Thermo Fisher, Waltham, MA, USA), containing 10% dimethyl sulfoxide (DMSO; Sigma-Aldrich, St. Louis, MS, USA) and 10 µM ROCKi, in the gas phase of liquid N_2.

4.9 Characterization of putative iPSC

To ensure high quality iPSC lines, cells were analyzed for various parameters, such as morphology, expression of stemness genes, the potential to differentiate into cell types of the meso-, endo-, and ectodermal germ layers, and genetic integrity.

4.9.1 Trilineage differentiation

For differentiation of iPSC into all three germ layers, the commercial StemMACS™ Trilineage Differentiation Kit, human" (Miltenyi Biotec, Bergisch Gladbach, Germany) was used following the manufacturers' recommendations. Cells were analyzed via immunocytochemistry (ICC, see **section 4.3**) with mesodermal (smooth muscle protein 22 alpha, [SM22A]), endodermal (forkhead box protein A2, [FOXA2]), and ectodermal (sex determining region y-box 2 [SOX2] and paired box protein 6 [PAX6]) markers.

4.9.2 Flow cytometry

Quantitative analysis of the expression of the pluripotency-associated surface markers stage-specific embryonic antigen-4 (SSEA-4) and tumor resistance antigen 1-60 (TRA-1-60) was performed using flow cytometry. $3x10^6$ iPSC were harvested as single cells using accutase (Gibco, Waltham, MA, USA), washed with $DPBS^{-/-}$ and kept on ice for the remaining steps. $1x10^6$ cells were used as the unstained control. The remaining cells were incubated for 15 min at 4°C with Viobility™ 405/452 Fixable Dye (1:1000; Miltenyi Biotec, Bergisch Gladbach, Germany) for live/dead discrimination. Cells were blocked with 5% (v/v) $FCS/DPBS^{-/-}$ by centrifugation (300 rcf, 3 min, 4°C) and $1x10^6$ cells were incubated with TRA-1-60 and SSEA4 antibodies, labelled with allophycocyanin (APC) or phycoerythrin (PE), respectively (both 1:11; Miltenyi Biotec, Bergisch Gladbach, Germany) for 15 min at 4°C. The remaining cells were incubated similarly with matching isotype control antibodies (1:50; REA Control (S)-APC and REA Control (S)-PE; Miltenyi Biotec, Bergisch Gladbach, Germany). Cells were washed with $DPBS^{-/-}$ by three centrifugation steps (300 rcf, 3 min, 4°C). Cells were resuspended in $DPBS^{-/-}$ and analyzed with a BD FACSCanto™ II or BD LSR II flow cytometer with FACSDiva™ software (all BD Bioscience, East Rutherford, UK).

For data acquisition, the background signal was evaluated using the unstained and the isotype control and gated accordingly. Only living single cells were included,

using the live/dead discrimination and forward/side scatter. Final analysis was performed using FlowJo v10 software (FlowJo, Ashland, OR, USA).

4.9.3 Sanger sequencing

To verify the presence of the disease associated mutation, genomic DNA (gDNA) from $3x10^6$ iPSC was purified using the DNeasy Blood & Tissue kit (Qiagen, Venlo, Netherlands), as recommended by the manufacturer. PCR was set up as stated in with the corresponding primers (see **Table 7**; Sigma Aldrich, St. Louis, MS, USA) for the mutation using One*Taq*® Hot Start 2X Master Mix with standard buffer, as recommended by the manufacturer (New England Biolabs, Ipswich, MS, USA). PCR products were sent to Eurofins Scientific (Luxembourg, Luxembourg) for purification and Sanger sequencing. Data was analyzed using DNA Baser v4 software (Heracle BioSoft, Pitesti, Romania).

4.9.4 Mycoplasma detection

iPSC were monitored for mycoplasma contamination using a PCR-based assay. Conditioned medium was collected, centrifuged (5000 rcf, 5 min, RT), supernatant aspirated, resuspended in 100 µl lysis buffer (see **Table 5**), and incubated for 5 min at 90°C. 100 µl of 40 mM TrisHCl (Sigma Aldrich, St. Louis, MS; USA) was added to neutralize the lysis buffer and the sample was centrifuged (5000 rcf, 1 min, RT). Isolated DNA was amplified using PCR with *mycoplasma* genus specific primers (see **Table 7**) and analyzed using agarose gel electrophoresis. The positive control consisted of purified DNA from a contaminated culture.

4.10 TK1-iPSC GLA transcriptomics and XCI

To investigate the presence of the mutated GLA on a transcriptional level, total RNA from TK1-iPSC was extracted and translated into cDNA, as described (see **section 4.13**). The mutation site was amplified using PCR (see **Table 7**) and sequenced, as described (see **section 4.9.3.**)

XCI was investigated at the Institute of Human Genetics, University of Würzburg (Prof. Eva Klopocki) using a methylation sensitive HhaI enzyme digestion assay (Promega, Madison, WI, USA).

4.11 Differentiation of iPSC into sensory neurons

A previously published protocol was modified and adapted to generate iPSC derived sensory neurons (Eberhardt et al., 2015). For differentiation experiments, TC plates were coated using Growth Factor Reduced Matrigel® (bMg; Corning, Corning, NY, USA), as previously described (see **section 4.8**), but diluting 500 µl bMg in 25 ml medium.

Medium was changed daily until day 10 of the differentiation. On day -2 of the differentiation, iPSC were harvested when 80-90% confluence was reached, by incubation of the cells with 600 µl accutase for 8 min at 37°C. The single cell suspension was centrifuged (300 rcf, 3 min, RT) resuspended in iPSC cultivation medium with 10 µM ROCKi, and 125,000 cells/cm² were seeded and cultivated for 2 d, as usual. On day 0, medium was switched to differentiation (KSR) medium (KO DMEM/F12, 15% KO-SR, 2 mM GlutaMAX™, 100 µM β-mercaptoethanol, 1% minimum essential medium non-essential amino acids, 100 U/ml penicillin, 100 µg/ml streptomycin [all Thermo Fisher Scientific, Waltham, MA, USA]) supplemented with 2i (100 nM LDN193189 [Stemcell Technologies, Vancouver, Canada], 10 µM SB431542 [Miltenyi Biotec, Bergisch Gladbach, Germany]) for 2 d, followed by 2 d with KSR, supplemented with 5i (100 nM LDN193189, 10 µM SB431542, 10 µM SU5402, 10 µM DAPT [both Sigma-Aldrich, St. Louis, MS, USA], and 3 µM CHIR99021 [Axon Medchem, Groningen, The Netherlands]). Beginning from day 4, N2 medium (DMEM/F12 + GlutaMAX™, B-27 Plus, N-2 Supplement [all: Thermo Fisher Scientific, Waltham, MA, USA], 100 U/ml Penicillin, 100 µg/ml streptomycin) with 5i was added to KSR-5i medium in 25% increments, every other day, until day 9. On day 10, cells were detached using incubation at 37°C with TrypLE™ Express and centrifuged (300 rcf, 3 min, RT). The cell pellet was resuspended in maturation medium (N2 medium, supplemented with 200 ng/ml ascorbic acid [Sigma Aldrich, St. Louis, MS, USA], 20 ng/ml beta-nerve growth factor [βNGF], 20 ng/ml brain-derived neurotrophic factor [BDNF] and 20 ng/ml glial cell line-derived neurotrophic factor [GDNF; all from Peprotech, Rocky Hill, NJ, USA]), spiked with 10 µM floxuridine (FdU, Santa Cruz Biotechnology, Dallas, TX, USA), and seeded either onto bMg coated high precision cover glass (Paul Marienfeld, Lauda Königshofen, Germany) or TC plates for subsequent analysis. Additionally to FdU, 1 µg/ml Mitomycin C (Stemcell Technologies, Vancouver, Canada) and CultureOne Supplement (Thermo

Fisher Scientific, Waltham, MA, USA) were tested as cytostatics. Half of the medium was changed at least once a week, depending on media consumption, as indicated by the phenol red pH indicator, present in the medium. Neurons were cultivated for at least 6 weeks (“mature neurons”) before analysis, unless otherwise stated. Replating of mature neurons was performed as described for day 10, including FdU treatment, but using conditioned medium instead of fresh maturation medium. One week old neurons are defined as “young” in the following sections.

4.12 Functional tests of iPSC-derived sensory neurons

Cultivated neurons were investigated for their response to ERT and the pro-inflammatory cytokine tumor necrosis factor-α (TNF) as potential pain trigger *in vivo* (Üçeyler et al., 2019).

4.12.1 Incubation with agalsidase-β

Neurons were incubated with 1.32 µg/ml agalsidase-β (Sanofi, Paris, France) to investigate the pharmacological response as follows: conditioned medium was collected from neurons, mixed 1:1 with fresh maturation medium, containing 2.64 µg/ml agalsidase-β and added to the neurons for 24 h. Cells were directly analyzed afterwards. For the untreated cells, medium was changed as described, lacking agalsidase-β

4.12.2 Incubation with TNF

To mimic an inflammatory environment as one of the major pain triggers in FD patients, mature neurons were challenged with TNF for 72 h (Üçeyler et al., 2019). Briefly, TNF was reconstituted in H_2O and diluted in 6% (w/v) trehalose (both Sigma-Aldrich, St. Louis, MS, USA). A mixture, containing 50% conditioned and 50% fresh maturation medium was used to dilute the compound to a final concentration of 1000 U/ml and neurons were incubated for 72 h at 37°C and 5% CO_2 (v/v). Neurons were incubated with 6% trehalose lacking TNF as the negative control. Cells were fixed, processed for ICC (see **section 4.3**) and Gb3 accumulations were quantified (see **section 4.12.3**).

4.12.3 Quantification of neuronal Gb3 accumulations

Neurons were fixed and stained, as described (see **section 4.3**) with an antibody against class III β-tubulin (TUJ1; Abcam, Cambridge, UK) and STxB::555 (Sigma-Aldrich, St. Louis, MS, USA). Whole coverslips were scanned using a DMi8 inverted

microscope, with a 20X objective (Leica Microsystems, Wetzlar, Germany, **Figure 2 A**). 150 $TUJ1^+$ cells were counted per sample using the cell counter plugin for ImageJ (National Institute of Health, New York City, NY, USA). STxB positive accumulations were determined in the same manner and diversified into four subgroups (see **Table 2**). A person not otherwise involved in the project and blinded as to sample allocation (Bettina Vignolo, B.Sc.) analyzed images.

Table 2: Diversification of STxB accumulations

Accumulation subgroup	**Characteristics**
No signal	Complete absence of STxB accumulations (**Figure 2 B**)
Focal	Small, highly intense, confined accumulations (**Figure 2 C)**
Scattered	Many accumulations spread out in the whole soma (**Figure 2 D)**
Mixed	Cells with scattered and focal accumulations (**Figure 2 E**)
Total	Sum of mixed, scattered, and focal accumulations

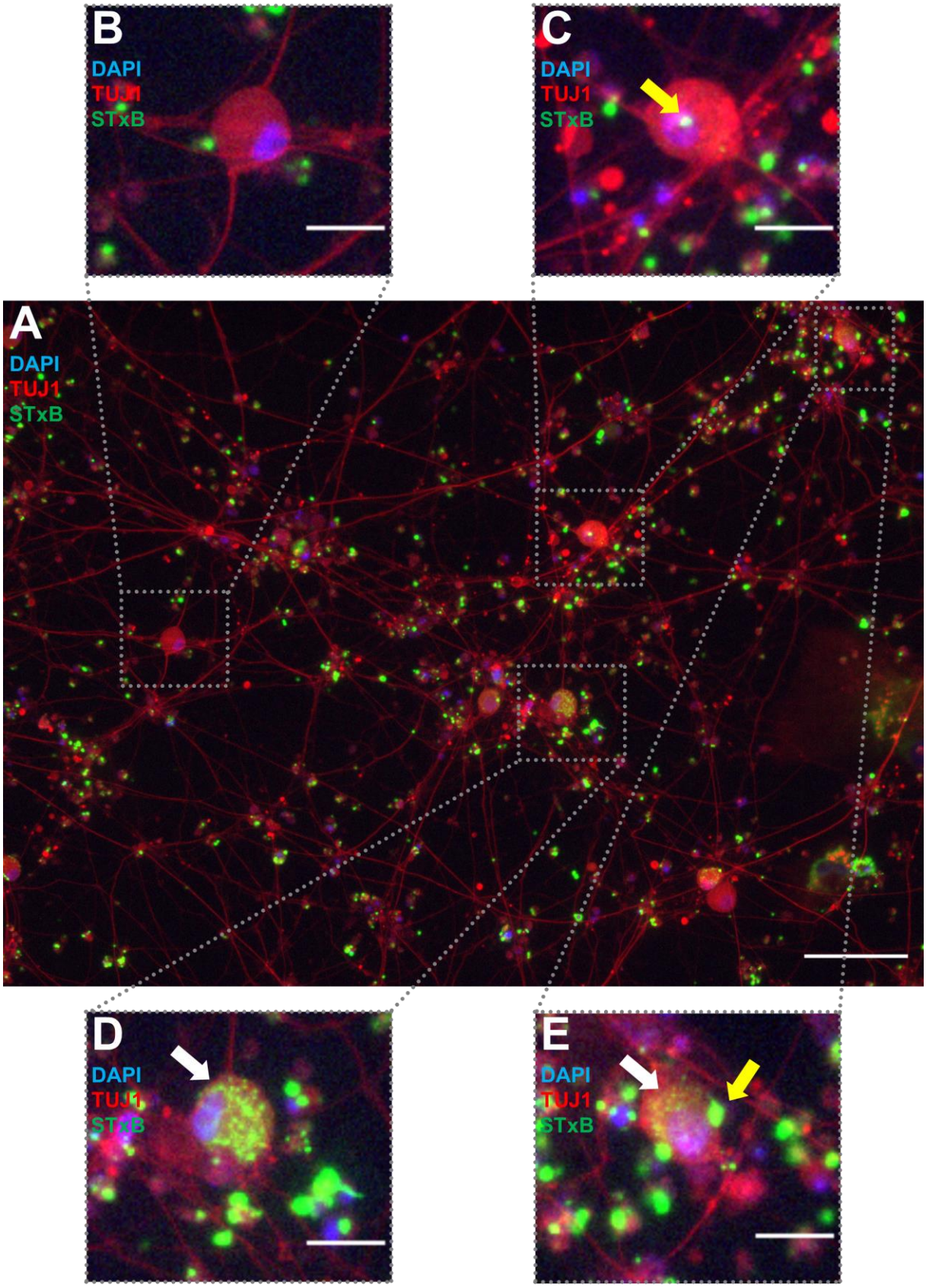

Figure 2: Classification of Gb3 accumulations. (A) Exemplary image for quantification. (B) No accumulations, (C) focal (yellow arrow), (D) scattered (white arrow), and (E) cells with mixed accumulations. Scale bars: 100 µm (A); 25 µm (B-D). All acquired with DMi8.

Abbreviations: DAPI = 4′,6-diamidino-2-phenylindole; TUJ1 = neuron-specific class III β-tubulin; STxB = Shiga Toxin1, B subunit

4.12.4 Confocal Ca^{2+} imaging

One week before analysis, 5 week old neurons were replated on 8-well cell culture glass chamber slides (Sarstedt, Nürnbrecht, Germany) and cultivated for 1 week, as usual. Cells were loaded with 2 µM Fluo-8 AM (Abcam, Cambridge, UK) for 1 h at 37°C, washed with conditioned medium and acquired with the CLSM setup in a live-cell acquisition chamber (Tokai Hit, Shizuoka, Japan) under physiological conditions (5% [v/v] CO_2, 37°C medium, 39°C heated lid). Data was collected with a sampling rate of 0.25 Hz for a total of 8 minutes. Data was analyzed using the open source NA^3 software (Prada et al., 2018).

4.12.5 Patch clamp analysis

Data acquisition and analysis for patch clamp experiments were performed by Dr. Lukas Hofmann in our laboratory.

Mature neurons were transferred into the recording chamber, containing bath solution (see **Table 5**) at RT. Borosilicate glass capillaries (Kimble Chase Life Science and Research Products, Meiningen, Germany) were pulled and heat-polished to patch pipettes with an input resistance of 1 – 4 MΩ containing pipette solution (see **Table 5**). Whole cell current clamp was recorded with an EPC10 patch clamp amplifier with a sampling rate of 20 kHz and data was acquired and analyzed using Patch Master software (both: HEKA, Ludwigshafen, Germany). To quantify action potentials (AP), neurons were stimulated with a single current pulse for 10 ms. Action potential threshold difference ($V_{ThresholdDiff}$) was calculated by subtracting the resting membrane potential (V_{Mem}) from the threshold potential ($V_{Threshold}$) to quantify the degree of neuronal excitability.

4.13 Quantitative real-time PCR (qRT-PCR) experiments

Total RNA was extracted from neurons using the miRNeasy Micro Kit and from iPSC using the miRNeasy Mini Kit (both Qiagen, Hilden, Germany) and 250 ng RNA was reverse transcribed into cDNA applying TaqMan reverse transcription reagents (Thermo Fisher Scientific, Waltham, MA, USA), as recommended by the manufacturers. 5 ng cDNA was used for gene expression studies using TaqMan probes (**Table 6**) with 18S ribosomal RNA as endogenous control (all: Thermo Fisher Scientific, Waltham, MA, USA).

Data was acquired with a QuantStudio™ 3 Real-Time PCR system with technical triplicates and analyzed using QuantStudio™ Design and Analysis software (both Thermo Fisher Scientific, Waltham, MA, USA) applying the ΔC_T method, normalizing expression of markers in iPSC to 1 and using the $^1/_{\Delta C_T}$ value for visualization.

4.14 Statistical analysis

IBM SPSS Statistics Version 26 software (IBM, Armonk, NY, USA) was used for statistical analysis. Data was analyzed using the non-parametric Mann-Whitney U test, after the Kolmogorov-Smirnov test showed a non-normal distribution. Results were visualized using GraphPad Prism 8 (GraphPad Software, San Diego, CA, USA) as interleaved bar (**Figure 16**, **Figure 22**) and interleaved scattered plots (**Figure 18, Figure 19, Figure 20, Figure 21**). Data points represent mean ± standard deviation, as appropriate.

5 Results

5.1 Generation and characterization of one female FD-iPSC line

First, we characterized our female FD-iPSC line. After initial reprogramming of HDF (**Figure 3 A**) and expansion of a single putative iPSC clone, cells showed ESC-like morphology with small, compact cells with a high nucleus:cytoplasm ratio with defined colony borders (**Figure 3 B**). Genetic analysis showed no chromosomal aberration as shown by G-banding (**Figure 3 C**). Expression of the pluripotency markers TRA-1-60, OCT4 and SSEA4 was confirmed by ICC (**Figure 3 D**). Quantitative analysis of TRA-1-60 and SSEA4 showed a coexpression on >94% of live single cells, proofing a homogenous expression (**Figure 3 E**). The disease associated mutation was present in TK1-iPSC, but not in Ctrl-iPSC (**Figure 3 F**). Directed differentiation into meso-, endo-, and ectodermal lineage resulted in cells expressing the germ-layer specific markers SOX2/PAX6 (ectoderm), FOXA2 (endoderm), and SM22A (mesoderm), confirming true pluripotency. No mycoplasma was detected (**supplementary Figure 31 A**)

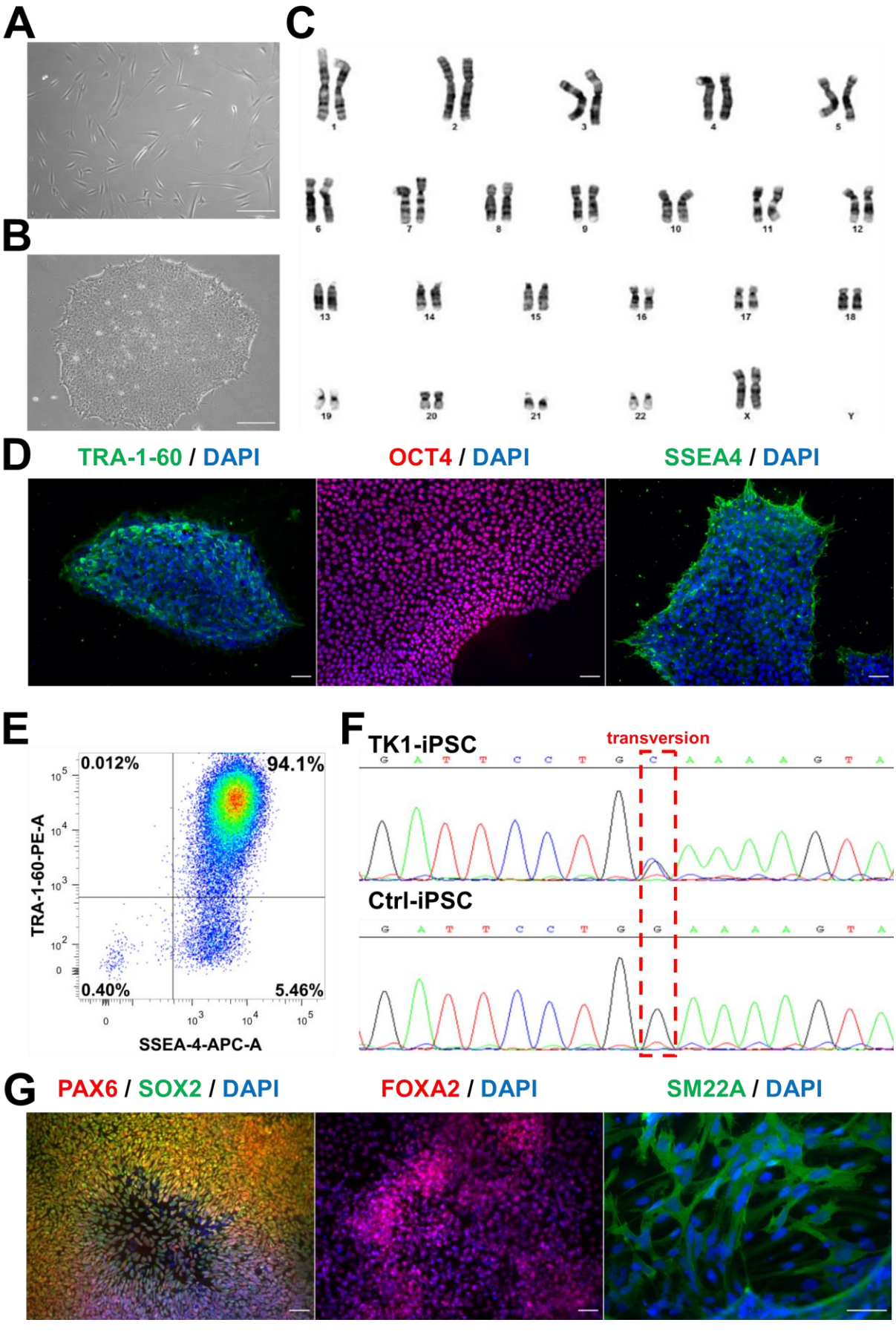
A
B
C
D
TRA-1-60 / DAPI
OCT4 / DAPI
SSEA4 / DAPI
E
0.012%
94.1%
0.40%
5.46%
TRA-1-60-PE-A
SSEA-4-APC-A
F
TK1-iPSC
transversion
Ctrl-iPSC
G
PAX6 / SOX2 / DAPI
FOXA2 / DAPI
SM22A / DAPI

Figure 3: Characterization of a female FD-iPSC line. (A) HDF showed (B) typical ESC-like morphology after reprogramming. (C) No chromosomal aberrations were found and (D) expression of stemness marker was confirmed by ICC qualitatively and (E) quantitatively. (F) The disease associated mutation c.708G>C was present in gDNA. (G) iPSC could be differentiated into cells of all three germ-layers, as shown by immunoreactions against specific markers. Scale bars: 50 µm.; Acquired with DMI IL LED (A, B) and Apotome (D, G).

Abbreviations: APC = allophycocyanin; Ctrl = control; DAPI = 4′,6-diamidino-2-phenylindole; ESC = embryonic stem cell; FOXA2 = forkhead box protein A2; HDF = human dermal fibroblasts; iPSC = induced pluripotent stem cells; OCT4 = octamer-binding transcription factor 4; PAX6 = paired box 6, PE = phycoerythrin; SM22A = smooth muscle protein 22-alpha; SOX2 = sex determining region Y box 2; SSEA4 = stage specific embryonic antigen 4; TRA-1-60 = tumor resistance antigen 1-60

5.2 Gb3 accumulation in TK1-iPSC and neurons

Accumulations were detected with STxB::555 in early (<p5) iPSC (**Figure 4 A**), but not in late (>p5) iPSC (**Figure 4 B**). Furthermore, no difference in the STxB signal was observed between TK1 and control neurons, labelled with peripherin (PRPH; **Figure 4 C, D**)

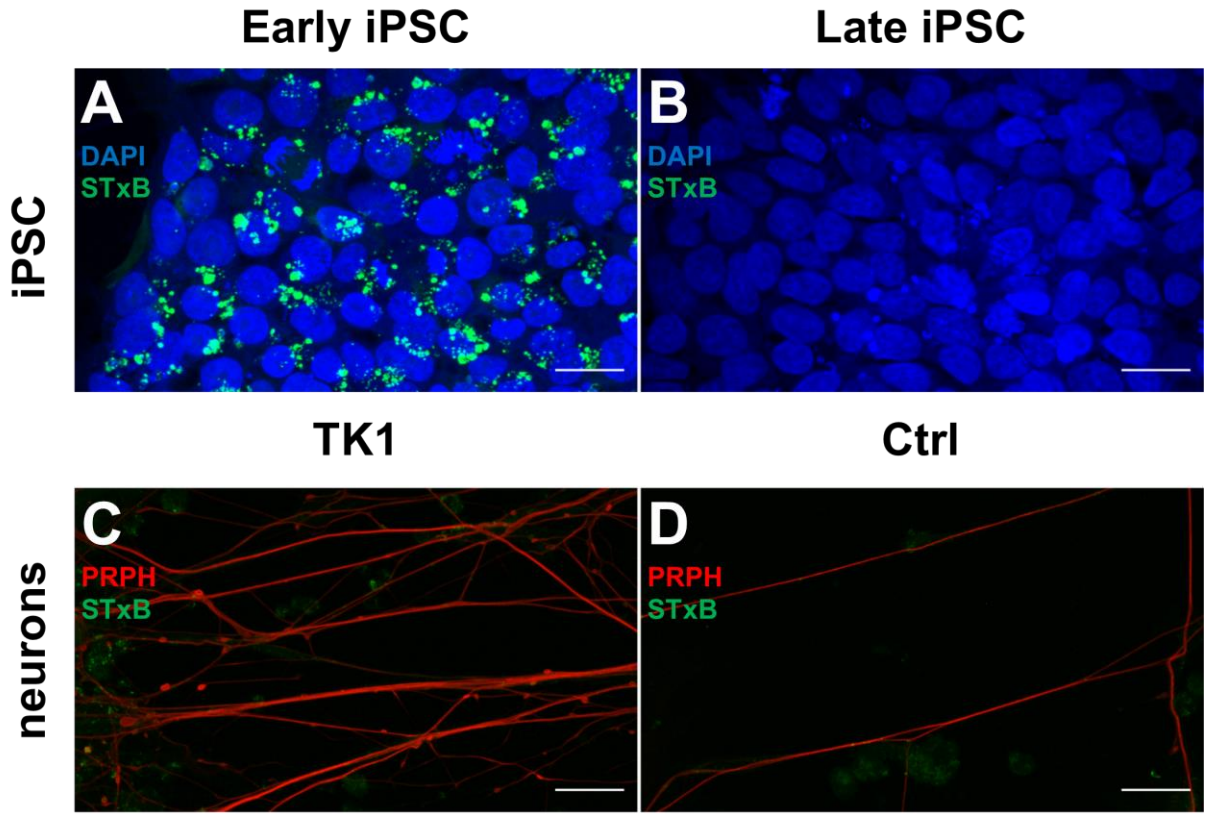

Figure 4: Gb3 accumulations in FD-cells from female subject. (A) StxB-positive profiles could be detected in early (p<5) iPSC, but (B) were missing in late (p>5) iPSC. No accumulations were detected in (C) TK1 iPSC-derived neurons, similar to (D) control iPSC-derived neurons. Scale bars: 25 µm. All aquired with CLSM.

Abbreviations: DAPI = 4′,6-diamidino-2-phenylindole; PRPH = peripherin; STxB = Shiga Toxin 1, B subunit

5.3 gDNA/cDNA analysis for TK1-iPSC

Analysis of *GLA* gDNA of late iPSC showed the presence of the disease-associated mutation c.708G>C, but its absence in cDNA, generated from mRNA specific for the mutation site (**Figure 5 A**). Further investigation of XCI via methylation-sensitive HhaI digestion showed a skewed inactivation towards one genotype in late iPSC, with a ratio of 100:0 (**Figure 5 B**).

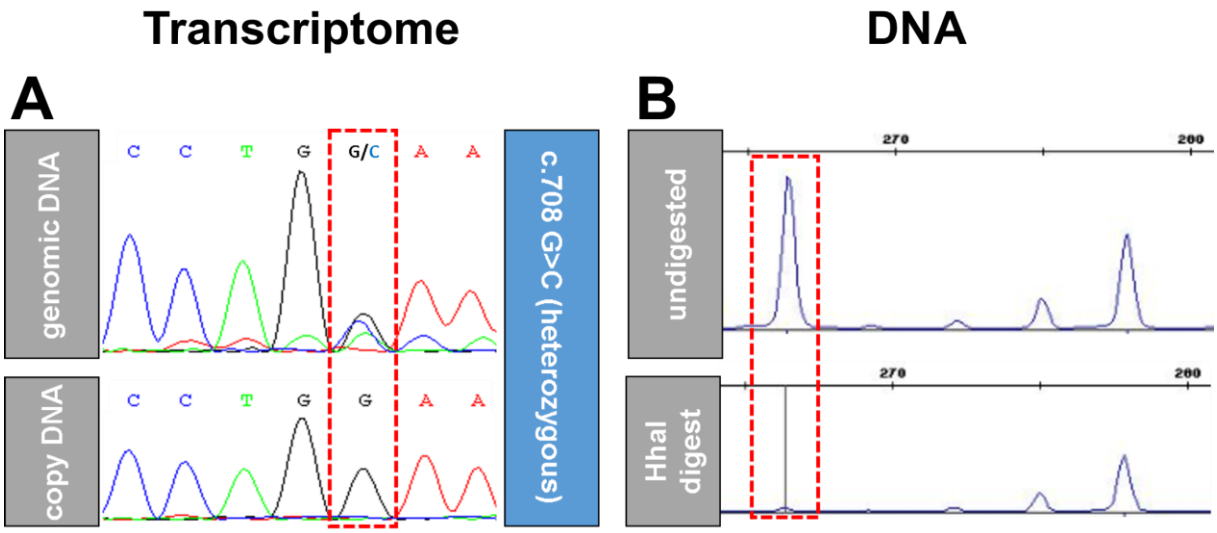

Figure 5: Genetic and transcriptomic analysis of TK1-FD-iPSC. (A) Presence of c.708G>C in the gDNA, but not in cDNA. (B) Full inactivation of one X-chromosome, as shown by methylation sensitive HhaI digestion.

5.4 Gb3 accumulations in male skin samples

Gb3 depositions in skin cryosections were analyzed for TK8, TK9, and a healthy control subject.

As shown in Figure 6, STxB$^+$ profiles are localized in the dermal part of TK8 (**Figure 6 A**) and TK9 (**Figure 6 B**), whereas no signal was detected in the healthy control (**Figure 6 C**). No sample showed accumulations in the epidermal part (**Figure 6 A' – C'**).

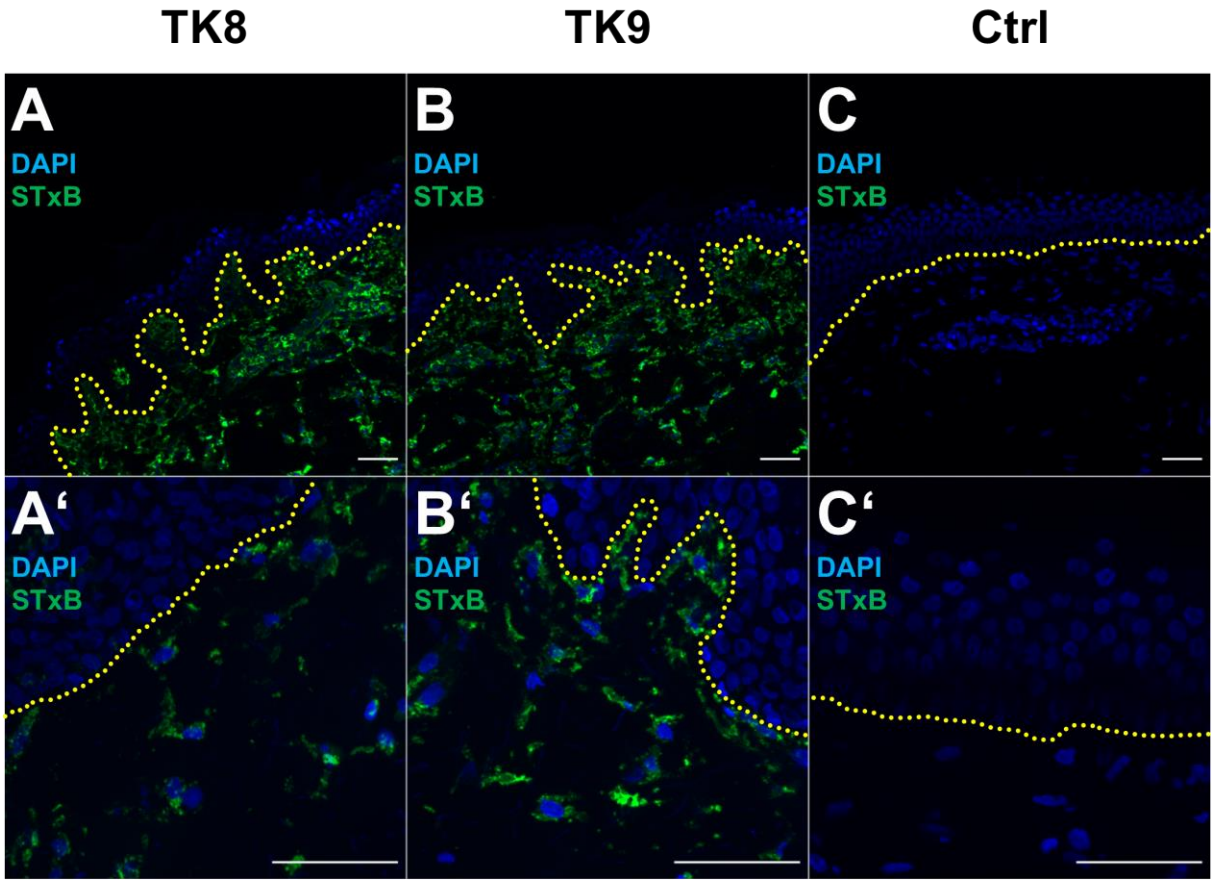

Figure 6: Gb3 accumulations in skin cryosections. Gb3 accumulations are located in the dermal layer of (A) TK8 and (B) TK9. (C) No depositions were detected in the healthy control. (A' – C') Higher magnification of the epidermal – dermal junction (yellow line). Scale bars: 50 µm. All acquired with Apotome. Yellow dotted line marks dermal-epidermal border.

Abbreviations: DAPI = 4′,6-diamidino-2-phenylindole; STxB = Shiga Toxin1, B subunit

5.5 Generation and characterization of four male FD-PSC lines

5.5.1 mRNA reprogramming of TK8

During reprogramming, HDF underwent substantial morphological changes from spindle-shaped cells before transfection (**Figure 7 A**) to compact cells, forming small colonies on the last day of transfection (**Figure 7 B**). Prolonged cultivation for 4 additional days resulted in small demarcated colonies (white arrows), which grew in size (**Figure 7 C**) and density over time until ready for picking and subcultivation (white arrow), 10 days after the last transfection (**Figure 7 D**).

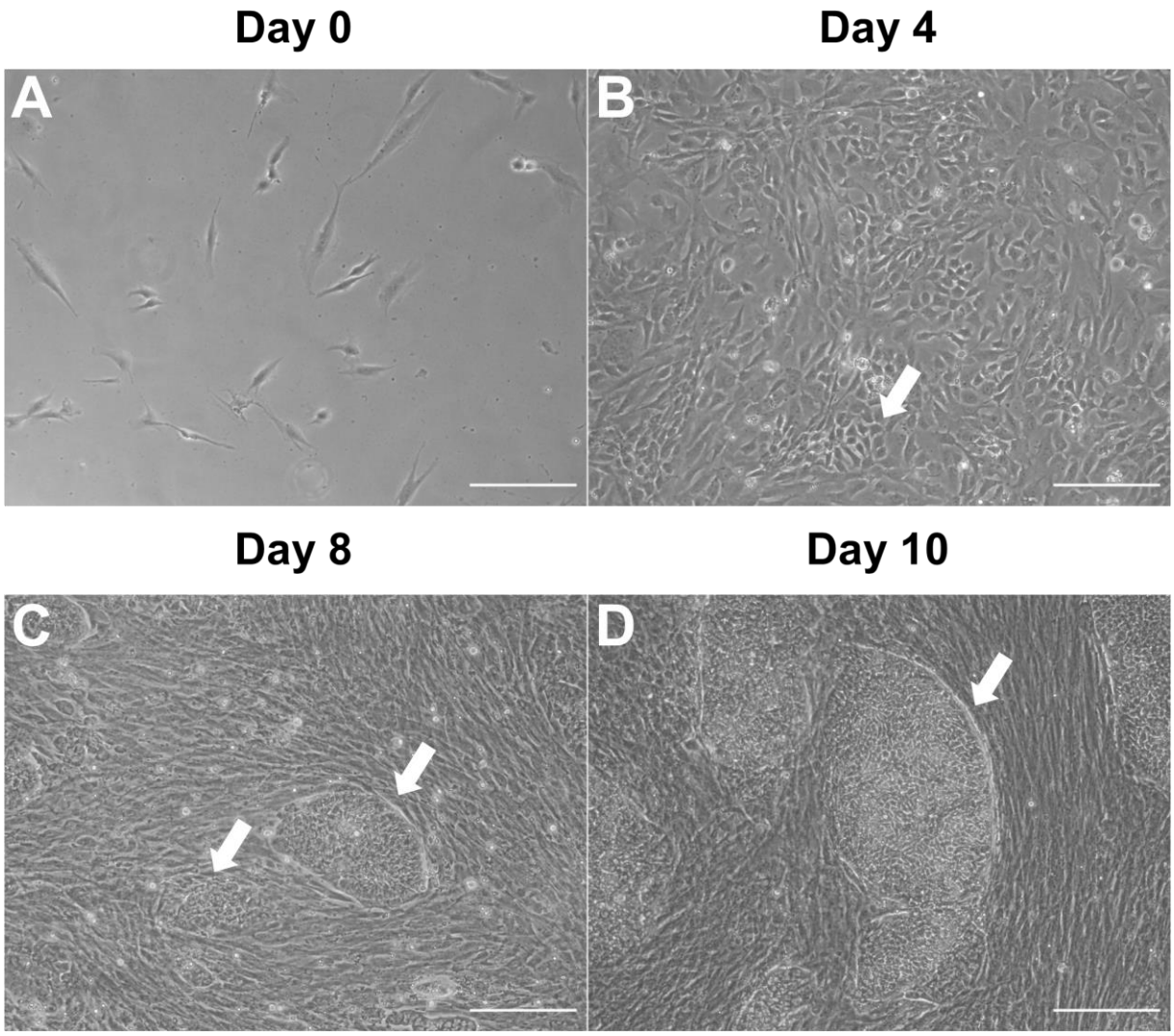

Figure 7: Morphological changes during reprogramming. (A) HDF before transfection, exhibiting typical spindle-shaped cell bodies. (B) After 4 transfections, cells started forming colonies of small and roundish cells, which (C) grew bigger 8 days and (D) became more dense, 10 days after the initial delivery of YF. White arrows indicate emerging putative iPSC colonies. Scale bars: 200 µm. All acquired with DMI IL LED.

Abbreviations: HDF = human dermal fibroblast; iPSC = induced pluripotent stem cells; YF = Yamanka factors

5.5.2 Full characterization of TK8 and TK9 iPSC lines

From each patient TK8 and TK9, two individual clones were chosen for experiments and fully characterized. In this section, data of one clone of each patient is presented; data of the second clone is detailed in the supplementary (see **section 8.8**.):

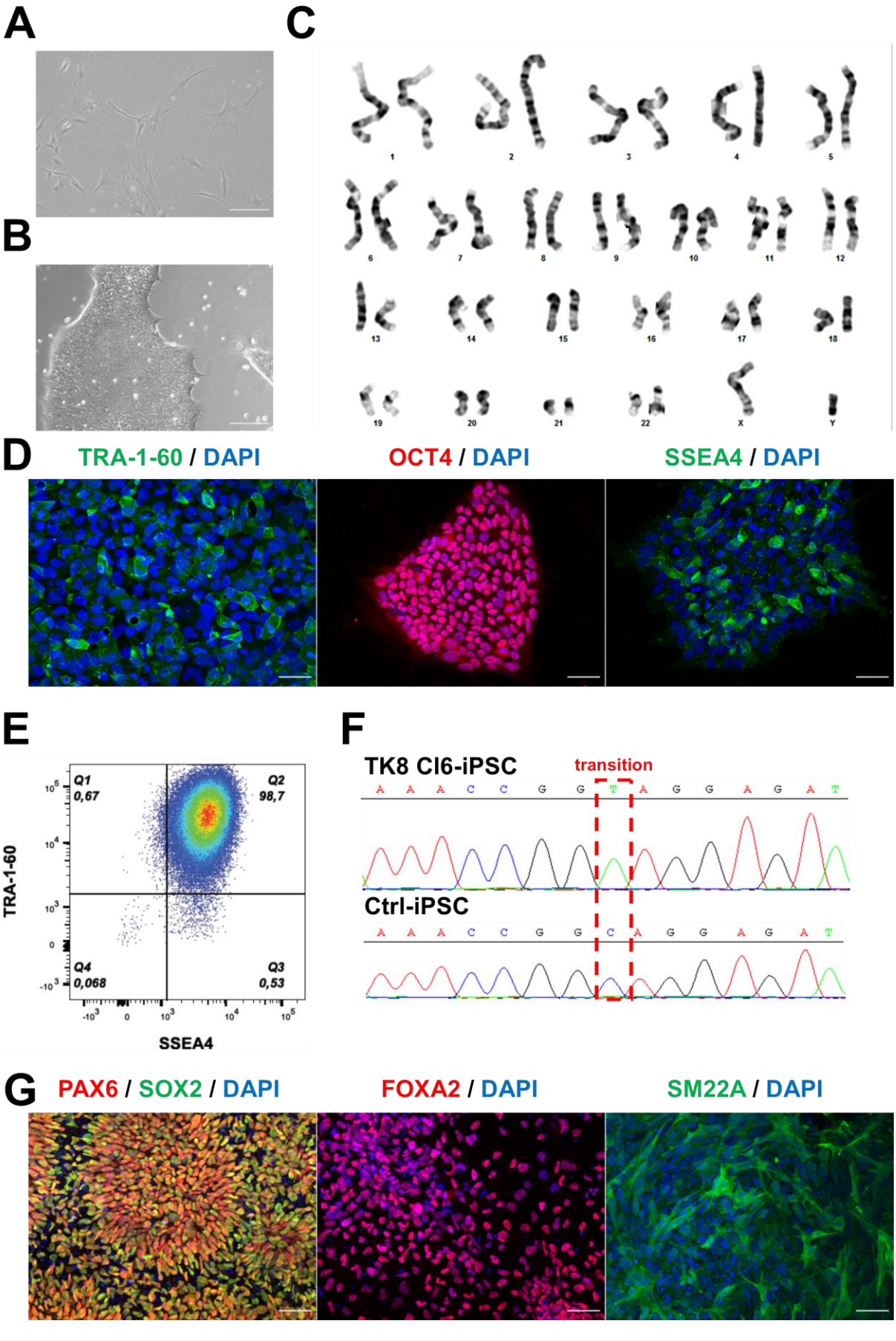
A
B
C
D
TRA-1-60 / DAPI
OCT4 / DAPI
SSEA4 / DAPI
E
Q1
0,67
Q2
98,7
Q4
0,068
Q3
0,53
TRA-1-60
SSEA4
F
TK8 Cl6-iPSC
transition
A A A C C G G T A G G A G A T
Ctrl-iPSC
A A A C C G G C A G G A G A T
G
PAX6 / SOX2 / DAPI
FOXA2 / DAPI
SM22A / DAPI

Figure 8: Characterization of TK8 clone 6. (A) HDF were reprogrammed to (B) iPSC with ESC-like morphology. (C) No chromosomal aberrations were found and (D) robust expression of the pluripotency markers was confirmed. (E) > 98% of live, single cells coexpressed TRA-1-60 and SSEA4, with (F) the retained c.1069C>T mutation. (G) Directed differentiation of cells into all three germ-layers was succesfull. Scale bars: 200 µm (A, B); 50 µm (D, G). Acquired with DMI IL LED (A, B) and Apotome (D, G).

Abbreviations: Ctrl = control; DAPI = 4′,6-diamidino-2-phenylindole; ESC = embryonic stem cell; FOXA2 = forkhead box protein A2; HDF = human dermal fibroblasts; iPSC = induced pluripotent stem cells; OCT4 = octamer-binding transcription factor 4; PAX6 = paired box 6, SM22A = smooth muscle protein 22-alpha; SOX2 = sex determining region Y box 2; SSEA4 = stage specific embryonic antigen 4; TRA-1-60 = tumor resistance antigen 1-60

HDF (**Figure 8 A; Figure 9 A**) were reprogrammed to putative iPSC showing ESC-like morphology (**Figure 8 B; Figure 9 B**), and no numerical or relevant chromosomal abnormalities (**Figure 8 C; Figure 9 C**). The expression of TRA-1-60, OCT4 and SSEA4 was easily detected by ICC (**Figure 8 D; Figure 9 D**). Quantitative analysis of SSEA4 and TRA-1-60 showed a $SSEA4^{+}/TRA\text{-}1\text{-}60^{+}$ cell population of 98.7 %, and 96.9 %, respectively (**Figure 8 E; Figure 9 E**). The disease-associated mutation c.1069C>T for TK8 and c.568delG for TK9 was present in iPSC gDNA (**Figure 8 F; Figure 9 F**). iPSC were differentiated into cells of the ecto-, endo-, and mesoderm as shown by ICC against the germ-layer specific markers PAX6/SOX2 (ectoderm), FOXA2 (endoderm), and SM22A (mesoderm; **Figure 8 G; Figure 9 G**). No mycoplasma was detected (supplementary Figure 31 A)

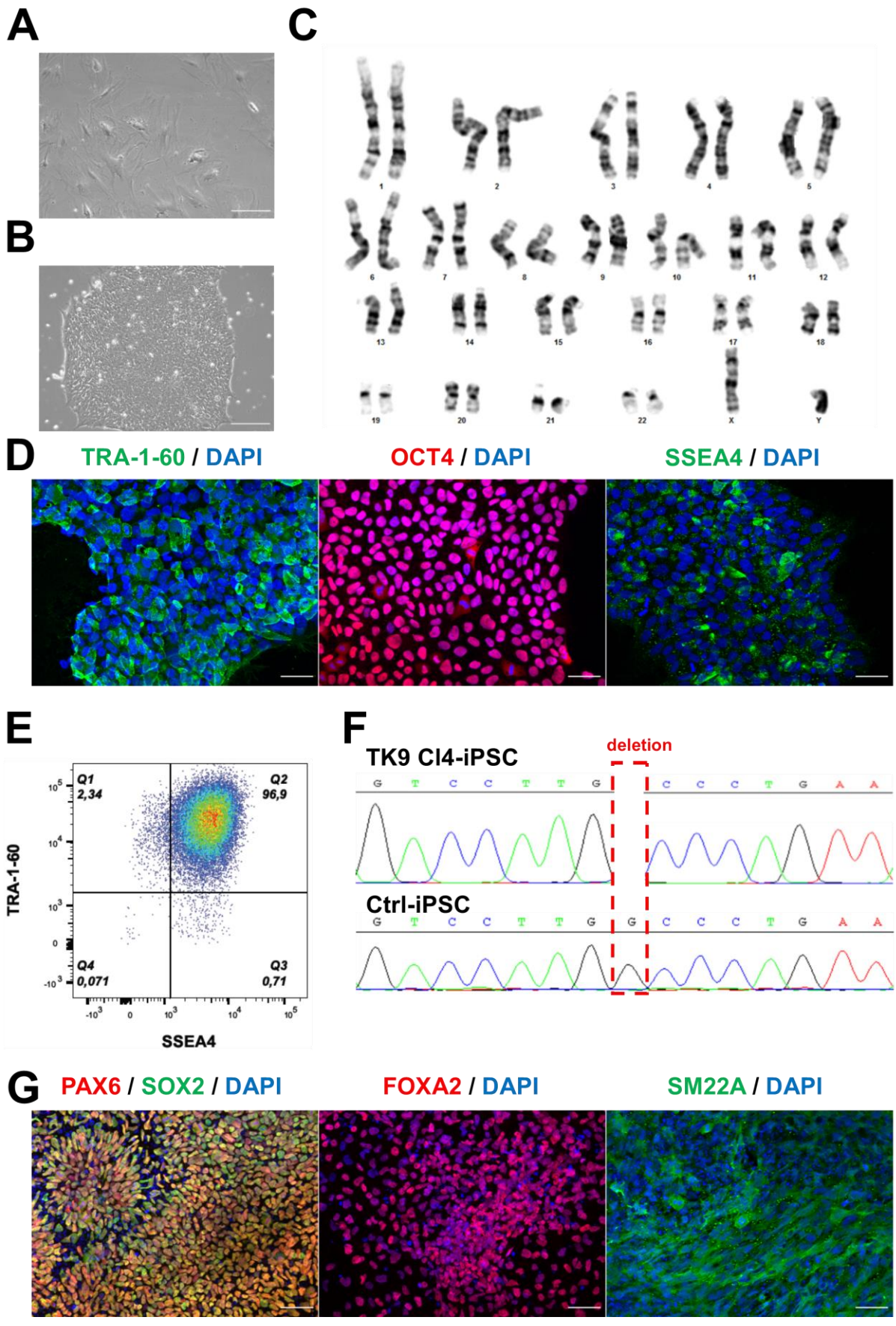

Figure 9: Characterization of TK9 clone 4. Transfection of (A) HDF with YF, resulted in (B), cells, morphological resembling ESC. (C) Chromosomal aberrations were non-existent and (D) expression of

key pluripotency markers was confirmed, with (E) >96% of analyzed cells being TRA-1-60/SSEA double positive. (F) The disease-associated c.568delG mutation was confirmed in iPSC as well as (G) expression of germ-layer markers after directed differentiation. Scale bars: 200 µm (A, B); 50 µm (D, G). Acquired with DMI IL LED (A, B) and Apotome (D, G).

Abbreviations: Ctrl = control; DAPI = 4′,6-diamidino-2-phenylindole; ESC = embryonic stem cell; FOXA2 = forkhead box protein A2; HDF = human dermal fibroblasts; iPSC = induced pluripotent stem cells; OCT4 = octamer-binding transcription factor 4; PAX6 = paired box 6, SM22A = smooth muscle protein 22-alpha; SOX2 = sex determining region Y box 2; SSEA4 = stage specific embryonic antigen 4; TRA-1-60 = tumor resistance antigen 1-60

5.6 Gb3 accumulations in male FD-iPSC lines

Clones from TK8 and TK9 were analyzed for Gb3 depositions using STxB. Data of one clone of each cell line is presented.

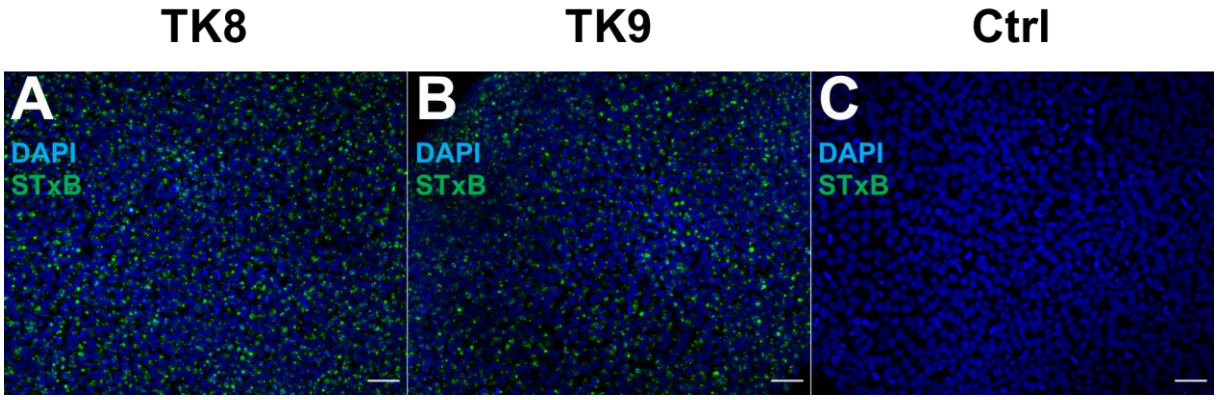

Figure 10: Gb3 accumulations in male FD-iPSC. (A) TK8 and (B) TK9 iPSC showed strong intracellular STxB-signal, whereas (C) no signal was detected in control iPSC. Scale bars: 50 µm. All acquired with Apotome.

Abbreviations: Ctrl = control, DAPI = 4′,6-Diamidin-2-phenylindol; iPSC = induced pluripotent stem cells; STxB = Shiga toxin1, B subunit

Both FD-iPSC lines showed numerous STxB positive accumulations (**Figure 10 A, B**) in contrast to control cells, where no depositions were detected (**Figure 10 C**).

5.7 Sensory neuron differentiation of iPSC

The differentiation protocol was established using the TK1 cell line and applied to the control, TK8, and TK9 cell lines. Data shown in this section is from the control line, if not otherwise stated.

5.7.1 Time course of the differentiation

iPSC were seeded with such a high density that an overconfluent monolayer was formed 2 days after the start of differentiation (**Figure 11 A**). Ten days after neuronal initiation, ganglia-like structures emerged (black arrow) with underlying non-neuronal, highly proliferative cells (white arrow; **Figure 11 B**). Cells were split, neurons regrouped into clusters, from which feeder-layer cells grew out (white arrow; **Figure 11 C**). After 6 weeks of maturation the feeder-layer cell number was greatly reduced with neurons (black arrow) adhering on top of the remaining cells (white arrow; **Figure 11 D**).

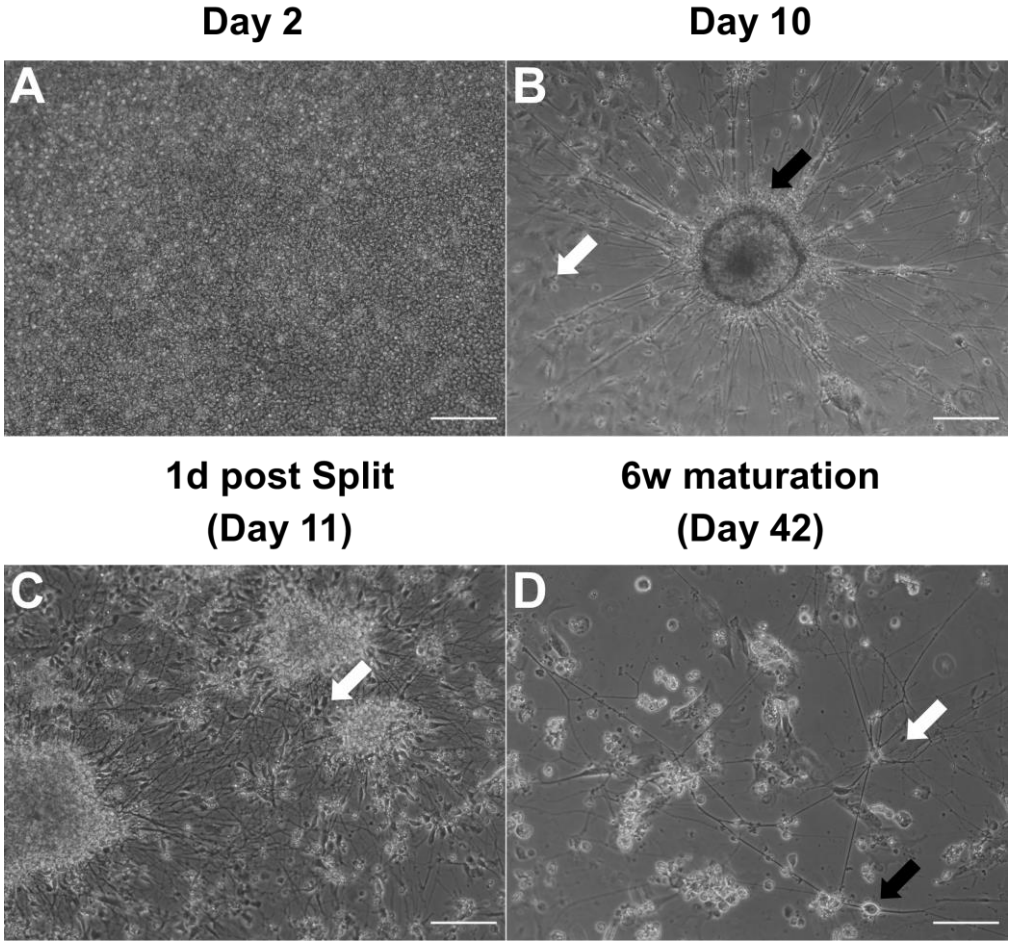

Figure 11: Neuronal differentiation. (A) Overconfluent cells with iPSC morphology on day 2, differentiated into (B) ganglia-like structure with neuronal processes (black arrow) after 10 days of differentiation, together with non-neuronal cells (white arrow). (C) Outgrowth of unspecified proliferative

cells from clusters 1 day after the neuronal split (white arrow). (D) Dying back of feeder layer cells with neurons attaching on top of the remaining cells (white arrow), showing nociceptive morphology (black arrow). Scale bars: 200 µm. All acquired with DMI IL LED.

Abbreviations: iPSC = induced pluripotent stem cells

5.7.2 Assesment of cytostatic compounds

To reduce non-neuronal cells, three different inhibitors were tested: FdU, CultureOne, and Mitomycin C.

Treatment with FdU resulted in a reduction of feeder layer cells, wheras neuronal structures seemed to be unaffected (**Figure 12 A**). The CultureOne treatment resulted in massive cell death of all cell types (**Figure 12 B**). Mytomycin C effectively reduced non-neuronal populations, but seemed to stress neurites (**Figure 12 C**). Images were acquired 1 week after initial treatment.

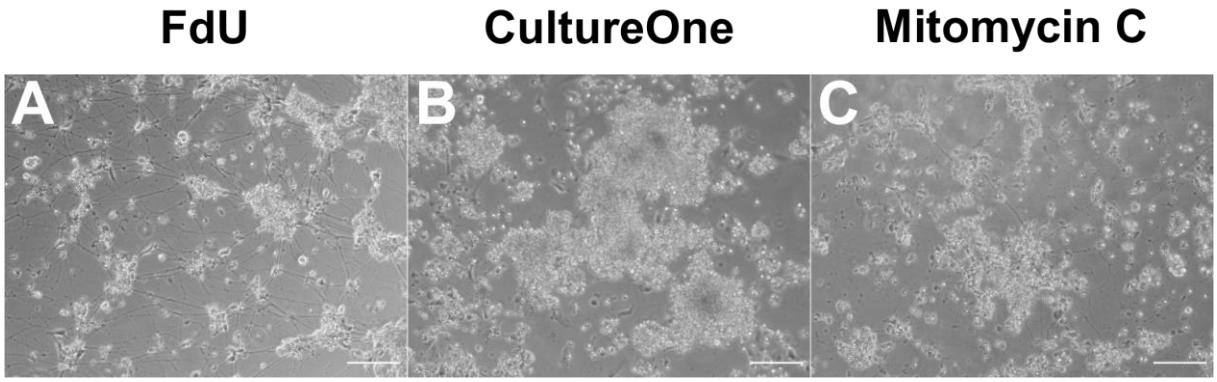

Figure 12: Comparison of cytostatics. (A) No neurotoxicity was caused by FdU, in contrast to (B) massive neuronal death with CultureOne. (C) Mitomycin C killed feeder-layer cells, but had a negative effect on neurons. Scale bars: 200 µm. All acquired with DMI IL LED.

Abbreviations: FdU = floxuridine

5.7.3 Marker expression during differentiation phase

To investigate expression of key markers, cells were fixed and analyzed every 2 days, during the first 10 days of differentiation.

The pluripotency marker OCT4 was highly expressed on day 2 and declined rapidly after 4 days of differentiation until no expression was detectable from day 6 onward. No expression of the sensory marker BRN3A was found during the first 4 days, but was abundant from day 6 on (**Figure 13 A – A’’’’**). PAX6, a key marker for neural crest fate was expressed starting from day 2, seemed to be most plentiful on day 6 and decreased afterwards. SOX10, a marker for neural progenitor and glial cells, had overall low expression starting from day 6, and was slightly increased on day 10

(**Figure 13 B – B’’’’**). The pan-neuronal marker TUJ1 and peripheral neuronal marker PRPH were absent on day 2 and showed increased expression starting from at least day 6. The amount of PRPH^{+} cells increased over time. No data was obtained for this immunoreaction on day 4 and no DAPI counterstaing was done for day 10 (**Figure 13 C – C’’’’**).

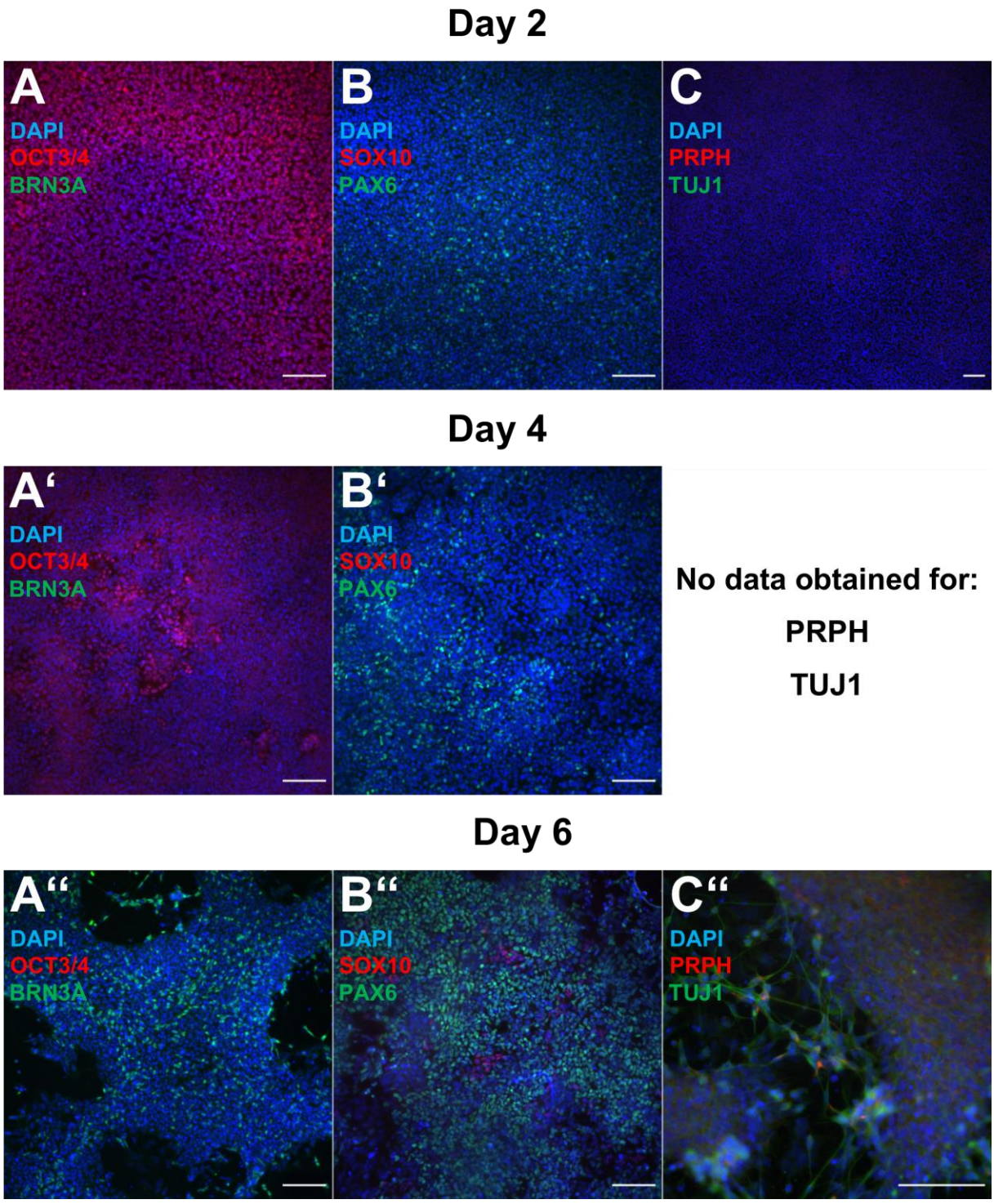

Continued on next page.

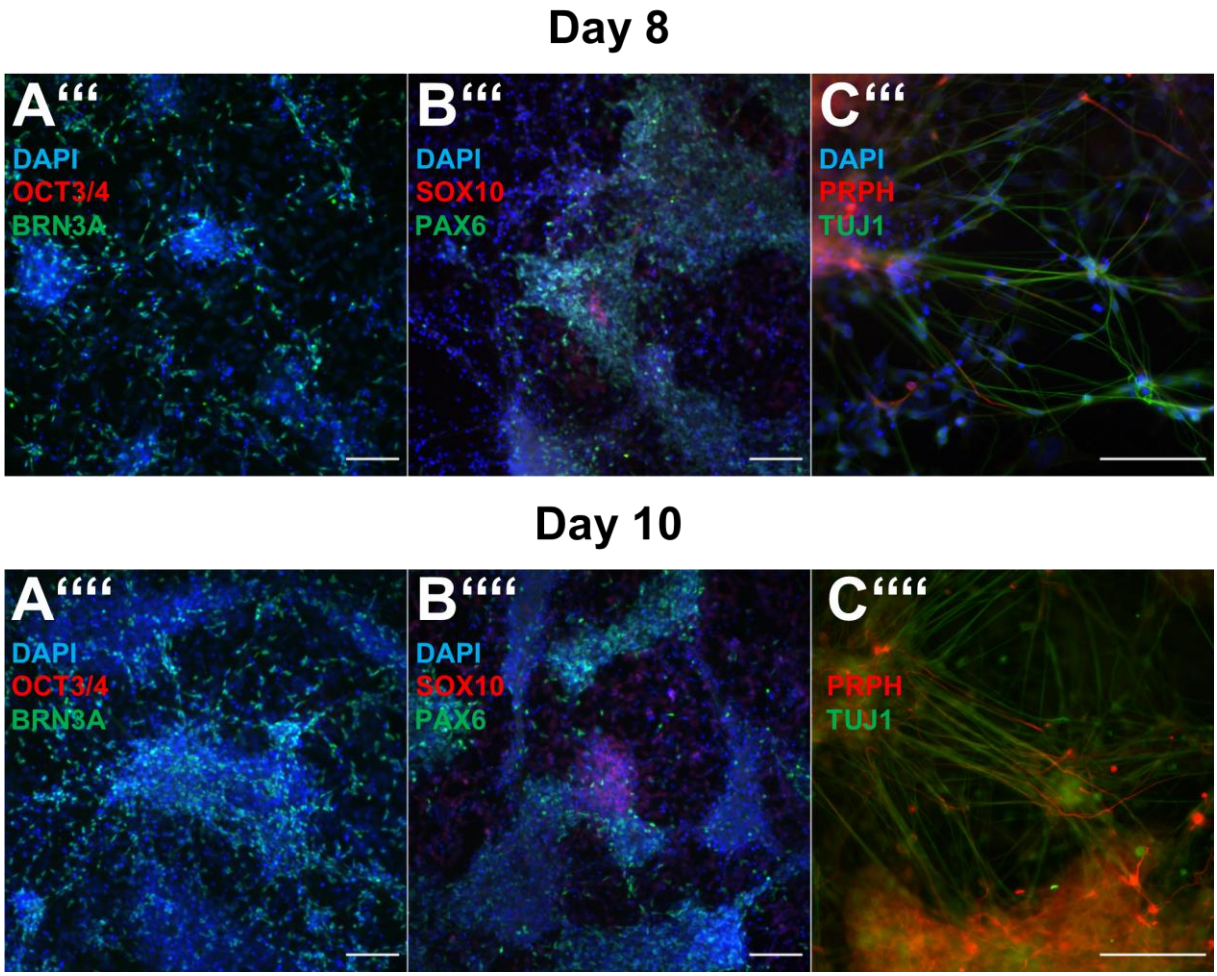

Figure 13: Key marker expression during neuronal differentiation. (A – A’’’’) The expression of OCT4 declined over time, whereas BRN3A expression increased during the differentiation. (B – B’’’’) PAX6 expression started on day 2 and was upregulated during the differentiation. SOX10 was detectable starting from day 6 onwards. (C – C’’’’) TUJ1 and PRPH were absent during the first 6 days, but were highly upregulated from then on. Scale bars: 100 µm. All acquired with Axiophot.

Abbreviations: BRN3A = POU class4 homebox 1; DAPI = 4′,6-diamidino-2-phenylindole; OCT4 = octamer-binding transcription factor 4; PAX6 = paired box 6; PRPH = peripherin; SOX10 = sex determining region Y-box 10; TUJ1 = neuron-specific class III β-tubulin

5.7.4 Marker expression on mature neurons - ICC

Expression of key markers for the sensory fate of neurons was determined during estblishment of the differentiation protocol on the control-iPSC line.

Mature control neurons expressed the pan-neuronal marker TUJ1 and the peripheral neuronal marker PRPH (**Figure 14 A**). Voltage gated sodium channel 1.8 ($Na_v1.8$) was highly expressed on neurons (**Figure 14 B**), whereas transient-receptor potential cation channel subfamily V member 1 (TRPV1) showed low expression, in some cases even unconclusive (**Figure 14 C**). Substance P (SP) was detected in some

fibers (white arrows), but also resulted in a high background signal (yellow arrow; **Figure 13 D**).

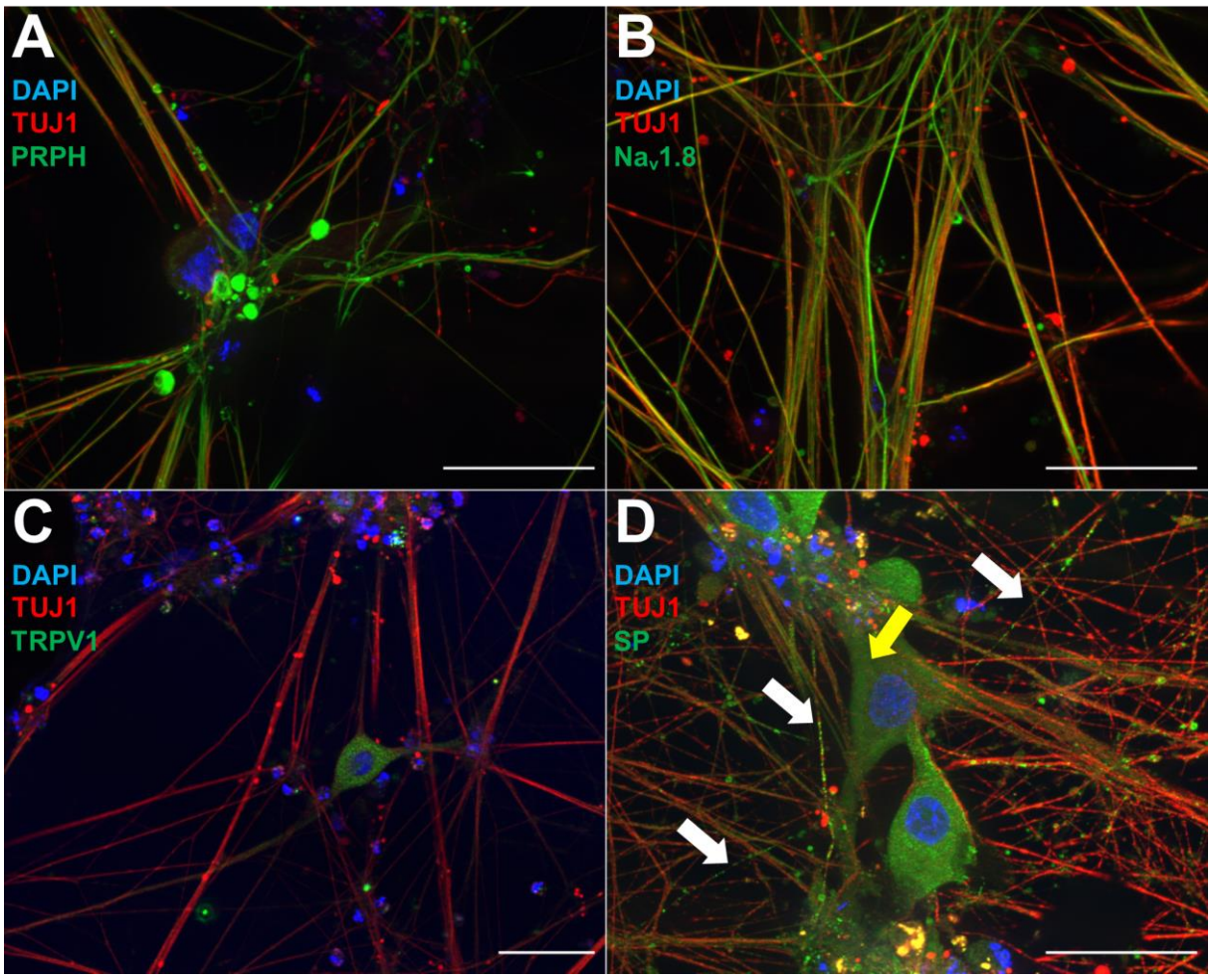

Figure 14: Key sensory marker expression. Expression of (A) PRPH, (B) Na_v 1.8, (C) TRPV1, and (D) SP together with TUJ1. Scale bars: 50 µm. Acquired with Apotome.

Abbreviations: DAPI = 4′,6-diamidino-2-phenylindole; Na_v 1.8 = sodium voltage-gated channel alpha subunit 10; PRPH = peripherin; SP = substance P; TRPV1 = transient receptor potential cation channel subfamily V member 1; TUJ1 = neuron-specific class III β-tubulin

5.7.5 TRPV1 labeling using dkTx

A secondary labeling technique using DkTx (see **section 4.3.1**) was used to detect TRPV1 in mature control neurons.

DkTx$^+$ neurons were sparse in the PRPH$^+$ popluation, with a substantial amount of non-cellular DkTx$^+$ profiles present in the sample (blue arrows; **Figure 15 A**). A more detailed analysis revealed DkTx$^-$ (white arrow) and DkTx$^+$ neurites (yellow arrow) likely in the same fiber bundle (**Figure 15 B – D**).

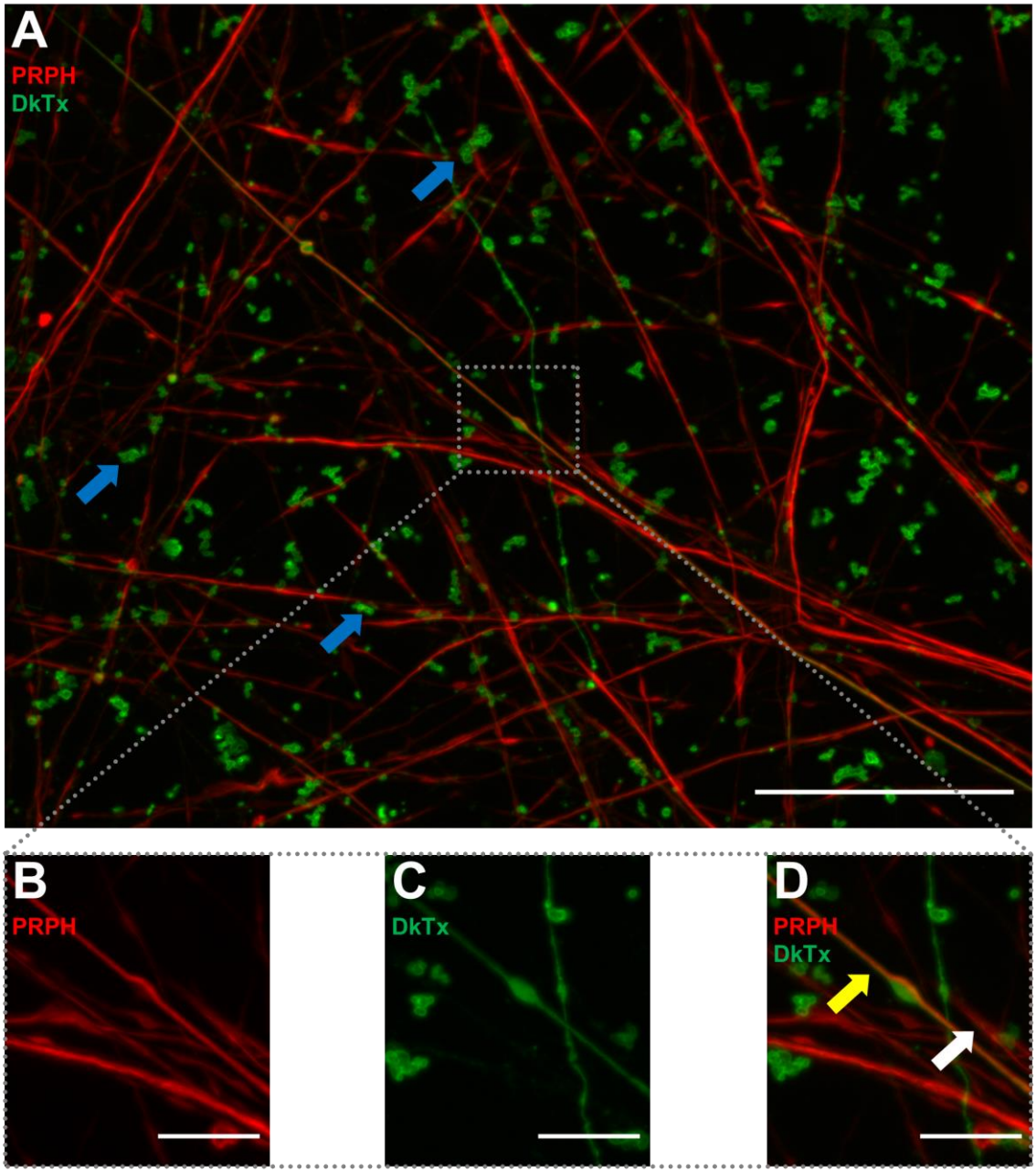

Figure 15: Labeling of TRPV1. (A) Overview of PRPH and DkTx labeling with some doublepositive fibers and DkTx aggregates (blue arrows). Photomicrograph-excerpts from the single acquisition channels for (B) PRPH and (C) DkTx. (D) Two-channel pictures with marked DkTx$^+$ fiber (yellow arrow)

and DkTx^{-} fiber (white arrow). Scale bars: 50 µm (A); 10 µm (B – D).All acquired with Apotome as maximum intensity Z-projections.

Abbreviations: DkTx = double-knot toxin; PRPH = peripherin

5.7.6 Marker expression of mature neurons – qRT-PCR

Expression of a small panel of key markers was investigated using qRT-PCR. In this section, data of one clone of each patient is presented; data of the second clone is shown in the supplementary (see **section 8.9**). Gene expression is normalized to iPSC expression (see **section 4.13**). A characterized control cell line was analyzed in parallel, but is lacking data for PRPH, due to insufficient amount of RNA.

Mature neurons, derived from TK8 Cl6 iPSC expressed TUJ1, PRPH, Na_v 1.7, and TRPV1 (**Figure 16 A**). The same markers were upregulated in TK9 Cl1 neurons, compared to iPSC baseline expression (**Figure 16 B**).

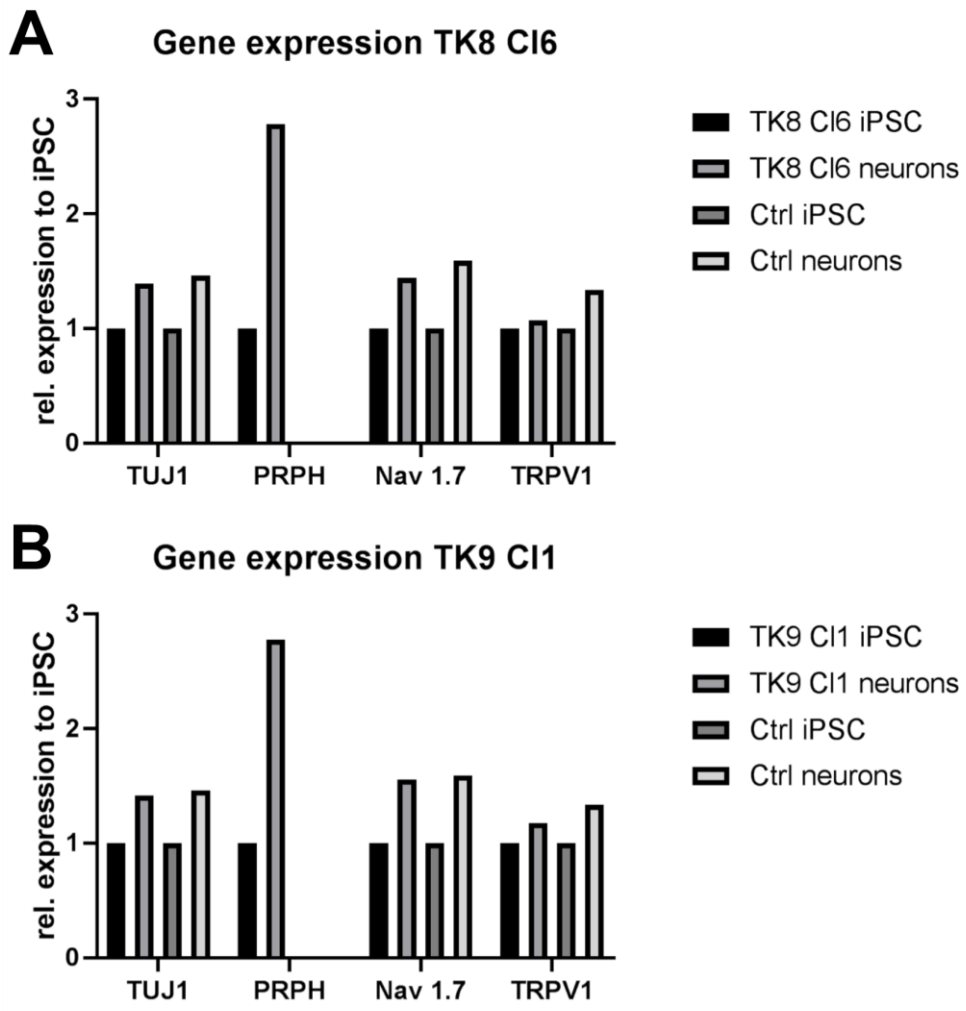

Figure 16: Gene expression of mature neurons. Neurons from (A) TK8 clone 6 and (B) TK9 clone 1 expressed TUJ1, PRPH, Nav 1.7 and TRPV1.

Abbreviations: Cl = clone; Ctrl = control; iPSC = induced pluripotent stem cells; Na_v 1.7 = sodium voltage-gated channel alpha subunit 9; PRPH = peripherin; TRPV1 = transient receptor potential cation channel subfamily V member 1; TUJ1 = neuron-specific class III β-tubulin

5.8 Neuronal Gb3 accumulations

Mature neurons were analyzed for Gb3 depositions, together with the the lysosomal-associated membrane protein 1 (LAMP1).

Gb3 accumulations colocalizing with LAMP1 were found in a perinuclear way, and to a certain extent in neurites in neurons derived from TK8-iPSC (**Figure 17 A**) and TK9-iPSC (**Figure 17 B**). No obvious difference in Gb3 load or lysosomal density was observed. Control cells showed no accumulations at all with a comparable lysosomal density as TK8 and TK9 (**Figure 17 C**). Deeper investigation of $LAMP1^+$ structures (**Figure 17 A' – C'**) and Gb3 depositions (**Figure 17 A'' – C''**) revealed lysosomal localization (white arrows) of Gb3 in TK8 (**Figure 17 A'''**), TK9 (**Figure 17 B'''**), but not in control cells (**Figure 17 C'''**).

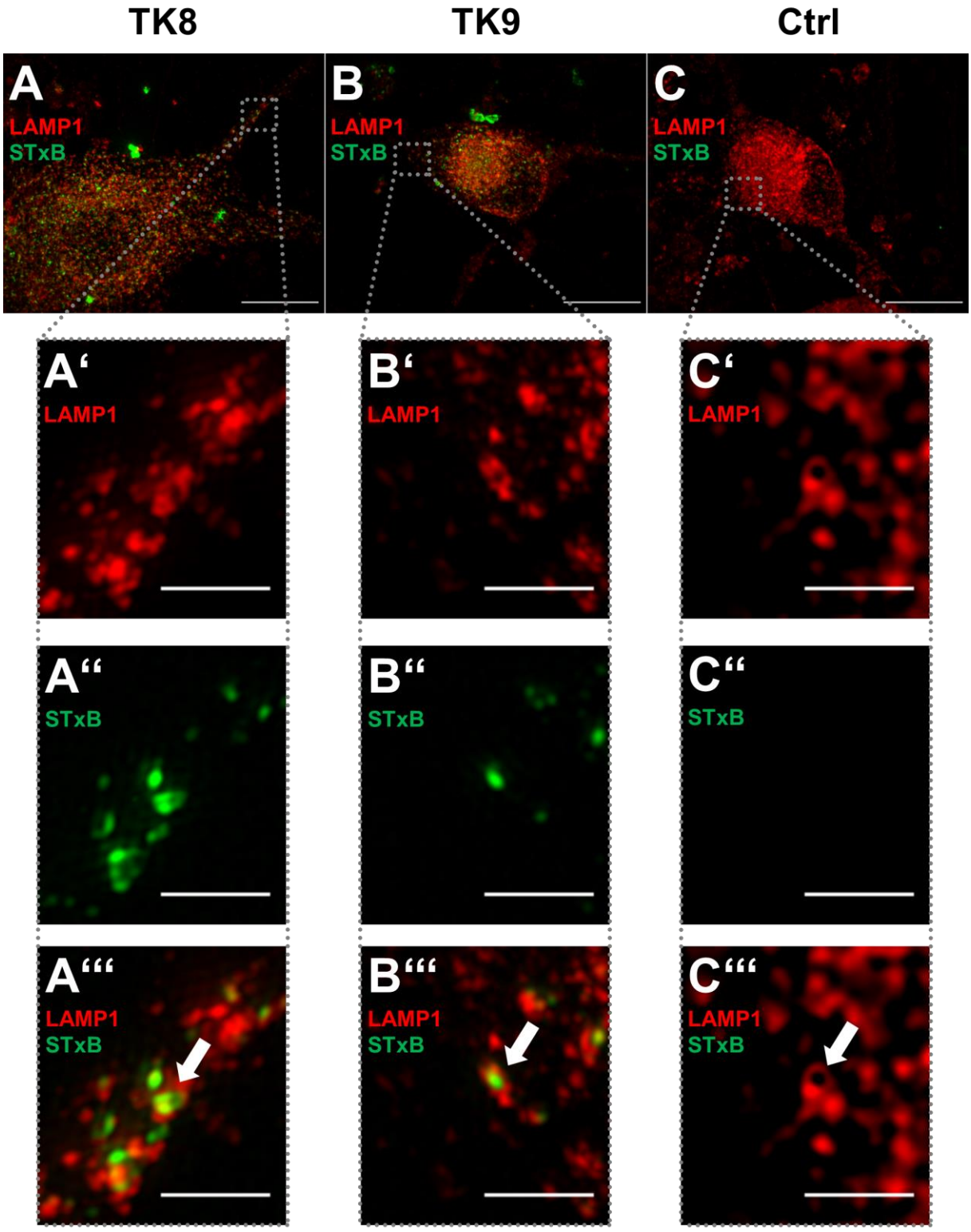

Figure 17: Gb3 accumulations in iPSC-derived neurons. Numerous Gb3 depositions colocalizing with LAMP1⁺ profiles were detected in (A) TK8 and (B) TK9 neurons. (C) The control population showed no accumulations at all, but a normal LAMP1 immunoreaction. Enlarged single channel acquisition images of LAMP1 (A', B', C'), STxB (A'', B'', C'') showing Gb3 localization inside of lysosomes (white arrows) in TK8 (A'''), TK9 (B'''), but not in (C''') control cells. Scale bars: 15 µm (A - C); 2 µm (A' – C'''). All acquired with SIM, with maximum intensity Z-projections (A – C) and single focal planes (A' – C''').

Abbreviations: Ctrl = control; DAPI = 4′,6-diamidino-2-phenylindole; iPSC = induced pluripotent stem cells; LAMP1 = lysosomal-associated membrane protein 1

5.9 Effect of ERT on Gb3 depositions

To analyze the effect of agalsidase-β on neuronal Gb3 accumulations, 1 week old (young; **Figure 18**) and > 6 weeks old neurons (mature; **Figure 19**) were incubated and analyzed for Gb3 load (see **section 4.12.3**). The amount of analyzed neurons is listed in **Table 3**. No Gb3 accumulations at all were detected in control cells with or without treatment and thus omitted from analysis (n=150, data not shown).

Table 3: Amount of analyzed neurons.

Accumulation subgroup	**Cell line**			
	TK8		TK9	
	no ERT	+ ERT	no ERT	+ ERT
	Young neurons (1 week old; N)			
TUJ1^{+} cells	450	450	600	600
Total Gb3 load	104	132	250	204
Scattered Gb3 load	25	0	88	9
Focal Gb3 load	127	132	247	195
Mixed Gb3 load	4	0	15	0
	Mature neurons (> 6 weeks old; N)			
TUJ1^{+} cells	1207	1286	341	326
Total Gb3 load	913	490	283	171
Scattered Gb3 load	808	329	272	149
Focal Gb3 load	76	156	4	22
Mixed Gb3 load	29	5	7	0

Abbreviations: ERT = enzyme replacement therapy; Gb3 = globotriaosylceramide; N = number; TUJ1 = neuron-specific class III β-tubulin

In young neurons from TK8 and TK9, ERT had no effect on the total Gb3 load (**Figure 18 A**), whereas scattered depositions were reduced in treated TK9 neurons compared to untreated ($p<0.05$, **Figure 18 B**). Focal Gb3 depositions were not cleared by ERT in TK8 cells, but increased in treated TK9 neurons compared to neurons lacking ERT ($p<0.05$, **Figure 18 C**). Mixed Gb3 depositions were decreased only in TK9 with treatment compared to untreated cells ($p<0.05$, **Figure 18 D**).

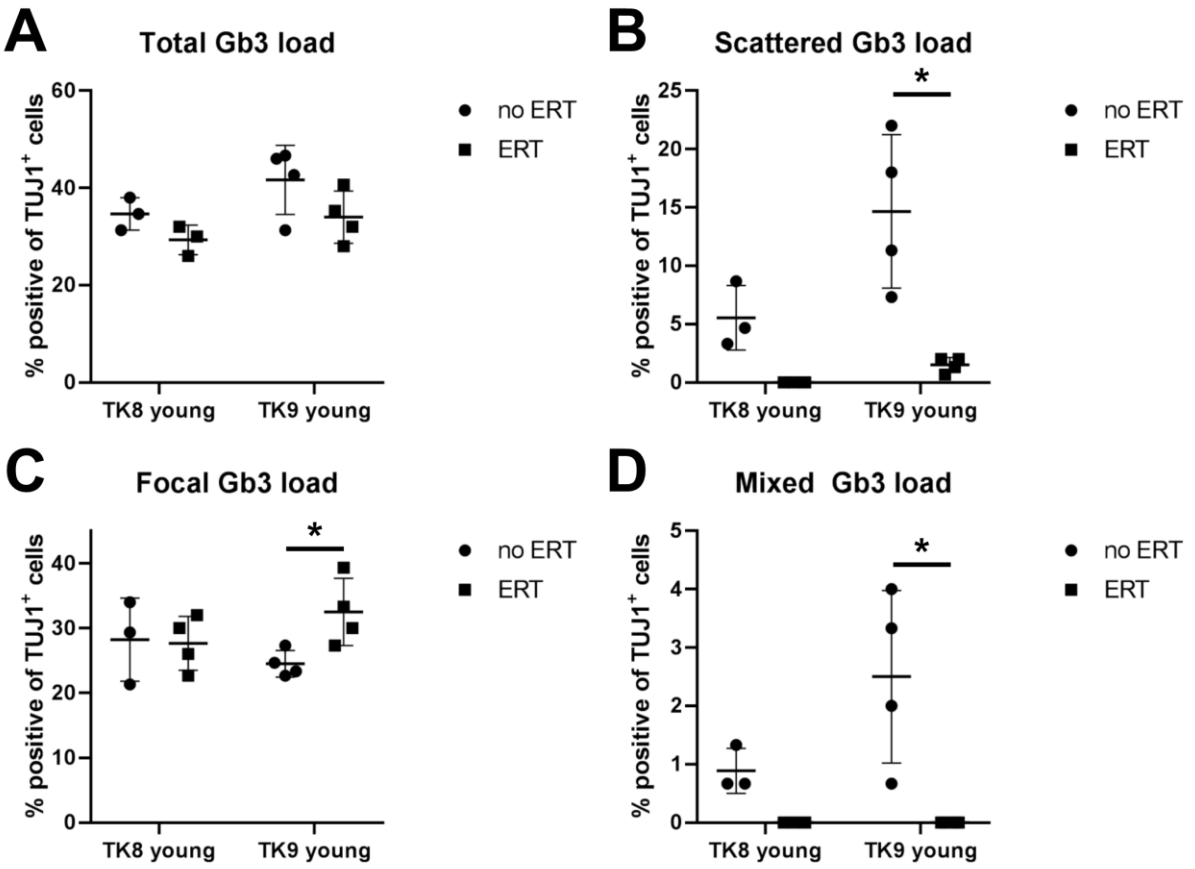

Figure 18: Effect of ERT on young neurons. (A) Total Gb3 load was not reduced in young neurons after treatment in both lines. (B) Scattered Gb3 accumulations were decreased in TK9 young neurons after ERT, but not in TK8 ($p<0.05$). (C) Focal Gb3 depositions were increased in young neurons with ERT, but not changed in TK8 ($p<0.05$). (D) Mixed Gb3 loads were reduced in TK9, but not in TK8 ($p<0.05$).

For number of evaluated neurons see **Table 3**.

Abbreviations: ERT = enzyme replacement therapy; Gb3 = globotriaosylceramide; TUJ1 = neuron-specific class III β-tubulin

Total Gb3 load was decreased in treated neurons derived from TK8-iPSC ($p<0.001$), with TK9 neurons showing a trend towards reduction compared to untreated cells ($p=0.071$; **Figure 19 A**). The same was true for scattered Gb3 depositions, the most common form of accumulations (**Figure 19 B**). No effect of ERT was found on focal Gb3 depositions (**Figure 19 C**), but a decrease was detected in cells with a mixed Gb3 load for TK8 compared to untreated neurons ($p<0.05$; **Figure 19 D**).

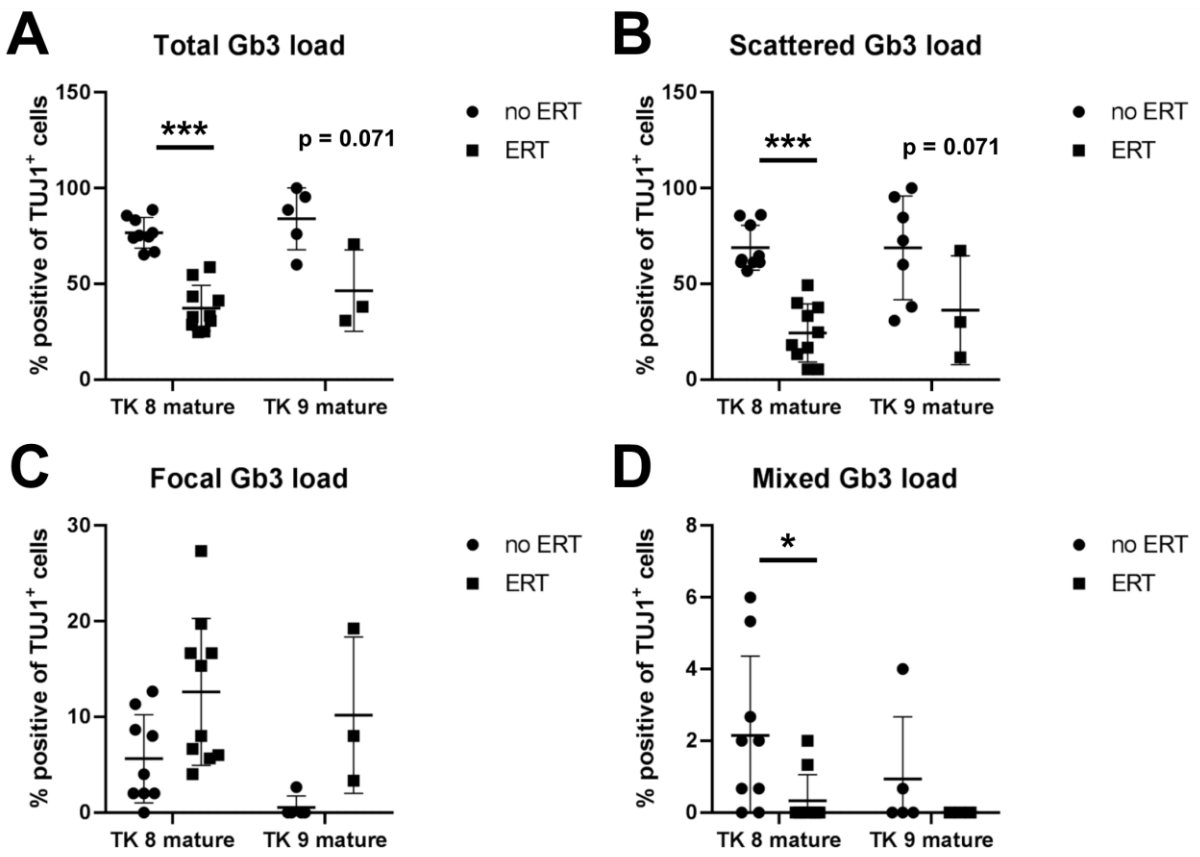

Figure 19: Effect of ERT on mature neurons. (A) Total Gb3 load was reduced in TK8 neurons after ERT ($p<0.001$). Gb3 depositions in TK9 neurons showed a trend of reudction after treatment ($p=0.071$). (B) Scattered accumulations were reduced in TK8 ($p<0.001$), not in TK9 ($p =0.071$), similar to (A). (C) No effect on focal Gb3 accumulations was found in TK8 and TK9 neurons. (D) Mixed Gb3 deposistion were reduced after treatment in TK8 ($p < 0.05$), but not in TK9 neurons.

For number of evaluated neurons see **Table 3**.

Abbreviations: ERT = enzyme replacement therapy; Gb3 = globotriaosylceramide; TUJ1 = neuron-specific class III β-tubulin

Young and mature neurons were compared with each other to analyze time-dependent build-up of Gb3 accumulations (**Figure 20, Figure 21**).

In untreated TK8 neurons, total Gb3 load was higher in mature neurons without ERT, but not with ERT ($p<0.01$; **Figure 20 A**). More cells with scattered Gb3 accumulations were found with or without treatment in mature neurons ($p<0.01$; **Figure 20 B**), whereas young neurons had more focal Gb3 depositions, independent of treatment ($p<0.01$, $p<0.05$; **Figure 20 C**). Cells with mixed Gb3 accumulation were sparse and showed no time-dependent difference (**Figure 20 C**).

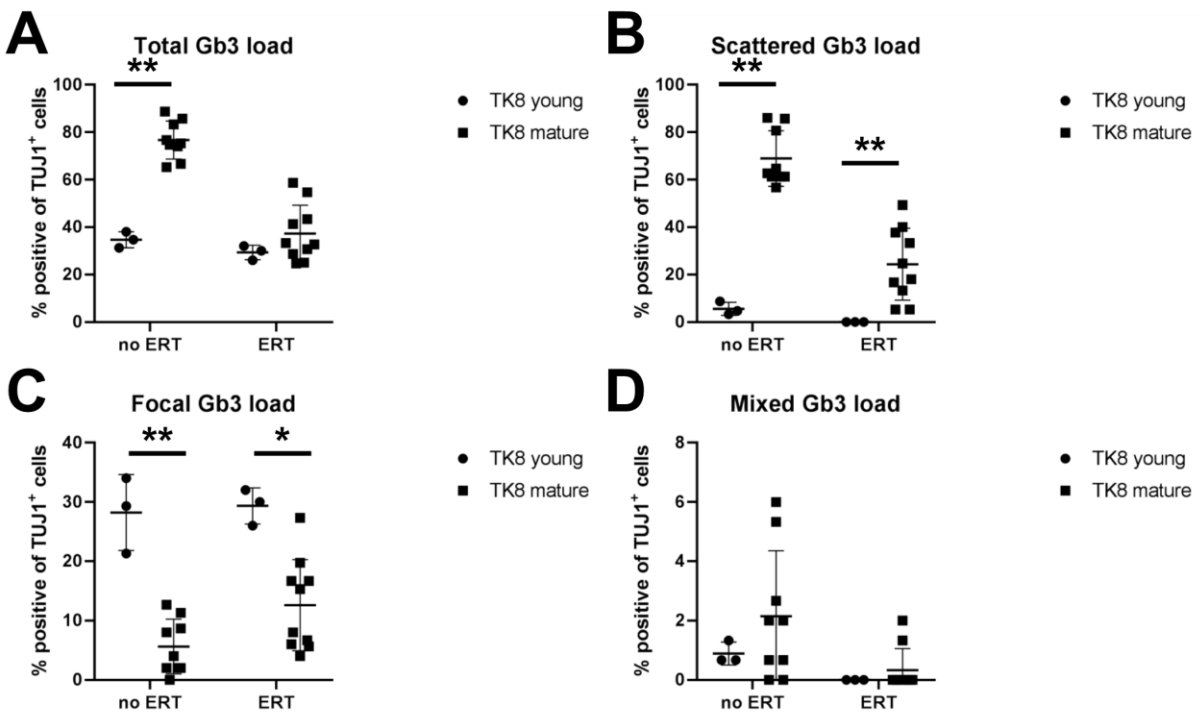

Figure 20: Time dependent accumulation of Gb3 in TK8 neurons. (A) Total Gb3 load was increased in mature neurons without ERT ($p<0.01$), no difference was detected after ERT. (B) Scattered depositions were increased with, and without treatment ($p<0.01$). (C) Focal Gb3 was increased in young neurons, independent of treatment ($p<0.01$, $p<0.05$). (D) No differences were detected in cells with mixed Gb3 load.

For number of evaluated neurons see **Table 3**.

Abbreviations: ERT = enzyme replacement therapy; Gb3 = globotriaosylceramide; TUJ1 = neuron-specific class III β-tubulin

Similar to TK8 neurons, mature TK9 neurons had a higher total Gb3 load without treatment than young neurons ($p<0.05$, **Figure 21 A**). Scattered accumulations were more prominent in older neurons without ERT and a trend in the same direction was found in cells with ERT ($p<0.05$, $p=0.057$; **Figure 21 B**). Focal Gb3 load was more abundant in young neurons without treatment than in treated neurons ($p<0.05$, $p=0.057$; **Figure 21 C**). As in TK8 neurons, cells with mixed Gb3 depositions were rare with no age-differences (**Figure 21 D**).

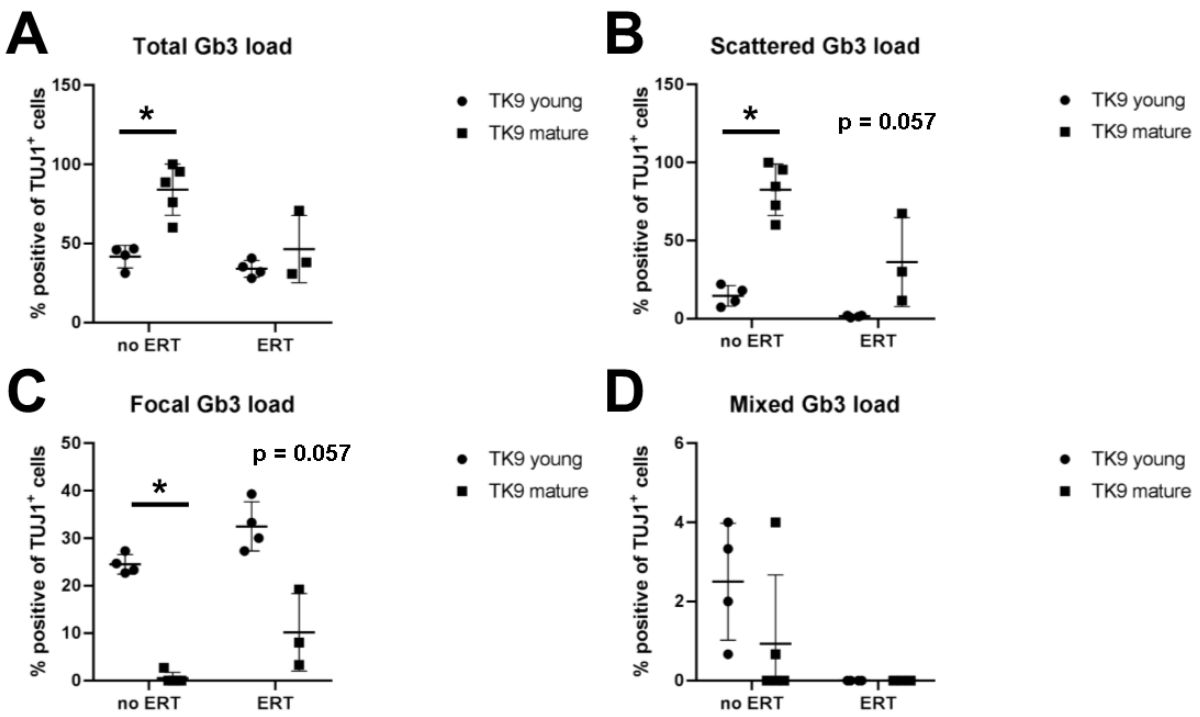

Figure 21: Time dependent accumulation of Gb3 in TK9 neurons. (A) Total Gb3 load was increased in mature neurons without treatment ($p<0.05$). (B) Scattered depositions were also increased in old neurons without ERT ($p<0.05$). (C) Focal Gb3 accumulations were increased in young neurons without treatment ($p<0.05$). (D) No changes were detected in cells with a mixed Gb3 load.

For number of evaluated neurons see **Table 3**.

Abbreviations: ERT = enzyme replacement therapy; Gb3 = globotriaosylceramide; TUJ1 = neuron-specific class III β-tubulin

5.10 Effect of TNF on neuronal Gb3 accumulations

As a pilot experiment, mature neurons from TK8 Cl6 were incubated with TNF or trehalose as control and Gb3 load was assessed to model inflammation as a typical pain trigger in FD patients (Üçeyler et al., 2019). Gb3 load did not change after incubation with TNF compared to trehalose treatment (**Figure 22**).

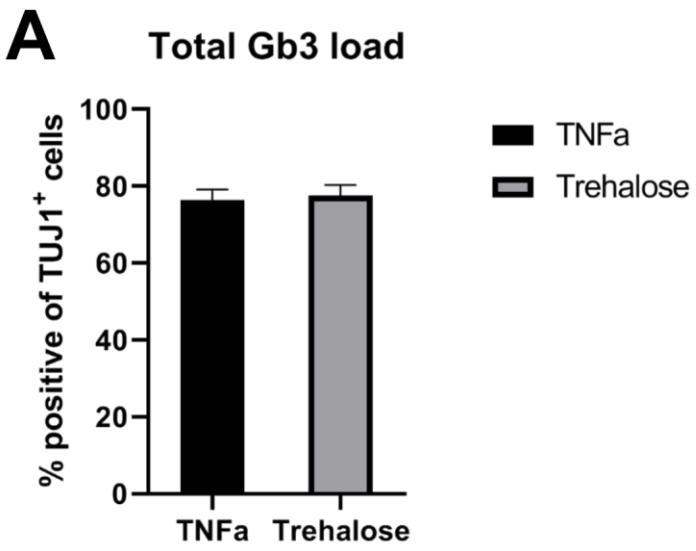

Figure 22: Effect of TNF on Gb3 depositions. No difference of Gb3 load was detectable when treating neuons with TNF and trehalose.

Abbreviations: Gb3 = globotriaosylceramide; TNF = tumor necrosis factor-α; TUJ1 = neuron-specific class III β-tubulin

5.11 Confocal Ca^{2+} imaging

Mature neurons from TK8 (**Figure 23**), TK9 (**Figure 24**), and the control (**Figure 25**) were analyzed at physiological conditions (37°C, 5% CO_2 [v/v]) using confocal Ca^{2+} imaging for detection of intracellular calcium reponses.

Loading of neurons with Fluo-8 AM dye was successful (**Figure 23 A; Figure 24 A; Figure 25 A**). Repetitive temporal changes of the fluorescence intensity of single neurites (white arrows), were detected, cycling from high (**Figure 23 A'; Figure 24 A'; Figure 25 A'**), over low (**Figure 23 A''; Figure 24 A''; Figure 25 A''**), to high again (**Figure 23 A'''; Figure 24 A'''; Figure 25 A'''**). Analysis with NA^3 software confirmed repeated spiking of the mean intensity values, indicating neuronal activity (**Figure 23 B; Figure 24 B; Figure 25 B**).

No comparative analysis between cell lines was performed (see **section 6.6**).

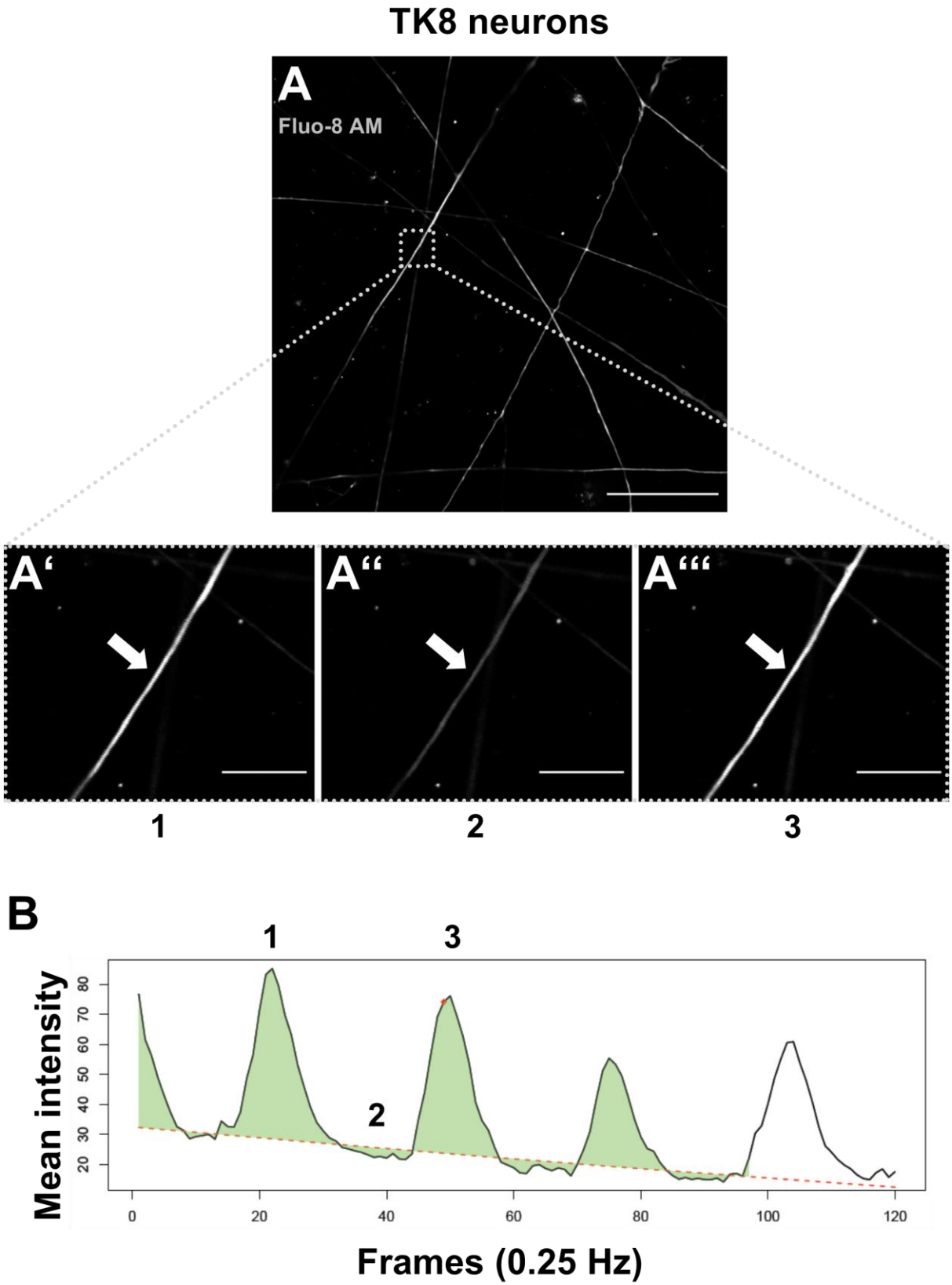

Figure 23: Ca^{2+} imaging of TK8 neurons. (A) Confocal overview image of Fluo-8 AM loaded neurons. (A’ – A”’) Cropped images of a single neurite (white arrow) at different timepoints (1-3). (B) Corresponding mean fluorescence intensity readouts of the region of interest showing repetitive cycling. Scale bars: 50 µm (A); 15 µm (A’ – A”’). All acquired with CLSM.

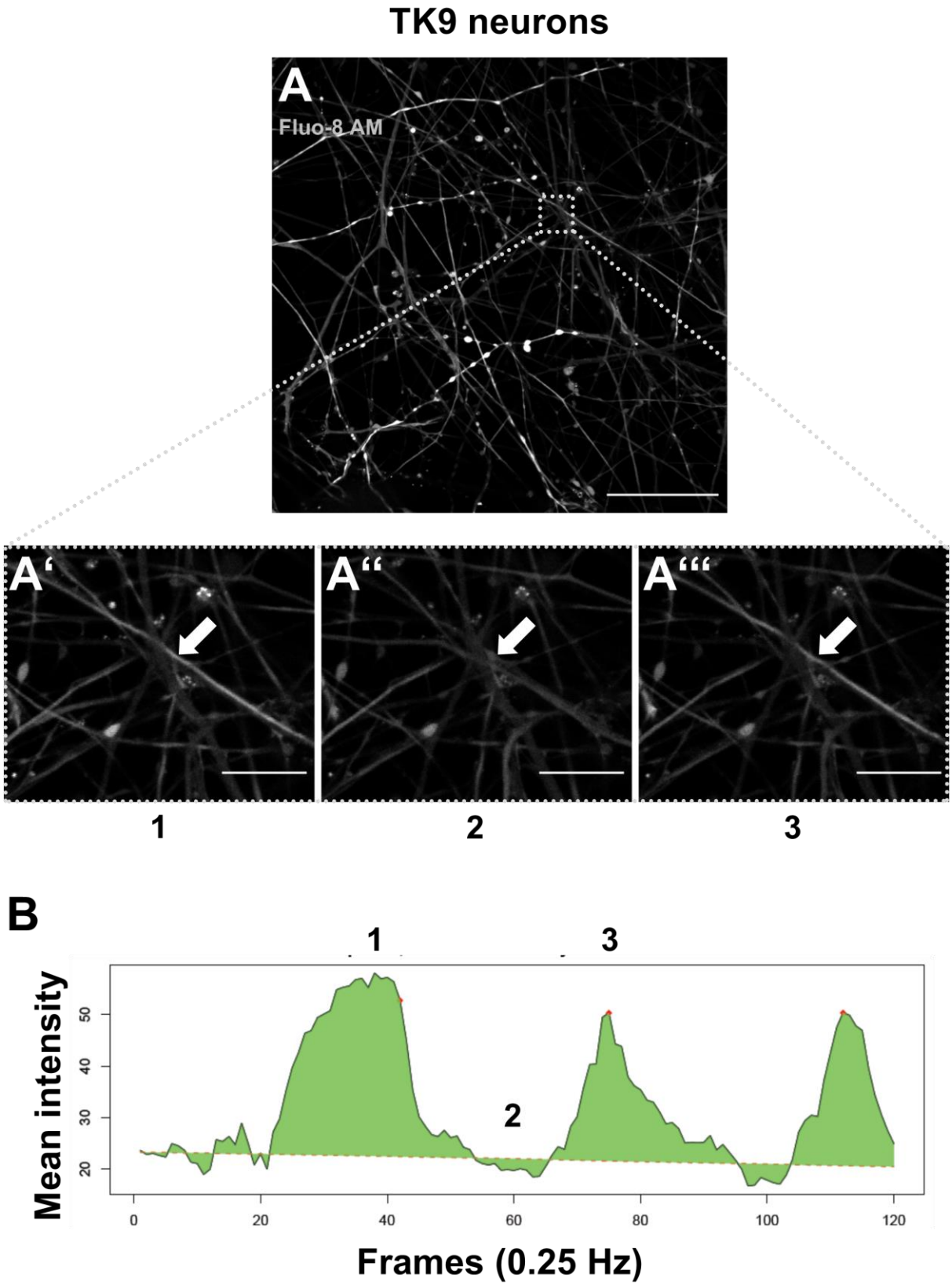

Figure 24: Ca^{2+} imaging of TK9 neurons. (A) Confocal overview image of Fluo-8 AM loaded neurons. (A' – A"') Cropped images of a single neurite (white arrow) at different timepoints (1-3). (B) Corresponding mean fluorescence intensity readouts of the region of interest showing repetitive cycling. Scale bars: 50 µm (A); 15 µm (A' – A"'). All acquired with CLSM.

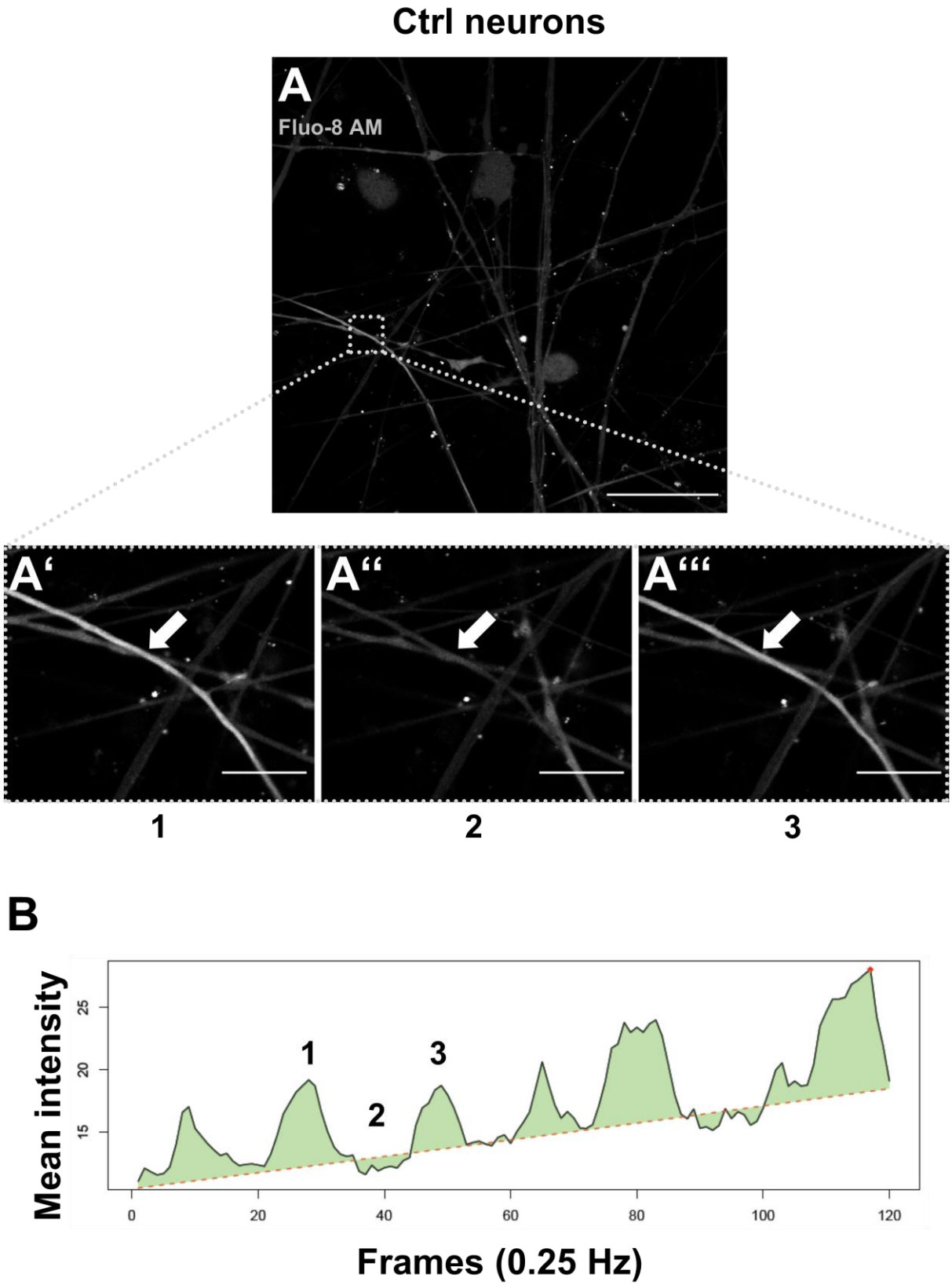

Figure 25: Ca^{2+} imaging of Ctrl neurons. (A) Confocal overview image of Fluo-8 AM loaded neurons. (A’ – A’’’) Cropped images of a single neurite (white arrow) at different timepoints (1-3). (B) Corresponding mean fluorescence intensity readouts of the region of interest showing repetitive cycling. Scale bars: 50 µm (A); 15 µm (A’ – A’’’). All acquired with CLSM.

5.12 Patch clamp analysis of mature neurons

Neurons from all cell lines initiated AP after stimulation (**Figure 26 A, B, C**). We measured resting membrane potential, the threshold to elicit an AP and calculated the difference ($V_{ThresholdDiff}$) as a marker for neuronal excitability (**Figure 26 D**). Neurons from TK8 had a lower $V_{ThresholdDiff}$ compared to control ($p<0.05$) or TK9 neurons ($p<0.001$; **Figure 26 E**).

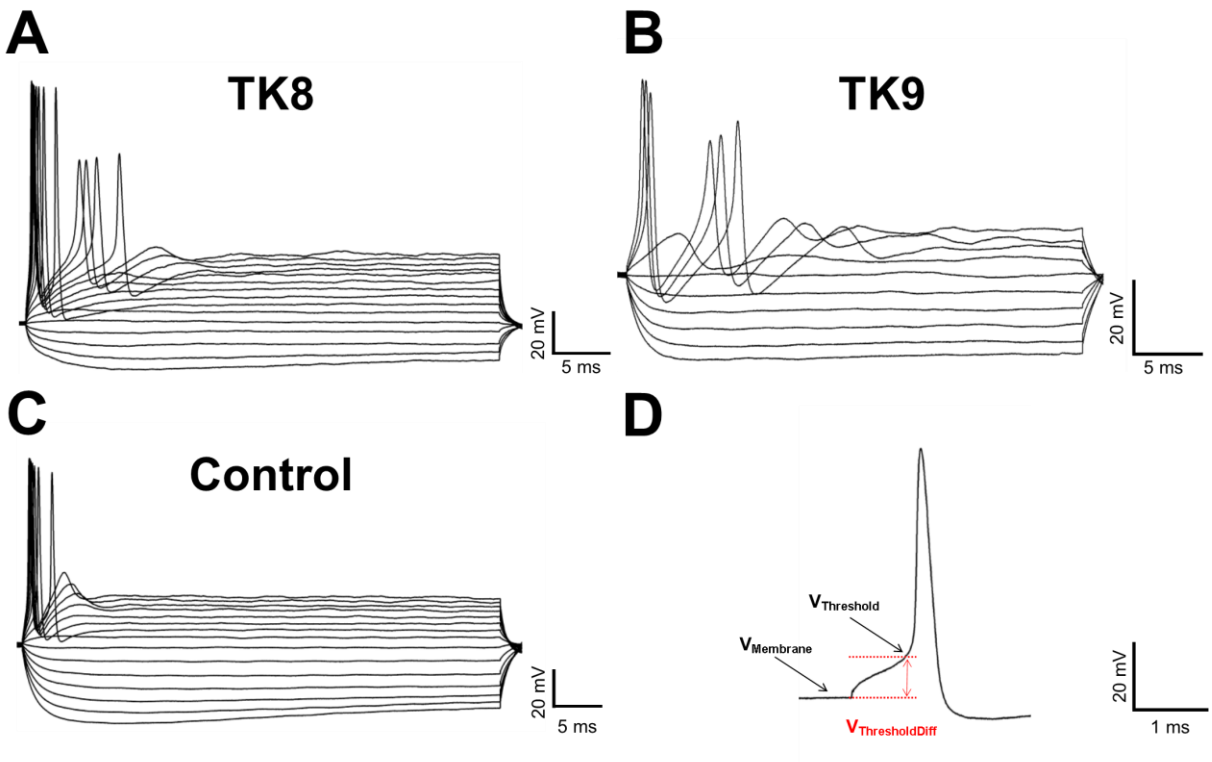

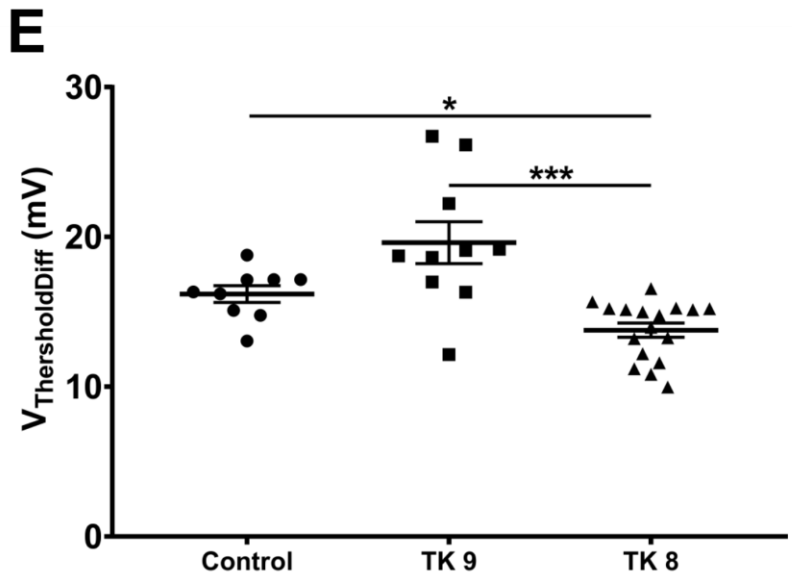

Figure 26: Patch clamp analysis of control, TK8, and TK9. Examplified AP trains for (A) TK8, (B) TK9, and (C) control neurons. (D) Definition of the $V_{ThresholdDiff}$, shown on an AP. (E) TK8 had lower $V_{ThresholdDiff}$, compared to TK9 ($p<0.001$) and control neurons ($p<0.05$).

Abbreviations: AP = action potential; Data acquisition and analysis performed by Dr. Lukas Hofmann

5.13 *d*STORM: Proof-of-Principle

As a Proof-of-Principle experiment, control neurons were labelled with CTxB and analyzed using the *d*STORM setup. The super-resolution image reveals many details of the membrane, with virutally no background signal **(Figure 27 A, A'**), whereas these details are lost using conventional widefield microscopy (**Figure 27 B, B'**)

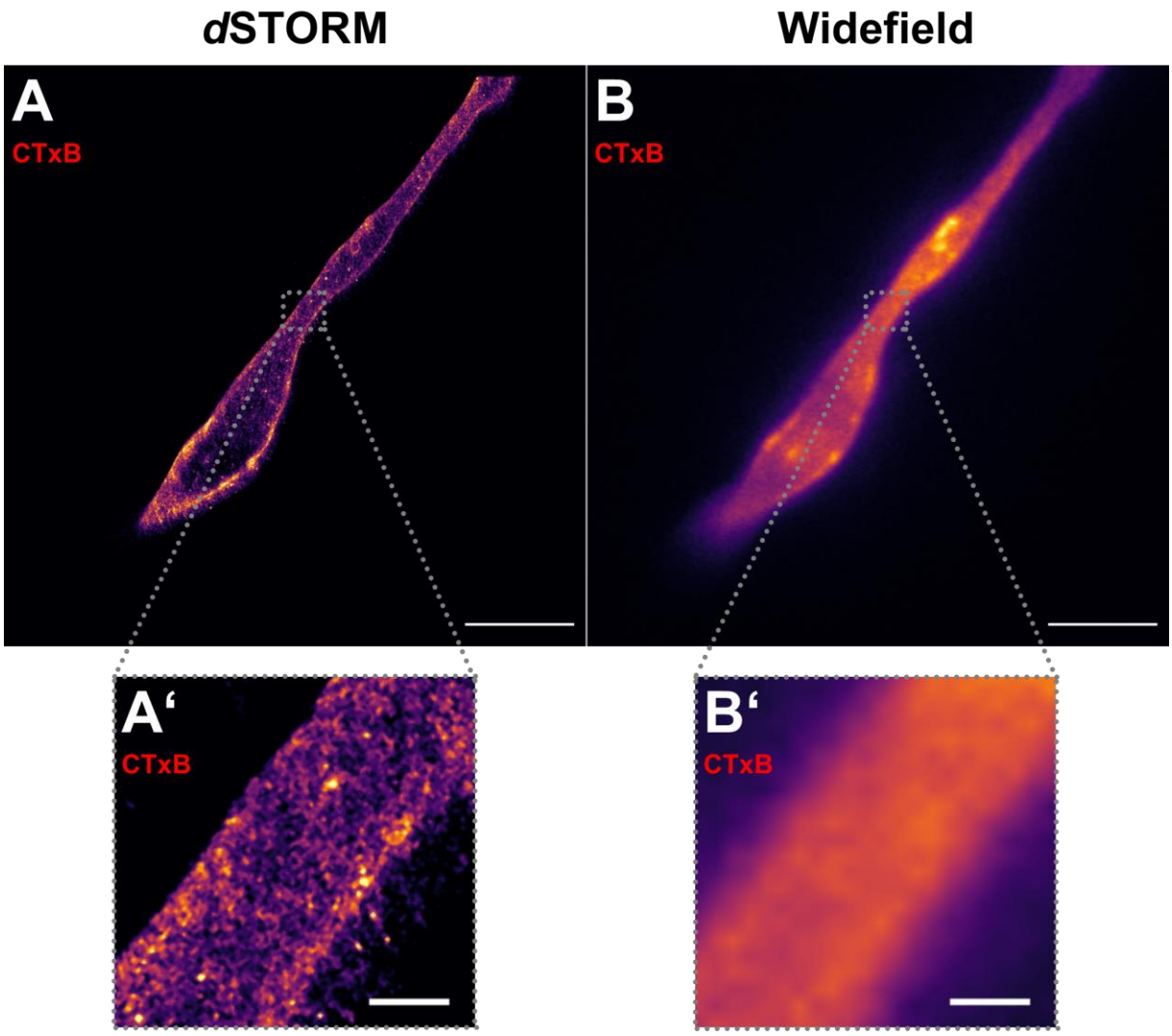

Figure 27: *d*STORM microscopy of control neurons. Overview of (A) reconstructed *d*STORM photomicrograph, in comparison with (B) conventional widefield recording of a CTxB labelled neuron. Close-up comparison of (A') *d*STORM and (B') widefield technique. Scale bars: 5 µm (A, B); 500 nm (A', B').

Abbreviations: CTxB = Cholera toxin, B subunit; *d*STORM = direct stochastic optical reconstruction microscopy; Data acquisition by Jan Schlegel (M.Sc.).

6 Discussion

6.1 Summary of main results

The main goal of our study was to establish an *in vitro* disease model for FD, based on biomaterial obtained from patients with a diverse pain phenotype and investigate the underlying cellular mechanisms of FD-associated pain and small fiber pathology. We generated fully characterized iPSC lines from a female (Klein et al., 2018) and two male patients. We derived neurons, expressing key sensory markers on the protein and the RNA level, showing pathognomonic Gb3 accumulations, neural activity, and electrophysiological differences, likely caused by functional alterations of ion channel activity. Challenging TK8 neurons with TNF, a typical trigger for FD pain (Üçeyler et al., 2019) did not change neuronal Gb3 load in a pilot experiment. Mature iPSC-derived neurons showed age-dependent Gb3 accumulation patterns and responded to pharmacological intervention by ERT with reduction in total Gb3 load. We further succeeded in visualizing Gb3 within neuronal lysosomes, which was not shown before. Additionally, we introduced a highly specific TRPV1-labeling and showed that our neurons are suitable for state-of-the art analysis using *d*STORM and SIM microscopy.

6.2 iPSC-derived sensory neurons as a potent tool in pain research

Modelling pain *in vitro* is a challenge since pain is a subjective experience and the perceived intensity has a high inter-individual variability (Cohen et al., 2018). However, to investigate potential mechanisms underlying pain, *in vitro* systems are still a valuable tool allowing assessment of pain-associated parameters, such as neuronal excitability (Chung and Chung, 2002), spontaneous activity (Xie et al., 2005), and firing rate (Yang et al., 2018). *In vitro* tools are increasingly established and applied in diverse research fields such as psychiatric disorders (Noh et al., 2017), neurodegenerative diseases (Li et al., 2018), and also pain syndromes (Eberhardt et al., 2015). In a recent study, patient-specific iPSC-derived sensory neurons provided a suitable basis to identify pharmacological treatment options against refractory pain (Namer et al., 2018). Analysis of sensory neurons derived from iPSC with a pathological Na_v 1.7 mutation, a major ion channel involved in pain (Kretschmer et al., 2002), revealed higher spontaneous activity compared to wildtype cells based on microelectrode array experiments. Application of the anticonvulsant lacosamide resulted in reduced spontaneous firing *in vitro* and relieved pain in the

patient (Namer et al., 2018). Another example for the usefulness of patient-derived sensory neurons in pain research is the investigation of the diverse phenotypes in patients with the same disease-associated mutation. A family carrying a pathogenic Na_v 1.7 mutation causing inherited erythromelalgia, but with diverse pain profiles was investigated using individual iPSC-derived sensory neurons (Mis et al., 2018). Applying whole genome sequencing the authors found a patient-specific mutation in a pain modulating gene, which contributed to interindividual differences in nociception *in vitro* and *in vivo* (Mis et al., 2018). Congenital insensitivity to pain caused by loss-of-function mutations in the gene encoding Na_v 1.7 was investigated using iPSC-derived sensory neurons revealing that Na_v 1.7 is a key regulator of neuronal excitability and that blockers for this channel currently in clinical trials lack specificity (McDermott et al., 2019). These examples show that utilizing iPSC and their downstream applications may help to elaborate personalized treatment options and investigate patient-specific phenotypes.

For FD, iPSC-based disease models are still rare. The first patient specific FD-iPSC line was published in 2013 showing membranous cytoplasmic bodies, but subsequent differentiation into mature cells was not successful, likely due to intracellular alterations by Gb3 (Kawagoe et al., 2013). iPSC derived cardiomyocytes of FD patients were successfully used to investigate the efficacy of substrate reduction therapy on Gb3 clearance (Itier et al., 2014) and establish a high-content analysis-based drug screening platform (Kuramoto et al., 2018). Still, there are no studies using *in vitro* models for FD pain research; the X-linked nature of FD may be one reason, a major challenge in iPSC research (Dandulakis et al., 2016).

6.3 Suitabilty of iPSC from female patients for disease modelling

Epigenetic mechanisms, such as methylation or acetylation lead to gene silencing or activation, respectively. During X-chromosomal inactivation (XCI), histone methylation leads to the formation of heterochromatin, blocking transcription of most genes from one X-chromosome (X_i), but leaving the other X-chromosome active (X_a) and usually results in a 50:50 or 60:40 XCI in healthy individuals (Chow et al., 2005). As described (see **section 3.2.1**), reprogramming to iPSC leads to remodeling of the epigenome, also affecting the XCI pattern in these cells. The mechanism of XCI during reprogramming is still under investigation, but studies either point towards a reactivation of the once silenced X-chromosome and thus leading to a novel

X_aX_i/X_iX_a distribution (Lagarkova et al., 2010) or a retained XCI pattern, originating from the somatic cells to be reprogrammed (Tchieu et al., 2010). These contradictory findings may be the result of biological variability of the cells during reprogramming (Bruck and Benvenisty, 2011). Long-term cultivation of iPSC might also have an impact on XCI, leading to an erosion of the inactivation pattern in favor of one chromosome, resulting in a 100:0 XCI distribution (Mekhoubad et al., 2012).

Our late FD-iPSC (p>5) derived from a female FD patient showed a skewed XCI with a ratio of 100:0 which is in line with the mentioned literature. Due to the presence of Gb3 accumulations in early (p<5) and the absence of accumulations in late FD-iPSC, we speculate that erosion of XCI developed over time, leading to a homogenous population of X_aX_i, and not X_aX_i/X_iX_a cells. Although, it cannot be determined which chromosome is favored during XCI in this case, the lack of Gb3 accumulations and the absence of mutated GLA on a transcriptomic level strongly suggests a complete inactivation of the X-chromosome carrying the disease-associated mutation. Paternal DNA is needed to reach cytogenetic proof. Another mechanism, yet less likely than XCI erosion, is a potential selective disadvantage of cells carrying mutated *GLA*, leading to a selection for healthy cells *in vitro*.

These findings need to be considered when iPSC are used for X-linked disease modelling, an ongoing field of investigation (Cheung et al., 2012). A possible approach to generate homogenous disease cell lines could be to utilize FACS and sorting cells early after reprogramming for their phenotype based on a reliable marker. In FD, STxB could be used to distinguish and isolate cells with Gb3 accumulations or increased membrane-bound Gb3. This would eliminate any evolutionary pressure in heterogeneous cell populations, although the challenge of eroding XCI persists. When using such cell lines, close monitoring is needed to ensure that the desired phenotype is present *in vitro* (Dandulakis et al., 2016). For downstream differentiation experiments, affected and healthy cells from the same patient could be cultivated together for a limited time to mimic the *in vivo* distribution. For male patients, XCI does not play a role and thus simplifies the establishment of new protocols and the downstream analysis.

6.4 iPSC and iPSC-derived sensory neurons from male FD patients

We did not find any differences in the proliferation properties or cell viability of iPSC or neurons between the control line and the FD lines. In terms of morphology or total Gb3 load, no differences were found between a patient with (TK8) and without (TK9) pain. Both showed a similar distribution of neuronal Gb3 accumulations and mature (i.e. > 6 weeks) cells responded well to ERT whereas cells from the control line showed no Gb3 accumulations at all. We used patients with two different nonsense mutations to test our disease model in a worst-case scenario: almost a complete lack of functional GLA, as reflected by pathologically reduced GLA-activity *in vivo* (see **Table 1**). Nonetheless, our model can also be used to investigate the effect of missense mutations, which is of particular interest in finding new therapeutic approaches, or mutations responding to chaperone therapy (Giugliani et al., 2013). Generating patient-specific sensory neurons offers the possibility to investigate the response to novel pharmacological compounds not only on the Gb3 load, but also on electrophysiological properties of the affected neurons. This system can be used to evaluate patient-specific alterations in neuronal activity, treat the neurons *in vitro* with a suitable drug, and transfer this knowledge to the patient in a bench-to-bedside approach (Namer et al., 2018).

6.5 Pharmacological response and Gb3 accumulations

A suitable *in vitro* disease model not only mimics disease phenotype, but also responds to common therapies, such as reduction of cellular Gb3 load by ERT (Itier et al., 2014). Our mature FD neurons showed the expected decrease of Gb3 accumulations upon incubation with exogenous GLA, making it an applicable model to investigate the effect of drugs on intraneuronal Gb3 depositions. Interestingly, we found different patterns of Gb3 accumulations depending on the duration of cultivation. While in young neurons (i.e. 1 week old), Gb3 was focally distributed, mature neurons mainly showed scattered Gb3. The latter was cleared by ERT, indicating that exogenous GLA can enzymatically break down and thus reduce Gb3 load in these cells. Focal accumulations, however, were resistant to treatment in young and mature neurons. Although this may be an artifact of our *in vitro* model, it also may have relevance for the *in vivo* situation since diversity in treatment response is a frequent clinical observation and it was shown that distinct Gb3 isoforms are resistant to ERT in kidney cells (Kodama et al., 2017).

Another interesting question is, if these focal Gb3 accumulations are also localized inside individual lysosomes, as we showed using SIM for scattered depositions. Gb3 was also found outside lysosomes, which may point towards lysosomal rupture, due to a Gb3 overload and might influence cellular dynamics (Hsu et al., 2019).

In a pilot experiment, we challenged our neurons with TNF, to simulate an inflammatory environment, known to increase the Gb3 load in white blood cells (Üçeyler et al., 2019). It is known that TNF, amongst other pro-inflammatory cytokines forms a positive-feedback loop with Gb3, which results in an increased Gb3 expression caused by TNF (Eisenhauer et al., 2001) and vice versa (Sakiri et al., 1998). Since fever is a major trigger of FD pain, a link between TNF, Gb3, and pain is likely. We aimed at investigating the effect of TNF on the Gb3 load, to see if this feedback-loop also exists in our neurons. We speculated that an increase of Gb3, induced by TNF can lead to abnormal neuronal activity, caused by an upregulation of nociceptive ion channels, as it was shown in old GLA KO mice (Lakoma et al., 2016). We did not detect an effect of TNF on Gb3, which may be due to several factors. First, it is known that iPSC-derived neurons resemble tissue of the first trimester of embryogenesis (Mariani et al., 2012); hence, TNF might activate different pathways not related to Gb3 accumulation than in adult neurons. Second, we did not investigate the expression of the TNF receptor 1 on our neurons, known to be expressed on sensory neurons (Li et al., 2004). A lack of this receptor could explain the unresponsiveness of our neurons. Third, Gb3 accumulations did change during TNF treatment in individual cells, e.g. more accumulations per cell, but were not reflected by our assay, because we only quantified positive cells, but not the individual cellular load. A workaround for this problem might be utilization of deep learning tools, such as DeepFLaSH (Segebarth et al., 2018), to automatize and maximize data output. Finally, this was a pilot experiment and we used the TNF concentration and incubation time suitable for white blood cells (Üçeyler et al., 2019), which likely have to be adapted to this system.

6.6 Electrophysiological properties of iPSC-derived sensory neurons

Functional testing of iPSC-derived sensory neurons using confocal Ca^{2+} imaging revealed rhythmic fluctuations of intracellular Ca^{2+} levels, strongly suggesting spontaneous firing and organized network activity (O'Donovan et al., 1994). To maximize contrast and minimize out-of-focus fluorescence, we decided to use a

CLSM for data acquisition. A drawback of this method is a low sampling rate of 0.25 Hz, which made detection of single APs with a duration of <5 ms impossible. We aimed at investigating binned action potentials (Davies et al., 2019) over a period of 8 min. Subsequent analysis using NA^3 software (Prada et al., 2018) showed that a sampling rate of 0.25 Hz was too low for effective analysis. Still, the collected data strongly suggests spontaneous network activity in all analyzed cell lines, indicating viable neuronal cultures, suitable for live-cell imaging experiments.

Patch clamp analysis revealed a decreased AP threshold difference ($V_{ThresholdDiff}$) in neurons from TK8 (patient with pain), compared to TK9 (patient without pain), and healthy control cells. $V_{ThresholdDiff}$ is determined to describe the degree of excitability of neurons in relation to the resting membrane potential. A lower $V_{ThresholdDiff}$ means that a smaller stimulus is required to initiate APs, which was the case for cells from the patient with FD pain. *In vivo*, this may result in a hyperexcitability of nociceptors and thus lead to pain (Ratte and Prescott, 2016). Upon stimulation, the Na_v 1.1, 1.2, 1.3, 1.6, and 1.9 channels depolarize the membrane until the AP threshold is reached, which triggers the opening of Na_v 1.7, the AP threshold defining channel (Meents et al., 2019). Altered steady-state kinetics, for example hyperpolarized activation, or depolarized inactivation of Na_v 1.7 may be the cause for the reduced AP threshold, leading to a more easily excitable neuron. It was also shown *in vitro* that an increased Gb3 load in human embryonic kidney 293 (HEK) cells expressing Na_v 1.7 had lower sodium currents compared to HEK cells with a normal Gb3 load. This effect was recovered by ERT incubation, directly linking Na_v 1.7 and Gb3 (Hofmann et al., 2018).

The mechanisms underlying reduced $V_{ThresholdDiff}$ are still elusive, but a direct link between Gb3 and Na_v 1.7 provides a starting point for further investigations, e.g. by using colocalization studies with super-resolution microscopy to investigate Gb3 - ion channel interactions on the membrane of iPSC-derived neurons. It was shown in the GLA KO mouse model of FD that an increased Gb3 load in aortic endothelial cells leads to a downregulation of the Ca^{2+} gated potassium channel K_{Ca} 3.1 by clathrin mediated endocytosis (Choi et al., 2014). Despite the fact that this was found using murine, non-neuronal cells, it still indicates that Gb3 may have a direct influence on the ion channel composition of membranes, likely also in neurons.

Lacking single ion channel investigations, the reason for the altered $V_{ThresholdDiff}$ is still unknown, but indicates that our *in vitro* model not only mimics the Gb3 accumulation phenotype, but also reflects electrophysiological changes in affected neurons. Identifying the altered ion channels will be an important step towards a more personalized analgesic treatment for patients with FD.

6.7 Labeling of Gb3 and TRPV1

To improve labelling of Gb3 for downstream optical analysis, we used dye-conjugated STxB (Majoul et al., 2002). This toxin is known to specifically bind to Gb3 (Hughes et al., 2000) and to some extend Gb4, but with a much lower affinity (Zumbrun et al., 2010). A major advantage of STxB is its specifity, resulting in labelling experiments with virtually no background signal, making it a suitable approach for demanding imaging techniques, such as *d*STORM or SIM. Furthermore, STxB can easily be used to detect membrane bound Gb3 and utilized in a live-cell imaging environment to visualize the endoplasmic reticulum, due to its intracellular trafficking route (Yu and Haslam, 2005). One drawback of this method is the detection of Gb4 in addition to Gb3, which makes it impossible to differentiate both. We still decided to identify $STxB^+$ profiles as Gb3, due to the 3-fold higher affinity of STxB for Gb3 (Gallegos et al., 2012). Furthermore, it was shown that Gb4 was not increased in GLA KO mice, compared to wildtype littermates in an *in vitro* rodent model of primary aortic endothelial cells (Shu et al., 2005). Together with the complete absence of $STxB^+$ accumulations in control skin, iPSC, and neurons, we hypothesized that if Gb4 is present in our cells, its concentration is most likely below the detection threshold of our assay and hence of minor relevance.

We also introduced a new approach to visualize TRPV1, a major player in nociception (Immke and Gavva, 2006). Despite numerous commercial antibodies available against TRPV1, in our hands the immunoreactions showed a high background signal and some unspecific binding, making the analysis unreliable. By utilizing the selectivity of DkTx for TRPV1 as agonist (Bohlen et al., 2010), combined with an N-terminal His_6-Tag, we were able to selectively label $TRPV1^+$ fibers, using a highly specific anti-His_6-antibody. Besides its selectivity, a major advantage of this approach is its suitability for live-cell imaging. It is possible to incubate and visualize neurons live with the toxin and simultaneously investigate neuronal activity, caused by TRPV1 activation using Ca^{2+} imaging. As a caveat, excitotoxicity caused by

irreversible binding of the toxin and increased Ca^{2+} influx (Choi, 1988) need to be taken into account.

6.8 Improved sensory differentiation protocol

We used published differentiation protocols as basis for our approach (Chambers et al., 2012; Eberhardt et al., 2015) and established a refined procedure to maximize reliability and neuronal survival. Current protocols aim at generating a highly purified sensory neuron culture early on, with as few non-neuronal cells as possible by using mitomycin C as cytostatic to effectively eliminate all mitotic cells. After initial experiments, we chose FdU because of better neuronal survival (Hui et al., 2016). In our hands, FdU routinely led to the formation of a feeder-layer. This is beneficial for neurons in terms of adhesion to cells, instead of an artificial extracellular matrix, but also for media composition (Petschnik et al., 2011). Mimicking the *in vivo* situation, where neurons also grow in symbiosis with e.g. glial cells (Stevens, 2003), our neurons are cultivated in a heterogeneous system, consisting of the desired neurons and cells supporting neuronal survival. The exact composition of this feeder-layer remains elusive and an in-depth characterization is needed. Nonetheless, we observed that neuronal viability was more robust in cultures with this feeder-layer, compared to pure neuronal cultures. We also chose to change the medium as few as possible to minimize physical (LaPlaca and Thibault, 1997), osmotic (Brocker et al., 2012) and nutrient (Young et al., 2009) stress on the neurons. One disadvantage of this method is the relative heterogeneity of our neuronal cultures, although the feeder-layer itself tends to degenerate during long-term cultivation and can be further depleted by replating mature neurons in the presence of FdU. A “contamination” with non-neuronal cells might be a challenge for highly sensitive assays, such as qRT-PCR or RNA sequencing (Wang et al., 2019). Still, with our system, iPSC-derived sensory neurons are robustly generated and maintained for at least eight weeks, expensive media consumption and hands-on time is minimized. Our neurons can be cultivated in a large scale and replated for the desired analysis in smaller cultivation vessels, making it a viable tool for pain research, not only for FD, but diseases affecting the PNS in general.

6.9 The diversity of pain in FD and experimental therapies

The pain phenotype in FD is diverse (Üçeyler et al., 2014), with the underlying mechanisms still under investigation. Although it is accepted that Gb3 plays a major

role in FD pain, there are conflicting results regarding reduction of the Gb3 load via ERT and pain relief. It was shown in several studies that ERT did not change pain intensity in adults (Eng et al., 2001b; Wilcox et al., 2004; Vedder et al., 2007; Üçeyler et al., 2014), whereas other studies reported pain reduction after ERT (Schiffmann et al., 2001; Hilz et al., 2004; Watt et al., 2010), and others reported some analgesic effect in children treated with ERT (Ries et al., 2006; Ramaswami et al., 2007). A possible explanation for the analgesic efficacy of ERT in children can be a long-term effect of Gb3 on post-mitotic cells, such as neurons, leading to permanent cellular changes, which cannot be reversed by ERT in adults. In children, however, neural plasticity is much more pronounced (Moore and Murphy, 2016) and early ERT might reverse these effects, thus alleviating pain. Furthermore, it was reported that patients with an early intervention with ERT have a better clinical outcome than patients who started treatment late (Germain et al., 2015). This further points towards time-dependent pathological cellular changes, which may be reversed by reducing Gb3 as soon as possible.

Even in families carrying the same mutation in *GLA*, the disease phenotype is differing from one individual to another. A case study reports on two brothers, genetically identical for *GLA*, with no enzyme activity at all with the younger brother having severe symptoms, whereas the older one is asymptomatic (Cammarata et al., 2015). Such constellations make a phenotype-genotype correlation difficult. The underlying mechanisms of these diverse phenotypes are still elusive, but it is of note that the screening for mutations only in *GLA* might not be sufficient and leaves other disease-associated genomic changes undetermined. A recent study used whole-exome sequencing of iPSC-derived sensory neurons to investigate inherited erythromyelalgia and its diverse pain phenotype. It was shown that the moderately affected mother had a mutation on a pain modulating gene, additionally to the familial Na_v 1.7 mutation, known to cause erythromyelalgia. This additional mutation led to a downregulation of neuronal excitability in the mother, thus decreased pain, compared to the severely affected son, lacking this mutation (Mis et al., 2018). The combination of whole exome sequencing and patient-derived sensory neurons might be a viable tool to detect further mutations and their effects on neuronal excitability.

Besides genomic mutation, it has been discussed that the epigenome might play a role in the manifestation of different disease phenotypes caused by the same

mutation. It has been shown that the epigenome is highly flexible and can easily be altered, e.g. by a dietary change (Zhang and Kutateladze, 2018), physical activity (Blackburn et al., 2015), chronic pain (Liang et al., 2015), but also environmental factors such as metal exposure (Takiguchi et al., 2003) or air pollution (Yauk et al., 2008). The transition in some patients from acute to chronic pain after injury for example, is suspected to be a result of epigenetic remodeling during the acute pain phase (Buchheit et al., 2012). Diverse epigenomes between individuals carrying the same disease-associated mutation can thus be a major player in pain severity. For models based on iPSC, this is a challenge, because during reprogramming, the epigenome is severely altered to achieve pluripotency (Godini et al., 2018), thus potentially erasing pain-relevant epigenetic information.

A hallmark of FD is the triggerable pain by physical activity, thermal stimuli, and fever (Politei et al., 2016). These triggers have in common that they result in an elevated generalized body temperature (fever, activity) or locally elevated and/or reduced body temperature (thermal stimuli). A major heat sensing ion channel is TRPV1 (Voets et al., 2004), causing pain upon activation. It was shown in the GLA KO mouse model that the protein expression of TRPV1 is elevated in mice (Lakoma et al., 2016) and that they show heat hypersensitivity upon TRPV1 activation in contrast to wildtype animals (Hofmann et al., 2018). It was also shown that TRPM8, a cold sensing ion channel (Liu and Qin, 2011), is downregulated (Lakoma et al., 2014) and Na_v 1.8, an ion channel involved in neuropathic pain (Amir et al., 2006), is upregulated in GLA KO mice (Lakoma et al., 2014). This points towards an altered ion channel expression on affected neurons. An increased expression of TRPV1 on nociceptors might lead to hyperexcitability due to temperature changes, caused by an elevated body temperature and thus result in pain. Furthermore, proalgesic inflammatory factors are known to reduce the thermal threshold of TRPV1 (Velisetty et al., 2017), linking fever and heat induced pain (Velisetty et al., 2017). Our *in vitro* model can be used to investigate temperature differences, proalgesic agents, and their effect on pain, e.g. by electrophysiologically (Ca^{2+} imaging or patch clamp) recording neurons at a baseline temperature, followed by a temperature increase / incubation with a proalgesic agent and comparing parameters, such as firing frequency, spontaneous activity, $V_{ThresholdDiff}$ of both conditions. Applying selective ion channel blockers can then be used to identify the causal ion channel.

ERT and chaperone therapy, the latter one not being suitable for all mutations are the only available therapeutic options for FD, creating demand for new approaches, such as gene therapy or other sources for GLA. Gene therapy for FD is already in clinical trials, with the advantage that no exogenous GLA is needed, because the genetic defect in *GLA* is corrected using lentiviral vectors *ex vivo* in hematopoietic stem cells and transplanted back into the patient. These cells and their daughter cells secrete functional GLA, which is taken up by GLA deficient cells, reducing Gb3 load, without the need of biweekly ERT. This therapeutic option is currently being evaluated in a phase II clinical trial (https://clinicaltrials.gov/; Identifier: NCT03454893).

A major problem of ERT can be the formation of neutralizing anti-drug antibodies (Mauhin et al., 2015), produced by the patient as reaction to exogenous GLA, manufactured in mammalian cell systems, which can greatly reduce the efficiency of ERT (Lenders et al., 2016). Recently, the plant-derived α-galactosidase A1.1 was discovered which efficiently lowered lyso-Gb3 levels in FD fibroblasts (Kytidou et al., 2018). It was also shown that A1.1 was delivered into lysosomes, did not cross-react with neutralizing antibodies, and is much more cost efficient, allowing application of higher dosages to increase organ penetration, making it a promising approach for FD (Kytidou et al., 2018). GLA extracted from the moss *Physcomitrella patens* is another approach to prevent immune-mediated reduction of ERT efficiency. Moss-derived GLA was well tolerated and a single dose resulted in a prolonged reduction of urinary Gb3 and plasma lyso-Gb3 concentrations after 28 days in a phase I clinical study (Hennermann et al., 2019). These, and future experimental approaches can be tested in our *in vitro* system for its efficiency of neuronal Gb3 depletion.

6.10 Conclusion and outlook

Our initial aim was to investigate possible differences of sensory neurons in patients with a varying pain phenotype by using the iPSC technology. We succeeded in generating and characterizing iPSC from a female, and two male patients, establish a reliable differentiation protocol and generate patient-specific sensory neurons. We showed that our FD-neurons reconstitute the disease phenotype and respond to ERT and adapted state-of-the-art methods for neuronal analysis and with these, unveiled new insights into cellular localization of Gb3, which can now be explored in more detail. Furthermore, we showed that neurons from a patient with pain differ in their

electrophysiological properties compared to neurons from a patient without pain, making a direct connection between our *in vitro* model and the clinical symptoms. Future work will be the extended super-resolution imaging of Gb3 accumulations and their potential influence on ion channel activity and cellular processes, leading to hyperexcitability and denervation. Microscopically, we aim at visualizing the pathological effect of Gb3 in neurons in a live-cell imaging environment. Electrophysiologically, Ca^{2+} imaging protocols will be optimized and pharmacological investigations using patch-clamp techniques are needed to pinpoint altered neuronal firing properties to individual ion channels and thus offer therapeutic options, which can then be tested in our *in vitro* system. To increase output and move forward towards a more personalized analgesic treatment for FD patients, experiments using microelectrode arrays should be considered to simultaneously test multiple drug candidates (Scelfo et al., 2012) and read-out their effect on the electrophysiology of sensory neurons respectively on FD-associated pain.

7 References

Aerts, J.M., Groener, J.E., Kuiper, S., Donker-Koopman, W.E., Strijland, A., Ottenhoff, R., Van Roomen, C., Mirzaian, M., Wijburg, F.A., Linthorst, G.E., Vedder, A.C., Rombach, S.M., Cox-Brinkman, J., Somerharju, P., Boot, R.G., Hollak, C.E., Brady, R.O., and Poorthuis, B.J. (2008). Elevated globotriaosylsphingosine is a hallmark of Fabry disease. *Proc Natl Acad Sci U S A* 105**,** 2812-2817.

Alegra, T., Vairo, F., De Souza, M.V., Krug, B.C., and Schwartz, I.V. (2012). Enzyme replacement therapy for Fabry disease: A systematic review and meta-analysis. *Genet Mol Biol* 35**,** 947-954.

Amir, R., Argoff, C.E., Bennett, G.J., Cummins, T.R., Durieux, M.E., Gerner, P., Gold, M.S., Porreca, F., and Strichartz, G.R. (2006). The role of sodium channels in chronic inflammatory and neuropathic pain. *J Pain* 7**,** S1-29.

Arends, M., Wanner, C., Hughes, D., Mehta, A., Oder, D., Watkinson, O.T., Elliott, P.M., Linthorst, G.E., Wijburg, F.A., Biegstraaten, M., and Hollak, C.E. (2017). Characterization of Classical and Nonclassical Fabry Disease: A Multicenter Study. *J Am Soc Nephrol* 28**,** 1631-1641.

Bangari, D.S., Ashe, K.M., Desnick, R.J., Maloney, C., Lydon, J., Piepenhagen, P., Budman, E., Leonard, J.P., Cheng, S.H., Marshall, J., and Thurberg, B.L. (2015). alpha-Galactosidase A knockout mice: progressive organ pathology resembles the type 2 later-onset phenotype of Fabry disease. *Am J Pathol* 185**,** 651-665.

Baron, R., Binder, A., and Wasner, G. (2010). Neuropathic pain: diagnosis, pathophysiological mechanisms, and treatment. *Lancet Neurol* 9**,** 807-819.

Blackburn, H.L., Mcerlean, S., Jellema, G.L., Van Laar, R., Vernalis, M.N., and Ellsworth, D.L. (2015). Gene expression profiling during intensive cardiovascular lifestyle modification: Relationships with vascular function and weight loss. *Genom Data* 4**,** 50-53.

Bohlen, C.J., Priel, A., Zhou, S., King, D., Siemens, J., and Julius, D. (2010). A bivalent tarantula toxin activates the capsaicin receptor, TRPV1, by targeting the outer pore domain. *Cell* 141**,** 834-845.

Brocker, C., Thompson, D.C., and Vasiliou, V. (2012). The role of hyperosmotic stress in inflammation and disease. *Biomol Concepts* 3**,** 345-364.

Bruck, T., and Benvenisty, N. (2011). Meta-analysis of the heterogeneity of X chromosome inactivation in human pluripotent stem cells. *Stem Cell Res* 6**,** 187-193.

Buchheit, T., Van De Ven, T., and Shaw, A. (2012). Epigenetics and the transition from acute to chronic pain. *Pain Med* 13**,** 1474-1490.

Buganim, Y., Faddah, D.A., and Jaenisch, R. (2013). Mechanisms and models of somatic cell reprogramming. *Nat Rev Genet* 14**,** 427-439.

Burlina, A.P., Sims, K.B., Politei, J.M., Bennett, G.J., Baron, R., Sommer, C., Moller, A.T., and Hilz, M.J. (2011). Early diagnosis of peripheral nervous system involvement in Fabry disease and treatment of neuropathic pain: the report of an expert panel. *BMC Neurol* 11**,** 61.

Cammarata, G., Fatuzzo, P., Rodolico, M.S., Colomba, P., Sicurella, L., Iemolo, F., Zizzo, C., Alessandro, R., Bartolotta, C., Duro, G., and Monte, I. (2015). High variability of Fabry disease manifestations in an extended Italian family. *Biomed Res Int* 2015**,** 504784.

Chambers, S.M., Qi, Y., Mica, Y., Lee, G., Zhang, X.J., Niu, L., Bilsland, J., Cao, L., Stevens, E., Whiting, P., Shi, S.H., and Studer, L. (2012). Combined small-

molecule inhibition accelerates developmental timing and converts human pluripotent stem cells into nociceptors. *Nat Biotechnol* 30**,** 715-720.
Cheung, A.Y., Horvath, L.M., Carrel, L., and Ellis, J. (2012). X-chromosome inactivation in rett syndrome human induced pluripotent stem cells. *Front Psychiatry* 3**,** 24.
Choi, D.W. (1988). Calcium-mediated neurotoxicity: relationship to specific channel types and role in ischemic damage. *Trends Neurosci* 11**,** 465-469.
Choi, S., Kim, J.A., Na, H.Y., Cho, S.E., Park, S., Jung, S.C., and Suh, S.H. (2014). Globotriaosylceramide induces lysosomal degradation of endothelial KCa3.1 in fabry disease. *Arterioscler Thromb Vasc Biol* 34**,** 81-89.
Chow, J.C., Yen, Z., Ziesche, S.M., and Brown, C.J. (2005). Silencing of the mammalian X chromosome. *Annu Rev Genomics Hum Genet* 6**,** 69-92.
Chung, J.M., and Chung, K. (2002). Importance of hyperexcitability of DRG neurons in neuropathic pain. *Pain Pract* 2**,** 87-97.
Cohen, M., Quintner, J., and Van Rysewyk, S. (2018). Reconsidering the International Association for the Study of Pain definition of pain. *Pain Rep* 3**,** e634.
Dandulakis, M.G., Meganathan, K., Kroll, K.L., Bonni, A., and Constantino, J.N. (2016). Complexities of X chromosome inactivation status in female human induced pluripotent stem cells-a brief review and scientific update for autism research. *J Neurodev Disord* 8**,** 22.
Davies, A.J., Kim, H.W., Gonzalez-Cano, R., Choi, J., Back, S.K., Roh, S.E., Johnson, E., Gabriac, M., Kim, M.S., Lee, J., Lee, J.E., Kim, Y.S., Bae, Y.C., Kim, S.J., Lee, K.M., Na, H.S., Riva, P., Latremoliere, A., Rinaldi, S., Ugolini, S., Costigan, M., and Oh, S.B. (2019). Natural Killer Cells Degenerate Intact Sensory Afferents following Nerve Injury. *Cell* 176**,** 716-728 e718.
Desnick, R.J., Brady, R., Barranger, J., Collins, A.J., Germain, D.P., Goldman, M., Grabowski, G., Packman, S., and Wilcox, W.R. (2003). Fabry disease, an under-recognized multisystemic disorder: expert recommendations for diagnosis, management, and enzyme replacement therapy. *Ann Intern Med* 138**,** 338-346.
Eberhardt, E., Havlicek, S., Schmidt, D., Link, A.S., Neacsu, C., Kohl, Z., Hampl, M., Kist, A.M., Klinger, A., Nau, C., Schuttler, J., Alzheimer, C., Winkler, J., Namer, B., Winner, B., and Lampert, A. (2015). Pattern of Functional TTX-Resistant Sodium Channels Reveals a Developmental Stage of Human iPSC- and ESC-Derived Nociceptors. *Stem Cell Reports* 5**,** 305-313.
Eiselleova, L., Matulka, K., Kriz, V., Kunova, M., Schmidtova, Z., Neradil, J., Tichy, B., Dvorakova, D., Pospisilova, S., Hampl, A., and Dvorak, P. (2009). A complex role for FGF-2 in self-renewal, survival, and adhesion of human embryonic stem cells. *Stem Cells* 27**,** 1847-1857.
Eisenhauer, P.B., Chaturvedi, P., Fine, R.E., Ritchie, A.J., Pober, J.S., Cleary, T.G., and Newburg, D.S. (2001). Tumor necrosis factor alpha increases human cerebral endothelial cell Gb3 and sensitivity to Shiga toxin. *Infection and immunity* 69**,** 1889-1894.
Endo, Y., Osumi, N., and Wakamatsu, Y. (2002). Bimodal functions of Notch-mediated signaling are involved in neural crest formation during avian ectoderm development. *Development* 129**,** 863-873.
Eng, C.M., Banikazemi, M., Gordon, R.E., Goldman, M., Phelps, R., Kim, L., Gass, A., Winston, J., Dikman, S., Fallon, J.T., Brodie, S., Stacy, C.B., Mehta, D., Parsons, R., Norton, K., O'callaghan, M., and Desnick, R.J. (2001a). A phase

1/2 clinical trial of enzyme replacement in fabry disease: pharmacokinetic, substrate clearance, and safety studies. *Am J Hum Genet* 68**,** 711-722.
Eng, C.M., Guffon, N., Wilcox, W.R., Germain, D.P., Lee, P., Waldek, S., Caplan, L., Linthorst, G.E., Desnick, R.J., and International Collaborative Fabry Disease Study, G. (2001b). Safety and efficacy of recombinant human alpha-galactosidase A replacement therapy in Fabry's disease. *N Engl J Med* 345**,** 9-16.
Fan, J.Q., Ishii, S., Asano, N., and Suzuki, Y. (1999). Accelerated transport and maturation of lysosomal alpha-galactosidase A in Fabry lymphoblasts by an enzyme inhibitor. *Nat Med* 5**,** 112-115.
Filoni, C., Caciotti, A., Carraresi, L., Cavicchi, C., Parini, R., Antuzzi, D., Zampetti, A., Feriozzi, S., Poisetti, P., Garman, S.C., Guerrini, R., Zammarchi, E., Donati, M.A., and Morrone, A. (2010). Functional studies of new GLA gene mutations leading to conformational Fabry disease. *Biochim Biophys Acta* 1802**,** 247-252.
Fusaki, N., Ban, H., Nishiyama, A., Saeki, K., and Hasegawa, M. (2009). Efficient induction of transgene-free human pluripotent stem cells using a vector based on Sendai virus, an RNA virus that does not integrate into the host genome. *Proc Jpn Acad Ser B Phys Biol Sci* 85**,** 348-362.
Gallegos, K.M., Conrady, D.G., Karve, S.S., Gunasekera, T.S., Herr, A.B., and Weiss, A.A. (2012). Shiga toxin binding to glycolipids and glycans. *PLoS One* 7**,** e30368.
Germain, D.P. (2010). Fabry disease. *Orphanet J Rare Dis* 5**,** 30.
Germain, D.P., Charrow, J., Desnick, R.J., Guffon, N., Kempf, J., Lachmann, R.H., Lemay, R., Linthorst, G.E., Packman, S., Scott, C.R., Waldek, S., Warnock, D.G., Weinreb, N.J., and Wilcox, W.R. (2015). Ten-year outcome of enzyme replacement therapy with agalsidase beta in patients with Fabry disease. *J Med Genet* 52**,** 353-358.
Germain, D.P., Hughes, D.A., Nicholls, K., Bichet, D.G., Giugliani, R., Wilcox, W.R., Feliciani, C., Shankar, S.P., Ezgu, F., Amartino, H., Bratkovic, D., Feldt-Rasmussen, U., Nedd, K., Sharaf El Din, U., Lourenco, C.M., Banikazemi, M., Charrow, J., Dasouki, M., Finegold, D., Giraldo, P., Goker-Alpan, O., Longo, N., Scott, C.R., Torra, R., Tuffaha, A., Jovanovic, A., Waldek, S., Packman, S., Ludington, E., Viereck, C., Kirk, J., Yu, J., Benjamin, E.R., Johnson, F., Lockhart, D.J., Skuban, N., Castelli, J., Barth, J., Barlow, C., and Schiffmann, R. (2016). Treatment of Fabry's Disease with the Pharmacologic Chaperone Migalastat. *N Engl J Med* 375**,** 545-555.
Giugliani, R., Waldek, S., Germain, D.P., Nicholls, K., Bichet, D.G., Simosky, J.K., Bragat, A.C., Castelli, J.P., Benjamin, E.R., and Boudes, P.F. (2013). A Phase 2 study of migalastat hydrochloride in females with Fabry disease: selection of population, safety and pharmacodynamic effects. *Mol Genet Metab* 109**,** 86-92.
Godini, R., Lafta, H.Y., and Fallahi, H. (2018). Epigenetic modifications in the embryonic and induced pluripotent stem cells. *Gene Expr Patterns* 29**,** 1-9.
Guerard, N., Oder, D., Nordbeck, P., Zwingelstein, C., Morand, O., Welford, R.W.D., Dingemanse, J., and Wanner, C. (2018). Lucerastat, an Iminosugar for Substrate Reduction Therapy: Tolerability, Pharmacodynamics, and Pharmacokinetics in Patients With Fabry Disease on Enzyme Replacement. *Clin Pharmacol Ther* 103**,** 703-711.

Gurdon, J.B., Elsdale, T.R., and Fischberg, M. (1958). Sexually Mature Individuals of Xenopus laevis from the Transplantation of Single Somatic Nuclei. *Nature* 182**,** 64-65.

Hanna, J., Cheng, A.W., Saha, K., Kim, J., Lengner, C.J., Soldner, F., Cassady, J.P., Muffat, J., Carey, B.W., and Jaenisch, R. (2010). Human embryonic stem cells with biological and epigenetic characteristics similar to those of mouse ESCs. *Proceedings of the National Academy of Sciences* 107**,** 9222-9227.

Hennermann, J.B., Arash-Kaps, L., Fekete, G., Schaaf, A., Busch, A., and Frischmuth, T. (2019). Pharmacokinetics, pharmacodynamics, and safety of moss-aGalactosidase A in patients with Fabry disease. *J Inherit Metab Dis* 42**,** 527-533.

Hilz, M.J., Brys, M., Marthol, H., Stemper, B., and Dütsch, M. (2004). Enzyme replacement therapy improves function of C-, Aδ-, and Aβ-nerve fibers in Fabry neuropathy. 62**,** 1066-1072.

Hofmann, L., Hose, D., Griesshammer, A., Blum, R., Doring, F., Dib-Hajj, S., Waxman, S., Sommer, C., Wischmeyer, E., and Uceyler, N. (2018). Characterization of small fiber pathology in a mouse model of Fabry disease. *Elife* 7.

Hsu, M.-J., Chang, F.-P., Lu, Y.-H., Hung, S.-C., Wang, Y.-C., Yang, A.-H., Lee, H.-J., Sung, S.-H., Wang, Y.-F., Yu, W.-C., Hsu, T.-R., Huang, P.-H., Chang, S.-K., Dzhagalov, I., Hsu, C.-L., and Niu, D.-M. (2019). Identification of lysosomal and extralysosomal globotriaosylceramide (Gb3) accumulations before the occurrence of typical pathological changes in the endomyocardial biopsies of Fabry disease patients. *Genetics in Medicine* 21**,** 224-232.

Hughes, A.K., Stricklett, P.K., Schmid, D., and Kohan, D.E. (2000). Cytotoxic effect of Shiga toxin-1 on human glomerular epithelial cells. *Kidney Int* 57**,** 2350-2359.

Hughes, C.S., Postovit, L.M., and Lajoie, G.A. (2010). Matrigel: a complex protein mixture required for optimal growth of cell culture. *Proteomics* 10**,** 1886-1890.

Hughes, D.A., Nicholls, K., Shankar, S.P., Sunder-Plassmann, G., Koeller, D., Nedd, K., Vockley, G., Hamazaki, T., Lachmann, R., Ohashi, T., Olivotto, I., Sakai, N., Deegan, P., Dimmock, D., Eyskens, F., Germain, D.P., Goker-Alpan, O., Hachulla, E., Jovanovic, A., Lourenco, C.M., Narita, I., Thomas, M., Wilcox, W.R., Bichet, D.G., Schiffmann, R., Ludington, E., Viereck, C., Kirk, J., Yu, J., Johnson, F., Boudes, P., Benjamin, E.R., Lockhart, D.J., Barlow, C., Skuban, N., Castelli, J.P., Barth, J., and Feldt-Rasmussen, U. (2017). Oral pharmacological chaperone migalastat compared with enzyme replacement therapy in Fabry disease: 18-month results from the randomised phase III ATTRACT study. *J Med Genet* 54**,** 288-296.

Hui, C.W., Zhang, Y., and Herrup, K. (2016). Non-Neuronal Cells Are Required to Mediate the Effects of Neuroinflammation: Results from a Neuron-Enriched Culture System. *PLoS One* 11**,** e0147134.

Immke, D.C., and Gavva, N.R. (2006). The TRPV1 receptor and nociception. *Semin Cell Dev Biol* 17**,** 582-591.

Itier, J.M., Ret, G., Viale, S., Sweet, L., Bangari, D., Caron, A., Le-Gall, F., Benichou, B., Leonard, J., Deleuze, J.F., and Orsini, C. (2014). Effective clearance of GL-3 in a human iPSC-derived cardiomyocyte model of Fabry disease. *J Inherit Metab Dis* 37**,** 1013-1022.

Kawagoe, S., Higuchi, T., Otaka, M., Shimada, Y., Kobayashi, H., Ida, H., Ohashi, T., Okano, H.J., Nakanishi, M., and Eto, Y. (2013). Morphological features of iPS cells generated from Fabry disease skin fibroblasts using Sendai virus vector (SeVdp). *Mol Genet Metab* 109**,** 386-389.

Klein, T. (2016). *Generation of patient-derived peripheral sensory neurons via reprogramming and transdifferentiation of human fibroblasts into iPSCs and iNPCs.* Master of Science, University of Würzburg.

Klein, T., Günther, K., Kwok, C.K., Edenhofer, F., and Üçeyler, N. (2018). Generation of the human induced pluripotent stem cell line (UKWNLi001-A) from skin fibroblasts of a woman with Fabry disease carrying the X-chromosomal heterozygous c.708G>C (W236C) missense mutation in exon 5 of the alpha-galactosidase-A gene. *Stem Cell Res* 31**,** 222-226.

Kodama, T., Tsukimura, T., Kawashima, I., Sato, A., Sakuraba, H., and Togawa, T. (2017). Differences in cleavage of globotriaosylceramide and its derivatives accumulated in organs of young Fabry mice following enzyme replacement therapy. *Mol Genet Metab* 120**,** 116-120.

Kretschmer, T., Happel, L.T., England, J.D., Nguyen, D.H., Tiel, R.L., Beuerman, R.W., and Kline, D.G. (2002). Clinical Article Accumulation of PN1 and PN3 Sodium Channels in Painful Human Neuroma-Evidence from Immunocytochemistry. *Acta Neurochirurgica* 144**,** 803-810.

Kummer, K.K., Kalpachidou, T., Kress, M., and Langeslag, M. (2017). Signatures of Altered Gene Expression in Dorsal Root Ganglia of a Fabry Disease Mouse Model. *Front Mol Neurosci* 10**,** 449.

Kuramoto, Y., Naito, A.T., Tojo, H., Sakai, T., Ito, M., Shibamoto, M., Nakagawa, A., Higo, T., Okada, K., Yamaguchi, T., Lee, J.K., Miyagawa, S., Sawa, Y., Sakata, Y., and Komuro, I. (2018). Generation of Fabry cardiomyopathy model for drug screening using induced pluripotent stem cell-derived cardiomyocytes from a female Fabry patient. *J Mol Cell Cardiol* 121**,** 256-265.

Kytidou, K., Beekwilder, J., Artola, M., Van Meel, E., Wilbers, R.H.P., Moolenaar, G.F., Goosen, N., Ferraz, M.J., Katzy, R., Voskamp, P., Florea, B.I., Hokke, C.H., Overkleeft, H.S., Schots, A., Bosch, D., Pannu, N., and Aerts, J. (2018). Nicotiana benthamiana alpha-galactosidase A1.1 can functionally complement human alpha-galactosidase A deficiency associated with Fabry disease. *J Biol Chem* 293**,** 10042-10058.

Laaksonen, S.M., Roytta, M., Jaaskelainen, S.K., Kantola, I., Penttinen, M., and Falck, B. (2008). Neuropathic symptoms and findings in women with Fabry disease. *Clin Neurophysiol* 119**,** 1365-1372.

Lagarkova, M.A., Shutova, M.V., Bogomazova, A.N., Vassina, E.M., Glazov, E.A., Zhang, P., Rizvanov, A.A., Chestkov, I.V., and Kiselev, S.L. (2010). Induction of pluripotency in human endothelial cells resets epigenetic profile on genome scale. *Cell Cycle* 9**,** 937-946.

Lakoma, J., Rimondini, R., Donadio, V., Liguori, R., and Caprini, M. (2014). Pain related channels are differentially expressed in neuronal and non-neuronal cells of glabrous skin of fabry knockout male mice. *PLoS One* 9**,** e108641.

Lakoma, J., Rimondini, R., Ferrer Montiel, A., Donadio, V., Liguori, R., and Caprini, M. (2016). Increased expression of Trpv1 in peripheral terminals mediates thermal nociception in Fabry disease mouse model. *Mol Pain* 12.

Lamb, T.M., Knecht, A.K., Smith, W.C., Stachel, S.E., Economides, A.N., Stahl, N., Yancopolous, G.D., and Harland, R.M. (1993). Neural induction by the secreted polypeptide noggin. *Science* 262**,** 713-718.

Laplaca, M.C., and Thibault, L.E. (1997). An in vitro traumatic injury model to examine the response of neurons to a hydrodynamically-induced deformation. *Ann Biomed Eng* 25**,** 665-677.

Lenders, M., Stypmann, J., Duning, T., Schmitz, B., Brand, S.M., and Brand, E. (2016). Serum-Mediated Inhibition of Enzyme Replacement Therapy in Fabry Disease. *J Am Soc Nephrol* 27**,** 256-264.
Li, H., Jiang, H., Zhang, B., and Feng, J. (2018). Modeling Parkinson's Disease Using Patient-specific Induced Pluripotent Stem Cells. *J Parkinsons Dis* 8**,** 479-493.
Li, Y., Ji, A., Weihe, E., and Schafer, M.K. (2004). Cell-specific expression and lipopolysaccharide-induced regulation of tumor necrosis factor alpha (TNFalpha) and TNF receptors in rat dorsal root ganglion. *J Neurosci* 24**,** 9623-9631.
Liang, L., Lutz, B.M., Bekker, A., and Tao, Y.X. (2015). Epigenetic regulation of chronic pain. *Epigenomics* 7**,** 235-245.
Liu, Y., and Qin, N. (2011). TRPM8 in health and disease: cold sensing and beyond. *Adv Exp Med Biol* 704**,** 185-208.
Lo, B., and Parham, L. (2009). Ethical issues in stem cell research. *Endocr Rev* 30**,** 204-213.
Macdermot, K.D., Holmes, A., and Miners, A.H. (2001). Anderson-Fabry disease: clinical manifestations and impact of disease in a cohort of 60 obligate carrier females. *J Med Genet* 38**,** 769-775.
Majoul, I., Schmidt, T., Pomasanova, M., Boutkevich, E., Kozlov, Y., and Soling, H.D. (2002). Differential expression of receptors for Shiga and Cholera toxin is regulated by the cell cycle. *J Cell Sci* 115**,** 817-826.
Mariani, J., Simonini, M.V., Palejev, D., Tomasini, L., Coppola, G., Szekely, A.M., Horvath, T.L., and Vaccarino, F.M. (2012). Modeling human cortical development in vitro using induced pluripotent stem cells. *Proceedings of the National Academy of Sciences* 109**,** 12770-12775.
Mauhin, W., Lidove, O., Masat, E., Mingozzi, F., Mariampillai, K., Ziza, J.M., and Benveniste, O. (2015). Innate and Adaptive Immune Response in Fabry Disease. *JIMD Rep* 22**,** 1-10.
Mcdermott, L.A., Weir, G.A., Themistocleous, A.C., Segerdahl, A.R., Blesneac, I., Baskozos, G., Clark, A.J., Millar, V., Peck, L.J., Ebner, D., Tracey, I., Serra, J., and Bennett, D.L. (2019). Defining the Functional Role of NaV1.7 in Human Nociception. *Neuron* 101**,** 905-919 e908.
Meents, J.E., Bressan, E., Sontag, S., Foerster, A., Hautvast, P., Rosseler, C., Hampl, M., Schuler, H., Goetzke, R., Le, T.K.C., Kleggetveit, I.P., Le Cann, K., Kerth, C., Rush, A.M., Rogers, M., Kohl, Z., Schmelz, M., Wagner, W., Jorum, E., Namer, B., Winner, B., Zenke, M., and Lampert, A. (2019). The role of Nav1.7 in human nociceptors: insights from human induced pluripotent stem cell-derived sensory neurons of erythromelalgia patients. *Pain* 160**,** 1327-1341.
Mekhoubad, S., Bock, C., De Boer, A.S., Kiskinis, E., Meissner, A., and Eggan, K. (2012). Erosion of dosage compensation impacts human iPSC disease modeling. *Cell Stem Cell* 10**,** 595-609.
Mis, M.A., Yang, Y., Tanaka, B.S., Gomis-Perez, C., Liu, S., Dib-Hajj, F., Adi, T., Garcia-Milian, R., Schulman, B.R., Dib-Hajj, S.D., and Waxman, S.G. (2018). Resilience to Pain: A Peripheral Component Identified using induced Pluripotent Stem Cells and Dynamic Clamp. *J Neurosci*.
Moore, S.J., and Murphy, G.G. (2016). "Chapter 14 - Age-Related Alterations in Neural Plasticity," in *Handbook of the Biology of Aging (Eighth Edition),* eds. M.R. Kaeberlein & G.M. Martin. (San Diego: Academic Press), 391-405.
Namer, B., Schmidt, D., Eberhardt, E., Maroni, M., Dorfmeister, E., Kleggetveit, I.P., Kaluza, L., Meents, J., Gerlach, A., Lin, Z., Winterpacht, A., Dragicevic, E.,

Kohl, Z., Schuttler, J., Kurth, I., Warncke, T., Jorum, E., Winner, B., and Lampert, A. (2018). Pain relief in a neuropathy patient by lacosamide: Proof of principle of clinical translation from patient-specific iPS cell-derived nociceptors. *EBioMedicine*.

Newbern, J., Zhong, J., Wickramasinghe, R.S., Li, X., Wu, Y., Samuels, I., Cherosky, N., Karlo, J.C., O'loughlin, B., Wikenheiser, J., Gargesha, M., Doughman, Y.Q., Charron, J., Ginty, D.D., Watanabe, M., Saitta, S.C., Snider, W.D., and Landreth, G.E. (2008). Mouse and human phenotypes indicate a critical conserved role for ERK2 signaling in neural crest development. *Proc Natl Acad Sci U S A* 105**,** 17115-17120.

Newbern, J.M. (2015). Molecular control of the neural crest and peripheral nervous system development. *Curr Top Dev Biol* 111**,** 201-231.

Noh, H., Shao, Z., Coyle, J.T., and Chung, S. (2017). Modeling schizophrenia pathogenesis using patient-derived induced pluripotent stem cells (iPSCs). *Biochim Biophys Acta Mol Basis Dis* 1863**,** 2382-2387.

O'donovan, M., Ho, S., and Yee, W. (1994). Calcium imaging of rhythmic network activity in the developing spinal cord of the chick embryo. *J Neurosci* 14**,** 6354-6369.

Ohshima, T., Murray, G.J., Swaim, W.D., Longenecker, G., Quirk, J.M., Cardarelli, C.O., Sugimoto, Y., Pastan, I., Gottesman, M.M., Brady, R.O., and Kulkarni, A.B. (1997). alpha-Galactosidase A deficient mice: a model of Fabry disease. *Proc Natl Acad Sci U S A* 94**,** 2540-2544.

Okita, K., Ichisaka, T., and Yamanaka, S. (2007). Generation of germline-competent induced pluripotent stem cells. *Nature* 448**,** 313-317.

Ovesny, M., Krizek, P., Borkovec, J., Svindrych, Z., and Hagen, G.M. (2014). ThunderSTORM: a comprehensive ImageJ plug-in for PALM and STORM data analysis and super-resolution imaging. *Bioinformatics* 30**,** 2389-2390.

Petschnik, A.E., Fell, B., Tiede, S., Habermann, J.K., Pries, R., Kruse, C., and Danner, S. (2011). A novel xenogeneic co-culture system to examine neuronal differentiation capability of various adult human stem cells. *PLoS One* 6**,** e24944.

Poleganov, M.A., Eminli, S., Beissert, T., Herz, S., Moon, J.I., Goldmann, J., Beyer, A., Heck, R., Burkhart, I., Barea Roldan, D., Tureci, O., Yi, K., Hamilton, B., and Sahin, U. (2015). Efficient Reprogramming of Human Fibroblasts and Blood-Derived Endothelial Progenitor Cells Using Nonmodified RNA for Reprogramming and Immune Evasion. *Hum Gene Ther* 26**,** 751-766.

Politei, J.M., Bouhassira, D., Germain, D.P., Goizet, C., Guerrero-Sola, A., Hilz, M.J., Hutton, E.J., Karaa, A., Liguori, R., Üçeyler, N., Zeltzer, L.K., and Burlina, A. (2016). Pain in Fabry Disease: Practical Recommendations for Diagnosis and Treatment. *CNS Neurosci Ther* 22**,** 568-576.

Prada, J., Sasi, M., Martin, C., Jablonka, S., Dandekar, T., and Blum, R. (2018). An open source tool for automatic spatiotemporal assessment of calcium transients and local 'signal-close-to-noise' activity in calcium imaging data. *PLoS Comput Biol* 14**,** e1006054.

Ramaswami, U., Wendt, S., Pintos-Morell, G., Parini, R., Whybra, C., Leon Leal, J.A., Santus, F., and Beck, M. (2007). Enzyme replacement therapy with agalsidase alfa in children with Fabry disease. *Acta Paediatr* 96**,** 122-127.

Ratte, S., and Prescott, S.A. (2016). Afferent hyperexcitability in neuropathic pain and the inconvenient truth about its degeneracy. *Curr Opin Neurobiol* 36**,** 31-37.

Ries, M., Clarke, J.T., Whybra, C., Timmons, M., Robinson, C., Schlaggar, B.L., Pastores, G., Lien, Y.H., Kampmann, C., Brady, R.O., Beck, M., and Schiffmann, R. (2006). Enzyme-replacement therapy with agalsidase alfa in children with Fabry disease. *Pediatrics* 118**,** 924-932.
Rodgers, C.W. (2011). "Human Genetics: The Basics". Elsevier).
Rolfs, A. (2013). Interdisziplinäre Leitlinie für die Fiagnose und Therapie des Morbus Fabry. *Deutsche Gesellschaft für Neurologie*.
Sakaki-Yumoto, M., Katsuno, Y., and Derynck, R. (2013). TGF-beta family signaling in stem cells. *Biochim Biophys Acta* 1830**,** 2280-2296.
Sakiri, R., Ramegowda, B., and Tesh, V.L. (1998). Shiga toxin type 1 activates tumor necrosis factor-α gene transcription and nuclear translocation of the transcriptional activators nuclear factor-κB and activator protein-1. *Blood* 92**,** 558-566.
Scelfo, B., Politi, M., Reniero, F., Palosaari, T., Whelan, M., and Zaldívar, J.-M. (2012). Application of multielectrode array (MEA) chips for the evaluation of mixtures neurotoxicity. *Toxicology* 299**,** 172-183.
Schiffmann, R. (2009). Fabry disease. *Pharmacol Ther* 122**,** 65-77.
Schiffmann, R., Hughes, D.A., Linthorst, G.E., Ortiz, A., Svarstad, E., Warnock, D.G., West, M.L., Wanner, C., and Conference, P. (2017). Screening, diagnosis, and management of patients with Fabry disease: conclusions from a "Kidney Disease: Improving Global Outcomes" (KDIGO) Controversies Conference. *Kidney Int* 91**,** 284-293.
Schiffmann, R., Kopp, J.B., Austin, H.A., 3rd, Sabnis, S., Moore, D.F., Weibel, T., Balow, J.E., and Brady, R.O. (2001). Enzyme replacement therapy in Fabry disease: a randomized controlled trial. *JAMA* 285**,** 2743-2749.
Scott, L.J., Griffin, J.W., Luciano, C., Barton, N.W., Banerjee, T., Crawford, T., Mcarthur, J.C., Tournay, A., and Schiffmann, R. (1999). Quantitative analysis of epidermal innervation in Fabry disease. *Neurology* 52**,** 1249-1254.
Segebarth, D., Griebel, M., Dürr, A., Von Collenberg, C.R., Martin, C., Fiedler, D., Comeras, L.B., Sah, A., Stein, N., Gupta, R., Sasi, M., Lange, M.D., Tasan, R.O., Singewald, N., Pape, H.-C., Sendtner, M., Flath, C.M., and Blum, R. (2018). DeepFLaSH, a deep learning pipeline for segmentation of fluorescent labels in microscopy images. 473199.
Shu, L., Murphy, H.S., Cooling, L., and Shayman, J.A. (2005). An in vitro model of Fabry disease. *J Am Soc Nephrol* 16**,** 2636-2645.
Sims, R.J., 3rd, Nishioka, K., and Reinberg, D. (2003). Histone lysine methylation: a signature for chromatin function. *Trends Genet* 19**,** 629-639.
Spada, M., Pagliardini, S., Yasuda, M., Tukel, T., Thiagarajan, G., Sakuraba, H., Ponzone, A., and Desnick, R.J. (2006). High incidence of later-onset fabry disease revealed by newborn screening. *Am J Hum Genet* 79**,** 31-40.
Spradling, A.C., Nystul, T., Lighthouse, D., Morris, L., Fox, D., Cox, R., Tootle, T., Frederick, R., and Skora, A. (2008). Stem cells and their niches: integrated units that maintain Drosophila tissues. *Cold Spring Harb Symp Quant Biol* 73**,** 49-57.
Stacey, P., Wassermann, A.M., Kammonen, L., Impey, E., Wilbrey, A., and Cawkill, D. (2018). Plate-Based Phenotypic Screening for Pain Using Human iPSC-Derived Sensory Neurons. *SLAS Discov* 23**,** 585-596.
Stadtfeld, M., and Hochedlinger, K. (2010). Induced pluripotency: history, mechanisms, and applications. *Genes Dev* 24**,** 2239-2263.

Stadtfeld, M., Maherali, N., Breault, D.T., and Hochedlinger, K. (2008). Defining molecular cornerstones during fibroblast to iPS cell reprogramming in mouse. *Cell Stem Cell* 2**,** 230-240.
Stevens, B. (2003). Glia: much more than the neuron's side-kick. *Current Biology* 13**,** R469-R472.
Takahashi, K., Tanabe, K., Ohnuki, M., Narita, M., Ichisaka, T., Tomoda, K., and Yamanaka, S. (2007). Induction of Pluripotent Stem Cells from Adult Human Fibroblasts by Defined Factors. *Cell* 131**,** 861-872.
Takahashi, K., and Yamanaka, S. (2006). Induction of Pluripotent Stem Cells from Mouse Embryonic and Adult Fibroblast Cultures by Defined Factors. *Cell* 126**,** 663-676.
Takiguchi, M., Achanzar, W.E., Qu, W., Li, G., and Waalkes, M.P. (2003). Effects of cadmium on DNA-(Cytosine-5) methyltransferase activity and DNA methylation status during cadmium-induced cellular transformation. *Exp Cell Res* 286**,** 355-365.
Tchieu, J., Kuoy, E., Chin, M.H., Trinh, H., Patterson, M., Sherman, S.P., Aimiuwu, O., Lindgren, A., Hakimian, S., Zack, J.A., Clark, A.T., Pyle, A.D., Lowry, W.E., and Plath, K. (2010). Female human iPSCs retain an inactive X chromosome. *Cell Stem Cell* 7**,** 329-342.
Tcw, J. (2019). Human iPSC application in Alzheimer's disease and Tau-related neurodegenerative diseases. *Neurosci Lett* 699**,** 31-40.
Tsukimura, T., Nakano, S., Togawa, T., Tanaka, T., Saito, S., Ohno, K., Shibasaki, F., and Sakuraba, H. (2014). Plasma mutant alpha-galactosidase A protein and globotriaosylsphingosine level in Fabry disease. *Mol Genet Metab Rep* 1**,** 288-298.
Üçeyler, N., Biko, L., Hose, D., Hofmann, L., and Sommer, C. (2016). Comprehensive and differential long-term characterization of the alpha-galactosidase A deficient mouse model of Fabry disease focusing on the sensory system and pain development. *Mol Pain* 12.
Üçeyler, N., Ganendiran, S., Kramer, D., and Sommer, C. (2014). Characterization of pain in fabry disease. *Clin J Pain* 30**,** 915-920.
Üçeyler, N., Kafke, W., Riediger, N., He, L., Necula, G., Toyka, K.V., and Sommer, C. (2010). Elevated proinflammatory cytokine expression in affected skin in small fiber neuropathy. *Neurology* 74**,** 1806-1813.
Üçeyler, N., Kahn, A.K., Kramer, D., Zeller, D., Casanova-Molla, J., Wanner, C., Weidemann, F., Katsarava, Z., and Sommer, C. (2013). Impaired small fiber conduction in patients with Fabry disease: a neurophysiological case-control study. *BMC Neurol* 13**,** 47.
Üçeyler, N., Urlaub, D., Mayer, C., Uehlein, S., Held, M., and Sommer, C. (2019). Tumor necrosis factor-α links heat and inflammation with Fabry pain. *Molecular Genetics and Metabolism*.
Vedder, A.C., Linthorst, G.E., Houge, G., Groener, J.E., Ormel, E.E., Bouma, B.J., Aerts, J.M., Hirth, A., and Hollak, C.E. (2007). Treatment of Fabry disease: outcome of a comparative trial with agalsidase alfa or beta at a dose of 0.2 mg/kg. *PLoS One* 2**,** e598.
Velisetty, P., Stein, R.A., Sierra-Valdez, F.J., Vásquez, V., and Cordero-Morales, J.F. (2017). Expression and Purification of the Pain Receptor TRPV1 for Spectroscopic Analysis. *Scientific Reports* 7**,** 9861.
Voets, T., Droogmans, G., Wissenbach, U., Janssens, A., Flockerzi, V., and Nilius, B. (2004). The principle of temperature-dependent gating in cold- and heat-sensitive TRP channels. *Nature* 430**,** 748-754.

Waldek, S., Patel, M.R., Banikazemi, M., Lemay, R., and Lee, P. (2009). Life expectancy and cause of death in males and females with Fabry disease: findings from the Fabry Registry. *Genet Med* 11**,** 790-796.

Wang, X., Park, J., Susztak, K., Zhang, N.R., and Li, M. (2019). Bulk tissue cell type deconvolution with multi-subject single-cell expression reference. *Nature Communications* 10**,** 380.

Warren, L., Manos, P.D., Ahfeldt, T., Loh, Y.H., Li, H., Lau, F., Ebina, W., Mandal, P.K., Smith, Z.D., Meissner, A., Daley, G.Q., Brack, A.S., Collins, J.J., Cowan, C., Schlaeger, T.M., and Rossi, D.J. (2010). Highly efficient reprogramming to pluripotency and directed differentiation of human cells with synthetic modified mRNA. *Cell Stem Cell* 7**,** 618-630.

Watt, T., Burlina, A.P., Cazzorla, C., Schönfeld, D., Banikazemi, M., Hopkin, R.J., Martins, A.M., Sims, K., Beitner-Johnson, D., O'brien, F., and Feldt-Rasmussen, U. (2010). Agalsidase beta treatment is associated with improved quality of life in patients with Fabry disease: Findings from the Fabry Registry. *Genetics In Medicine* 12**,** 703.

Wilcox, W.R., Banikazemi, M., Guffon, N., Waldek, S., Lee, P., Linthorst, G.E., Desnick, R.J., Germain, D.P., and International Fabry Disease Study, G. (2004). Long-term safety and efficacy of enzyme replacement therapy for Fabry disease. *Am J Hum Genet* 75**,** 65-74.

Wilcox, W.R., Oliveira, J.P., Hopkin, R.J., Ortiz, A., Banikazemi, M., Feldt-Rasmussen, U., Sims, K., Waldek, S., Pastores, G.M., Lee, P., Eng, C.M., Marodi, L., Stanford, K.E., Breunig, F., Wanner, C., Warnock, D.G., Lemay, R.M., Germain, D.P., and Fabry, R. (2008). Females with Fabry disease frequently have major organ involvement: lessons from the Fabry Registry. *Mol Genet Metab* 93**,** 112-128.

Xie, W., Strong, J.A., Meij, J.T., Zhang, J.M., and Yu, L. (2005). Neuropathic pain: early spontaneous afferent activity is the trigger. *Pain* 116**,** 243-256.

Yang, Z., Tan, Q., Cheng, D., Zhang, L., Zhang, J., Gu, E.W., Fang, W., Lu, X., and Liu, X. (2018). The Changes of Intrinsic Excitability of Pyramidal Neurons in Anterior Cingulate Cortex in Neuropathic Pain. *Front Cell Neurosci* 12**,** 436.

Yauk, C., Polyzos, A., Rowan-Carroll, A., Somers, C.M., Godschalk, R.W., Van Schooten, F.J., Berndt, M.L., Pogribny, I.P., Koturbash, I., Williams, A., Douglas, G.R., and Kovalchuk, O. (2008). Germ-line mutations, DNA damage, and global hypermethylation in mice exposed to particulate air pollution in an urban/industrial location. *Proc Natl Acad Sci U S A* 105**,** 605-610.

Young, J.E., Martinez, R.A., and La Spada, A.R. (2009). Nutrient deprivation induces neuronal autophagy and implicates reduced insulin signaling in neuroprotective autophagy activation. *J Biol Chem* 284**,** 2363-2373.

Yu, M., and Haslam, D.B. (2005). Shiga toxin is transported from the endoplasmic reticulum following interaction with the luminal chaperone HEDJ/ERdj3. *Infect Immun* 73**,** 2524-2532.

Zhang, Y., and Kutateladze, T.G. (2018). Diet and the epigenome. *Nature Communications* 9**,** 3375.

Zumbrun, S.D., Hanson, L., Sinclair, J.F., Freedy, J., Melton-Celsa, A.R., Rodriguez-Canales, J., Hanson, J.C., and O'brien, A.D. (2010). Human intestinal tissue and cultured colonic cells contain globotriaosylceramide synthase mRNA and the alternate Shiga toxin receptor globotetraosylceramide. *Infect Immun* 78**,** 4488-4499.

8 Appendices

8.1 Media for cultivation

Table 4: Media for differentiation and maturation

Medium / Supplement	Final concentration
KSR medium	
KnockOut™ DMEM/F-12	Base medium
KnockOut™ Serum Replacement	15 %
GlutaMAX™	2 mM
2-Mercaptoethanol	100 µM
MEM NEAA solution	1X
Pen/Strep solution	1X
N-2 medium	
DMEM/F12 + GlutaMAX™	Base medium
B27-Plus Supplement	1X
N-2 Supplement	1X
Pen/Strep solution	1X
2i cocktail	
LDN-193189	100 nM
SB-431542	10 µM
5i cocktail	
LDN-193189	100 nM
SB-431542	10 µM
SU-5402	10 µM
DAPT	10 µM
CHIR 99021	3 µM
Maturation medium	
N-2 medium	Base medium
BDNF	20 ng/ml
GDNF	20 ng/ml
βNGF	20 ng/ml
Ascorbic acid	200 ng/ml

For abbreviations see **page 94**.

8.2 Reagents

Aqua-Poly/Mount	Polysciences, Warrington, PA
BSA	Sigma-Aldrich, St. Louis, MS, USA
ProLong™ Glass Antifade Mountant	Thermo Fisher Scientific, Waltham, MA; USA
DAPI	Sigma-Aldrich, St. Louis, MS, USA
Scandicain® 2%	AstraZeneca, London, UK
Cell culture base media	
DMEM/F-12	Thermo Fisher Scientific, Waltham, MA; USA
DMEM/F-12 + GlutaMAX™	Thermo Fisher Scientific, Waltham, MA; USA
KnockOut™ DMEM/F-12	Thermo Fisher Scientific, Waltham, MA; USA
StemMACS™ iPS-Brew XF, human	Miltenyi Biotec, Bergisch Gladbach, Germany
NutriStem® hPSC XF	Biological Industries, Kibbutz Beit-Haemek, Israel
Cell culture supplements / growth factors	
2-Mercaptoethanol	Thermo Fisher Scientific
N-2 Supplement	Thermo Fisher Scientific, Waltham, MA; USA
B-27™ Plus Supplement	Thermo Fisher Scientific, Waltham, MA; USA
DMSO Hybri-Max™	Sigma-Aldrich, St. Louis, MS, USA
FCS	Merck, Darmstadt, Germany
KnockOut™ Serum Replacement	Thermo Fisher Scientific, Waltham, MA; USA
Penicillin/Streptomycin	Thermo Fisher Scientific, Waltham, MA; USA
StemMACS™ iPS-Brew XF, human, 50X Supplement	Miltenyi Biotec, Bergisch Gladbach, Germany
BDNF	Peprotech, Rocky Hill, NJ, USA
GDNF	Peprotech, Rocky Hill, NJ, USA
βNGF	Peprotech, Rocky Hill, NJ, USA
Ascorbic acid	Sigma-Aldrich, St. Louis, MS, USA
MEM NEAA	
Cell culture small molecules	
StemMACS™ Y27632	Miltenyi Biotec, Bergisch Gladbach, Germany
CHIR99021	Axon Medchem, Groningen, Netherlands
StemMACS™ SB431542	Miltenyi Biotec, Bergisch Gladbach, Germany

LDN193189	STEMCELL Technologies, Vancouver, Canada
SU-5402	Sigma-Aldrich, St. Louis, MS, USA
DAPT	Sigma-Aldrich, St. Louis, MS, USA
Floxuridine	Santa Cruz Biotechnology, Dallas, TX, USA
Chemicals, Buffers	
0.5M EDTA	Thermo Fisher Scientific, Waltham, MA; USA
$DPBS^{-/-}$	Biochrom, Berlin, Germany
$DPBS^{+/+}$	Sigma-Aldrich, St. Louis, MS, USA
PFA	Electron Microscopy Sciences, Hatfield, PA; USA
Extracellular matrices	
Matrigel, GFR	Corning, Corning, NY, USA
Matrigel, hESC qualified	Corning, Corning, NY, USA
Nucleic acid extraction kits	
DNeasy Blood & Tissue Kit	Qiage, Hilden, Germany
miRNeasy Micro/Mini Kit	Qiage, Hilden, Germany
(qRT)-PCR reagents	
Primers (see **section8.6**)	Sigma-Aldrich, St. Louis, MS, USA
One*Taq*® Hot Start DNA Polymerase w. Master Mix	New England BioLabs, Ipswich, MA, USA
TaqMan™ Universal PCR Master Mix	Thermo Fisher Scientific, Waltham, MA; USA
TaqMan™ Probes (see **section 8.5**)	Thermo Fisher Scientific, Waltham, MA; USA
StemPro® Accutase®	Thermo Fisher Scientific, Waltham, MA; USA
StemRNA™ 3rd Gen. Reprogramming Kit	ReproCELL, Yokohama, Japan
Saponin	Sigma-Aldrich, St. Louis, MS, USA
Toxin-labelling / Click chemistry	
StxB	Sigma-Aldrich, St. Louis, MS, USA
DkTx	MyBioSource.com, San Diego, CA, USA

THE™ His Tag Antibody-iFluor 647	GenScript, Nanjing, China
SeTau-647-NHS	SETA BioMedicals, Urbana, IL, USA
BODIPY® FL	Thermo Fisher Scientific, Waltham, MA, USA
TrypLE™ Express	Thermo Fisher Scientific, Waltham, MA; USA

8.3 Buffers and solutions

Table 5: Buffers and solutions

Reagent	Final concentration
Lysis buffer	
NaOH	25 mM
EDTA	200 µM
Neutralizing buffer	
Tris-HCl	40 mM
Bath solution	
NaCl	180 mM
$CaCl_2$	1.8 mM
KCl	5.4 mM
$MgCl_2$	1 mM
HEPES	10 mM
Glucose	10 mM
Pipette solution	
KCl	170 mM
$MgCl_2$	2 mM
EGTA	1 mM
HEPES	5 mM
ATP	1 mM

For abbreviations see **page 94**

8.4 Technical equipment

6 mm skin punch biopsy	KAI, Solingen, Germany
Analog Vortex Mixer	VWR, Radnor, USA
accu-jet® pro pipette controller	BrandTech Scientific, Essex, CT, USA
Biosphere® Filter Tips	Sarstedt, Nuernbrecht, Germany
Cameras / Detectors	
Axiocam 506 mono	Carl Zeiss, Oberkochen, Germany
Edge 5.5	PCO, Kelheim, Germany
DFC3000G	Leica Microsystems, Wetzlar, Germany
DMC2900	Leica Microsystems, Wetzlar, Germany
SPOT INSIGHT™	Diagnostic Instruments, Sterling Heights, MI, USA
Cell culture consumables	
6-Well plate	Greiner Bio One, Frickenhausen, Germany
12-Well plate	Thermo Fisher Scientific, Waltham, MA, USA
24-Well plate	Thermo Fisher Scientific, Waltham, MA, USA
48-Well plate	Thermo Fisher Scientific, Waltham, MA, USA
Centrifuge tubes (15 ml, 50 ml)	Greiner Bio One, Frickenhausen, Germany
Cryovials	Greiner Bio One, Frickenhausen, Germany
Filtropur S 0.2 syringe filter	Sarstedt, Nürnbrecht, Germany
Pipette (5 ml, 10 ml, 25 ml, 50 ml)	Greiner Bio One, Frickenhausen, Germany
T-25 TC flask	Thermo Fisher Scientific, Waltham, MA, USA
Centrifuges	
Centrifuge 5417R	Eppendorf, Hamburg, Germany
Rotina 420R	Hettich, Tuttlingen, Germany
Combitips advanced® 0,5 ml	Eppendorf, Hamburg, Germany
Cryostat CM3050	Leica, Wetzlar, Germany
Flow cytometer	
FACSCanto™ II	BD Bioscience, East Rutherford, NJ, USA
LSR II	BD Bioscience, East Rutherford, NJ, USA
Freezer comfort -20°C	Liebherr, Biberach, Germany
Freezer TSX Series -80°C	Thermo Fisher Scientific, Waltham, MA, USA
Glass ware	
Coverglass, high precision,	Hartenstein, Würzburg, Germany

Coverglass, high precision 24x50 mm	Roth, Karlsruhe, Germany
Excitation light sources for microscopy	
Colibri 7 LED	Zeiss, Oberkochen, Germany
EL6000	Leica Microsystems, Wetzlar, Germany
HXP 120 C	Zeiss Oberkochen, Germany
Heracell™ VIOS 160i CO_2 incubator	Thermo Fisher Scientific, Waltham, MA, USA
Herasafe™ HS18 laminar flow hood	Heraeus, Hanau, Germany
MicroAmp® fast 96-well reaction plate	Applied Biosystems, Darmstadt, Germany
MicroAmp® adhesive film	Applied Biosystems, Darmstadt, Germany
Microscopes	
Apotome 2	Zeiss, Oberkochen, Germany
Axio Imager M.2	Zeiss, Oberkochen, Germany
Axiophot 2	Zeiss, Oberkochen, Germany
CKX41	Olympus, Tokyo, Japan
Elyra S.1 SIM	Zeiss, Oberkochen, Germany
DMi8	Leica Microsystems, Wetzlar, Germany
DMI IL LED	Leica Microsystems, Wetzlar, Germany
LSM700	Zeiss, Oberkochen, Germany
Multipette® Stream	Eppendorf, Hamburg, Germany
NanoDrop™ One Spectrophotometer	Thermo Fisher Scientific, Waltham, MA, USA
Objectslides superfrost	Langenbrinck, Teningen, Germany
PapPen	Sigma-Aldrich, St. Louis, MS, USA
Parafilm® M	Bemis Company Inc, Oshkosh, USA
PCR Tubes 0,2 ml, 1,5 ml	Eppendorf, Hamburg, Germany
Pipettes	
Research® plus	Eppendorf, Hamburg, Germany
Software	
DNA Baser	Heracle BioSoft, Pitesti, Romania
FACSDiva	BD Bioscience, East Rutherford, NJ, USA
FlowJo v10	FlowJo, Ashland, OR, USA
GraphPad Prism 8	GraphPad Software, San Diego, CA, USA
Image J free v1.52i	National Institute of Health, Bethesda, MD, USA

LAS X	Leica Microsystems, Wetzlar, Germany
Office 2016	Microsoft, Redmond, WA, USA
SPSS IBM version 26	IBM, Ehningen, Germany
ZEN Blue/Black Edition	Zeiss, Oberkochen, Germany
Thermocycler	
Peqstar	Peqlab, Erlangen, Germany
Primus 96	Peqlab, Erlangen, Germany
QuantStudio 3	Applied Biosystems, Darmstadt, Germany
Tissue-Tek® Cryomold	Sakura, Staufen, Germany

For abbreviations see **page 94**

8.5 qRT-PCR probes

Table 6: TaqMan probes.

Gene/Target	Assay-ID
18S rRNA	Hs99999901_s1
PRPH	Hs00196608_m1
SCN9A	Hs01076699_m1
TRPV1	Hs00218912_m1
TUBB3	Hs00801390_s1

8.6 PCR cycling conditions and primers

Table 7: PCR experiment variables.

Target	Sequence (5'-3')	Annealing temp.
GLA c.708G>C (TK1)	Fw: CTGTAAACTCAAGAGAAGG Rev: CATCCTGCTCTAAGTAC	44°C
GLA cDNA Exon 5 (TK1)	Fw: ATTGATGCCCAGACCTTTGC Rev: GGGTCCTGATTGATGGCAATTAC	54°C
GLA c.1069C>T (TK8)	Fw: ACAGGGCCACTTATCAC Rev: AAAGGTGGACAGGAAGTAG	53°C
GLA c.568delG (TK9)	Fw: CACAATTTAAGCACAGAGCAAC Rev: GGACATGAATGGTGAAATAAAGGG	51°C
Mycoplasma sp.	Fw: GGGAGCAAACAGCATTAGATACCCT Rev: TGCACCATCTGTCACTCTGTTAACCTC	55°C

Abbreviations: GLA = α-galactosidase A

8.7 Antibodies for ICC/IHC/FACS

Table 8: Primary antibodies

Reactivity	Host	Company	Catalog #	Dilution
BRN3A	Goat	Santa Cruz Biotechnology	sc-31984	1:50
FOXA2	Mouse	Santa Cruz Biotechnology	sc-374376	1:50
LAMP1	Mouse	DSHB	H4A3	1:100
$Na_v1.8$	Rabbit	Alomone Labs	ASC-016	1:200
NCAM::647	Mouse	BioLegend	362513	1:100
OCT3/4	Mouse	Santa Cruz Biotechnology	sc-5279	1:50
PAX6	Rabbit	BioLegend	901302	1:200
PRPH::488	Mouse	Santa Cruz Biotechnology	sc-377093 AF488	1:250
PRPH::647	Mouse	Santa Cruz Biotechnology	sc-377093 AF647	1:250
REA Control (S)-APC	Human	Miltenyi-Biotec	130-113-434	1:11
REA Control (S)-PE	Human	Miltenyi-Biotec	130-113-438	1:11
SM22A	Rabbit	Abcam	ab14106	1:100
SOX10	Mouse	Santa Cruz Biotechnology	sc-365692	1:100
SOX2	Mouse	R&D Systems	MAB2018	1:200
SP::594	Rat	Santa Cruz Biotechnology	sc-21715 AF594	1:100
SSAE4-APC	Human	Miltenyi-Biotec	130-098-347	1:11
SSEA4	Mouse	R&D Systems	MAB1435	1:100
TRA-1-60	Mouse	Merck Millipore	MAB4360	1:100

TRA-1-60::488	Human	Miltenyi-Biotec	130-106-872	1:100
TRA-1-60-PE	Human	Miltenyi-Biotec	130-100-350	1:11
TRPV1	Goat	Santa Cruz Biotechnology	sc-12503	1:150
TUJ1	Chicken	Abcam	ab41489	1:500

For abbreviations see **page 94**

Table 9: Secondary antibodies

Reactivity	**Host**	**Company**	**Catalog # + dye**	**Dilution**
Chicken-IgY	Donkey	Jackson Immunoresearch	703-165-155 Cy3	1:100
Chicken-IgY	Donkey	Jackson Immunoresearch	703-545-155 AF488	1:300
Goat-IgG	Donkey	Jackson Immunoresearch	705-165-147 Cy3	1:100
Mouse-IgG	Donkey	Jackson Immunoresearch	715-165-150 Cy3	1:100
Mouse-IgG	Donkey	Jackson Immunoresearch	715-605-150 AF647	1:300
Mouse-IgG	Donkey	Jackson Immunoresearch	715-005-150 No dye	1:150
Rabbit-IgG	Donkey	Jackson Immunoresearch	711-605-152 AF647	1:300
Rabbit-IgG	Donkey	Jackson Immunoresearch	711-545-152 AF488	1:300

For abbreviations see **page 94**

8.8 Characterization for the second clone of TK8 and TK9

Two additional clones were generated and characterized for TK8 (**Figure 28**), and TK9 (Figure 29).

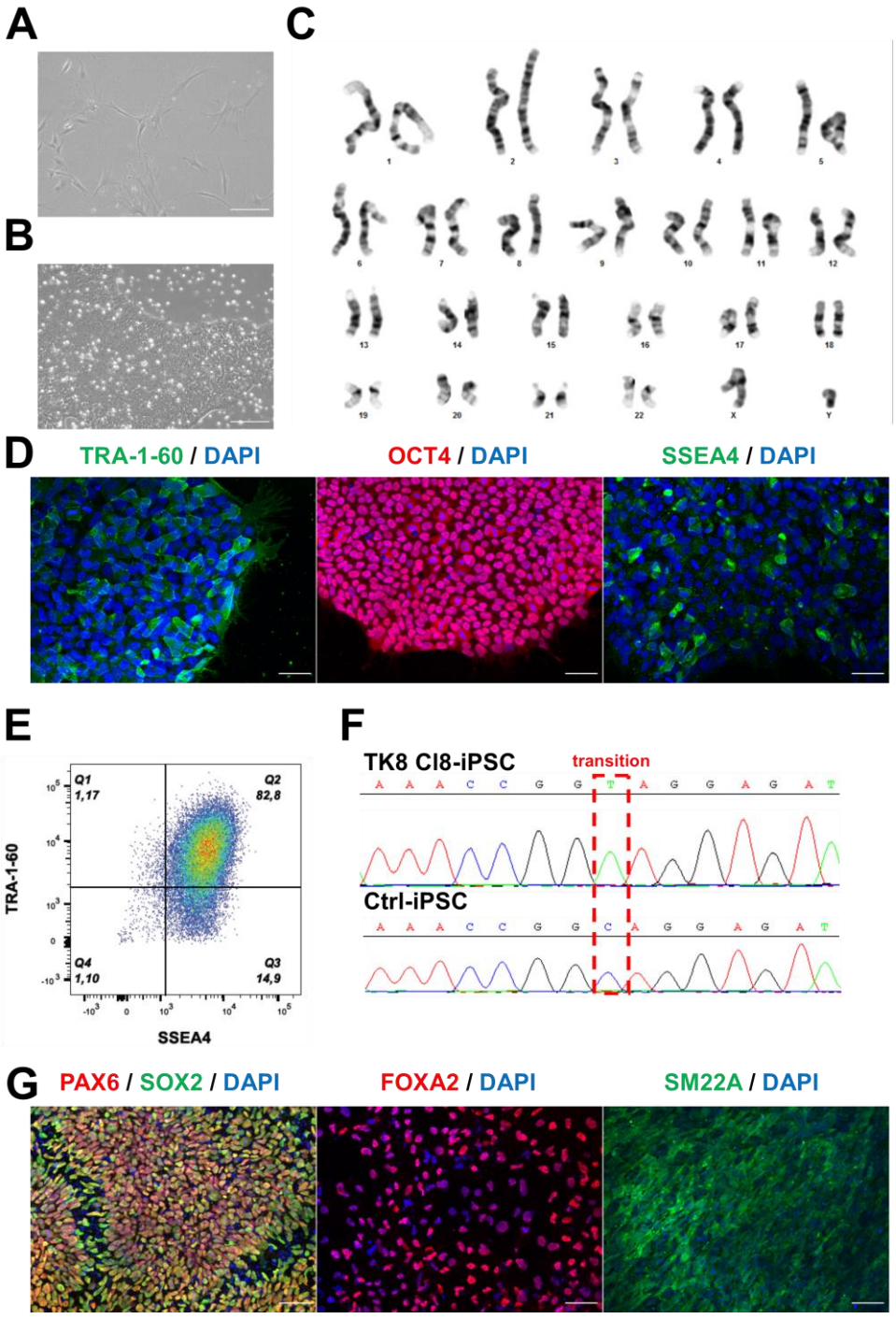

Figure 28: Characterization of TK8 clone 8. (A) HDF were reprogrammed to (B) iPSC with ESC-like morphology. (C) No chromosomal aberrations were found and (D) robust expression of the pluripotency markers was confirmed. (E) > 82% of live, single cells coexpressed TRA-1-60 and SSEA4, with (F) the retained c.1069C>T mutation. (G) Directed differentiation of cells into all three germ-layers was succesfull. Scale bars: 200 µm (A, B); 50 µm (D, G). Acquired with DMI IL LED (A, B) and Apotome (D, G).

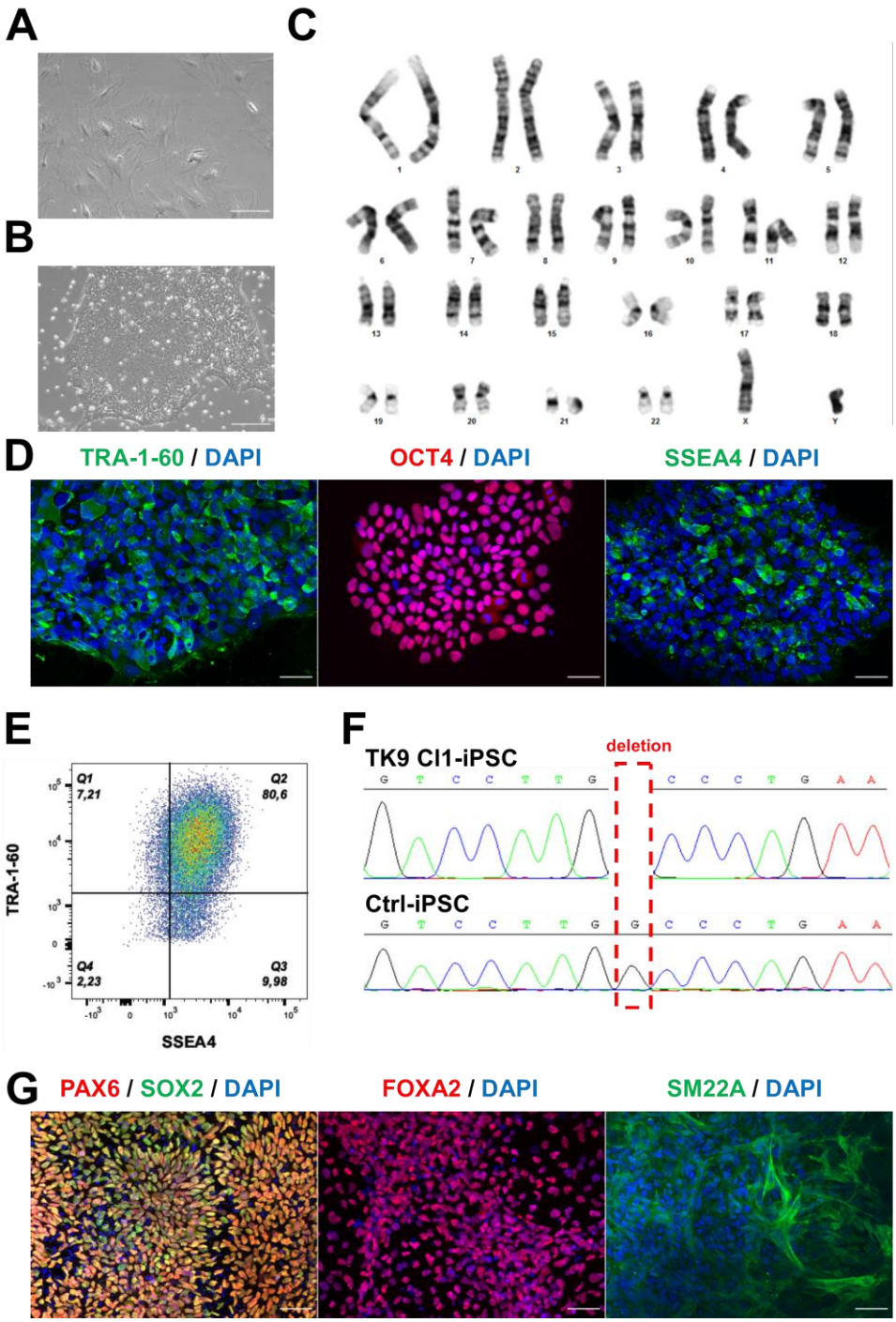

Figure 29: Characterization of TK9 clone 1. (A) HDF were reprogrammed to (B) iPSC with ESC-like morphology. (C) No chromosomal aberrations were found and (D) robust expression of the pluripotency markers was confirmed. (E) > 80% of live, single cells coexpressed TRA-1-60 and SSEA4, with (F) the retained c.68delG mutation. (G) Directed differentiation of cells into all three germ-layers was succesfull. Scale bars: 200 µm (A, B); 50 µm (D, G). Acquired with DMI IL LED (A, B) and Apotome (D, G).

Abbreviations for **Figure 28** and **Figure 29**: Ctrl = control; DAPI = 4′,6-diamidino-2-phenylindole; ESC = embryonic stem cell; FOXA2 = forkhead box protein A2; HDF = human dermal fibroblasts; iPSC = induced pluripotent stem cells; OCT4 = octamer-binding transcription factor 4; PAX6 = paired box 6, SM22A = smooth muscle protein 22-alpha; SOX2 = sex determining region Y box 2; SSEA4 = stage specific embryonic antigen 4; TRA-1-60 = tumor resistance antigen 1-60

8.9 Marker expression of mature neurons of additional clones

One additional clone of TK8 and TK9 (**Figure 30**) were analyzed for sensory marker expression.

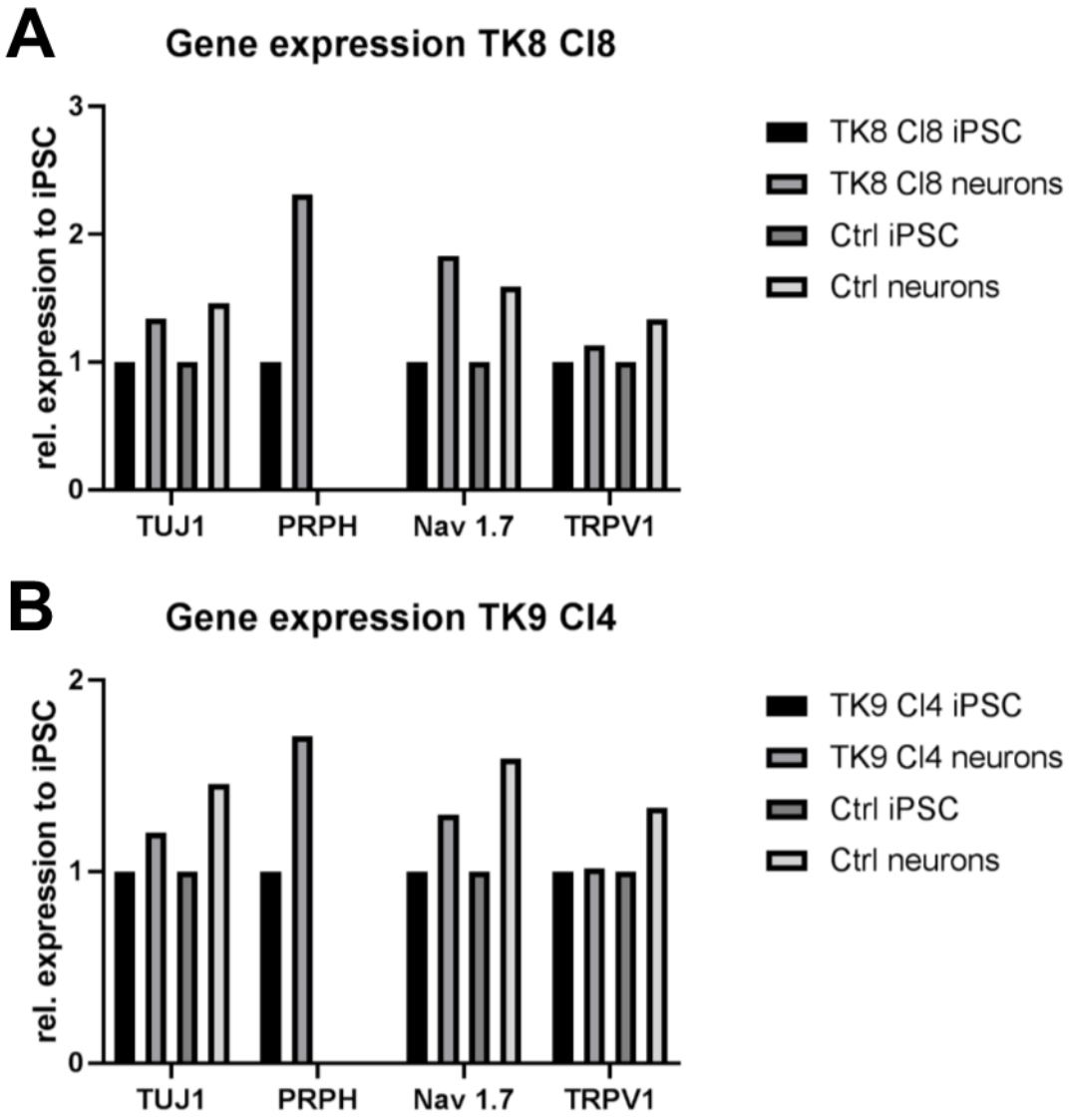

Figure 30: Gene expression on mature neurons. Neurons from (A) TK8 clone 8 and (B) TK9 clone 4 expressed TUJ1, PRPH, Nav 1.7 and TRPV1.

8.10 Myoplasma screening

TK1 (**Figure 31 A**), TK8, and TK9 (**Figure 31 B**) iPSC lines were analyzed for mycoplasma contamination. No signal at 300 bp shows the absence of mycoplasma contamination in conditioned medium of all cell lines.

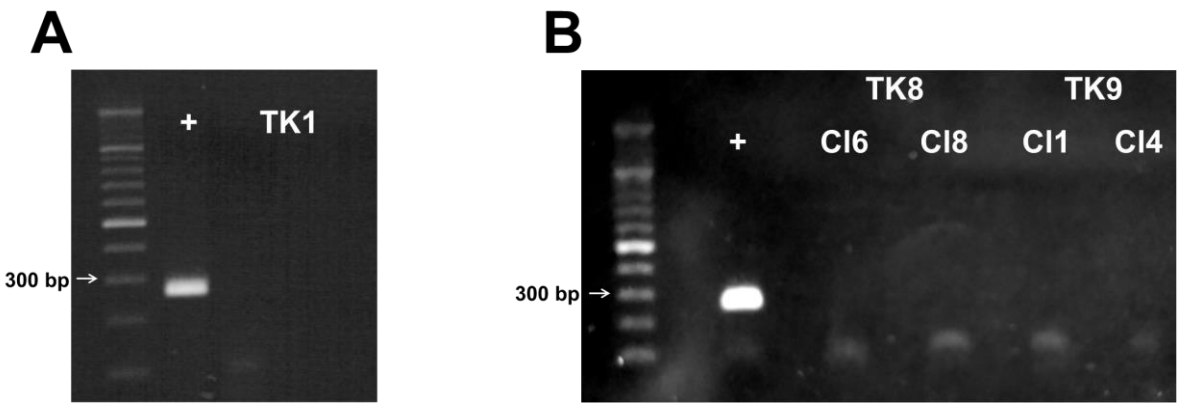

Figure 31: PCR for mycoplasma detection. (A) From left to right: 100 bp DNA ladder, positive control, medium from TK1-iPSC. (B) From left to right: 100 bp DNA ladder, positive control, medium from TK8 Cl.6, TK8 Cl.8, TK9 Cl.1, TK9 Cl.4

Abbreviations: + = positive control; bp = base pairs;

9 Abbreviations

2/5i	2/5 inhibitor cocktail
AF-xxx	Alexa Fluor™-xxx
AP	action potential
APC	allophycocyanin
βNGF	β-nerve growth factor
BDNF	brain-derived neurotrophic factor
BRN3A, POU4F1	POU class 4 homebox 1
CDC20	cell division cycle 20
CGRP	calcitonin gene-related peptide
CLSM	confocal laser scanning microscope
CM	cardiomyocytes
CNS	central nervous system
Ctrl	control
DAPI	4’,6-Diamidin-2-phenylindol
DMEM	Dulbecco’s modified Eagle medium
(c)(g)DNA	(copy)(genomic)deoxyribonucleic acid
DMSO	dimethyl sulfoxide
DNMT3B	DNA methyltransferase 3 β
$DPBS^{-/-}$	Dulbecco’s Phosphate-Buffered Saline
$DPBS^{+/+}$	Dulbecco’s Phosphate-Buffered Saline with Mg^{++}, Ca^{++}
DPPA2	developmental pluripotency associated 2
DRG	dorsal root ganglion

*d*STORM	direct stochastic optical reconstruction microscopy
ECM	extracellular matrix
EDTA	ethylenediaminetetraacetic acid
EGTA	egtazic acid
ERT	enzyme replacement therapy
ESRRB	estrogen related receptor β
EZH2	enhancer of zeste 2 polycomb repressive complex 2 subunit
FACS	fluorescence activated cell sorting
FBXO15	F-box Protein 15
FCS	fetal calf serum
FD	Fabry disease
FdU	floxuridine
FGF4	fibroblast growth factor 4
FOXA2	forkhead box protein A2
Gb3	globotriaosylceramide
Gb4	globotetrahexosylceramide
GDNF	glial cell-derived neurotrophic factor
GLA	alpha-galactosidase A
HDF	human dermal fibroblast
hESC, ES	human embryonic stem cell
ICC	immunocytochemistry
IENFD	intraepidermal nerve fiber density

IHC	immunohistochemistry
iPSC	induced pluripotent stem cells
Klf4	Kruppel-like factor 4
KO	KnockOut
KO-SR	KnockOut™ Serum Replacement
LIN28	Lin-28 homolog A
MEM NEAA	minimum essential medium non –essential amino acids
MET	Mesenchymal-epithelial transition
Na_v	voltage gated sodium channel
NCAM, CD56	neural cell adhesion molecule
NR6A1	nuclear receptor subfamily group A member 1
Oct4	octamer-binding transcription factor 4
PAX6	paired box protein 6
(qRT)(RT)-PCR	(quantitative real-time)(reverse transcription) polymerase chain reaction
PE	phycoerythrin
PFA	paraformaldehyde
PNS	peripheral nervous system
PRPH	peripherin
(m)(mi)RNA	(messenger)(micro)ribonucleic acid
ROCK(i)	Rho-associated protein kinase (inhibitor)
RT	room temperature
SALL4	spalt like transcription factor 4

SCNxA	sodium voltage-gated channel alpha subunit X
SIM	strucuted illumination microscopy
SIM	structured illumination microscopy
SM22A	smooth muscle protein 22-alpha
SOX10	sex determining region Y-box 10
SOX2	sex determining region Y-box 2
SSEA4	stage-specific embryonic antigen-4
StxB	Shiga toxin 1, B subunit
TRA-1-60	tumor resistance antigen 1-60
TRPV1	transient-receptor potential cation channel subfamily V member 1
TUJ1	neuron-specific class III β-tubulin
UTF1	undifferentiated embryonic cell transcription factor 1
wt	wildtype
XCI	X-chromosomal inactivation
YF	Yamanaka factors

10 List of Figures and Tables

11 Curriculum vitae

12 Publications

Peer reviewed journals; original articles

Klein, T., Klug, K., Henkel, L., Kwok, C.K., Edenhofer, F., Klopocki, E., Kurth, I., and Üçeyler, N. (2019). Generation of two induced pluripotent stem cell lines from skin fibroblasts of sisters carrying a c.1094C>A variation in the SCN10A gene potentially associated with small fiber neuropathy. *Stem Cell Res* 35**,** 101396.

Klein, T., Günther, K., Kwok, C.K., Edenhofer, F., and Üçeyler, N. (2018a). Generation of the human induced pluripotent stem cell line (UKWNLi001-A) from skin fibroblasts of a woman with Fabry disease carrying the X-chromosomal heterozygous c.708G>C (W236C) missense mutation in exon 5 of the alpha-galactosidase-A gene. *Stem Cell Res* 31**,** 222-226.

Klein, T., Henkel, L., Klug, K., Kwok, C.K., Klopocki, E., and Üçeyler, N. (2018b). Generation of the human induced pluripotent stem cell line UKWNLi002-A from dermal fibroblasts of a woman with a heterozygous c.608 C>T (p.Thr203Met) mutation in exon 3 of the nerve growth factor gene potentially associated with hereditary sensory and autonomic neuropathy type 5. *Stem Cell Res* 33**,** 171-174.

Leinders, M., Doppler, K., **Klein, T.**, Deckart, M., Rittner, H., Sommer, C., and Üçeyler, N. (2016). Increased cutaneous miR-let-7d expression correlates with small nerve fiber pathology in patients with fibromyalgia syndrome. *Pain* 157**,** 2493-2503.

Poster presentations at international conferences:

Klein, T., Günther, K., Schlegel, J., Wischmeyer, E., Edenhofer, F., Klopocki, E., Sauer, M., Üçeyler, N. (2018). Induced pluripotent stem cells generated from skin fibroblasts of a female patient with FD are susceptible to cell death during nociceptive differentiation – CAVE: X-inactivation. 48th international meeting of the Society for Neuroscience, San Diego, USA

Karl, F., Malzacher, T., Kreß, L., **Klein, T.**, Saffer, N., Fey, P., Sommer, C., Groeber-Becker, F., Üçeyler, N. (2018). Extended use of diagnostic skin punch biopsies of SFN patients to multiply limited material for new in vitro tools to investigate small fiber pathology. 48th international meeting of the Society for Neuroscience, San Diego, USA

Klein, T., Günther, K., Sommer, C., Wischmeyer, E., Edenhofer, F., Üçeyler, N. (2017) Generation of patient-derived sensory neurons using iPSCs & smNPCs obtained from patients with Fabry disease. 47th International meeting of the Society for Neuroscience, Washington D.C., USA

Klein, T., Günther, K., Sommer, C., Edenhofer, F., Üçeyler, N. (2017). Generation of patient-derived sensory neurons using iPSC and smNPC obtained from patients with Fabry disease. 9th international meeting Stem Cell Network North Rhine-Westphalia, Münster, Germany

Klein, T., Günther, K., Sommer, C., Edenhofer, F., Üçeyler, N. (2016). Patient-derived peripheral sensory neurons as possible disease model for Fabry pain. 11th international symposium EUREKA, Würzburg, Germany

13 Danksagung

Diese Arbeit wäre nicht möglich gewesen ohne die Unterstützung vieler Leute. Falls ich jemanden vergessen habe, war das keine Absicht und ich entschuldige mich prophylaktisch dafür!

Frau Prof. Dr. Nurcan Üçeyler: Vielen Dank für die Möglichkeit meine Doktorarbeit in diesem Bereich schreiben zu dürfen. Vielen Dank auch für das Vertrauen, das Du in mich setzt, ich habe sehr viel gelernt während dieser Zeit.

Mein weiterer Dank gilt auch den Mitgliedern meines Promotionskomitees, Herrn PD Dr. Robert Blum, Herr Prof. Dr. Erhard Wischmeyer und Frau Prof. Dr. Claudia Sommer für den (wissenschaftlichen) Austausch und Kritik im Rahmen der Reports, oder auch bei den Retreats.

Meinen Bürokollegen Dr. Franziska Karl, Dr. Lukas Hofmann, Christoph Erbacher möchte ich von Herzen für die angenehme Arbeitsatmosphäre danken, bei der der Spaß nie zu kurz gekommen ist und die mich stets bei wissenschaftlichen, aber auch bürokratischen Hürden gut beraten haben. Katharina Klug, danke für dein Engagment während deiner Masterarbeit und dem Teilen der Wochenenddienste! Für die Wochenenddienste auch vielen Dank an Max Breyer, Chiazor Maureen Bob-Anyeji, Anna Forster und v.a. Bettina Vignolo, die sich auch bereit erkärt hat tausende Neurone auszuzählen.

Danke auch an die vielen TAs aus der Klinik, die mich entweder direkt bei der wissenschftlichen Arbeit unterstützt haben, oder für ausreichend Kaffeenachschub gesorgt haben! Daniela Urlaub, die mich bei der Zellkultur entlastet hat: DANKE!

Ohne die enge Kooperation mit dem Institut für Biophysik und Biotechnologie wären viele Versuche in dieser Arbeit nicht möglich gewesen. Vielen Dank hierfür an Herrn Prof. Dr. Markus Sauer und v.a. auch Jan Schlegel. Jan, Danke für die Unterstützung sowohl bei den Versuchen, als auch als Kumpel beim Feierabendbier. Dass aus einer Idee, geboren beim Bier, eine offizielle Kooperation mit Nachfolgeprojekt wird, wer hätte an dem Abend damit gerechnet… Danke, ich schulde dir so einiges!

Mein Dank geht auch an Frau Dr. Katharina Günther, die mich in die Methodik der iPSC eingelernt hat und doch öfters Recht hatte, als ich es anfangs wahrhaben wollte.

Nicht zuletzt möchte ich mich bei allen weiteren Freunden bedanken, die mich moralisch unterstützt haben!

Und zu guter Letzt gilt mein besonderer Dank natürlich meiner Familie, ohne die ich niemals an diesem Punkt stehen würde. **DANKE für alles!**